Pump-Probe Experiments & Radiation Generation using Laser Wakefield Accelerators

by

William Alexander Schumaker

A dissertation submitted in partial fulfillment
of the requirements for the degree of
Doctor of Philosophy
(Nuclear Engineering and Radiological Sciences)
in The University of Michigan
2014

Doctoral Committee:

Professor Karl M. Krushelnick, Co-Chair
Assistant Professor Alexander G. R. Thomas, Co-Chair
Professor Roy Clarke
Research Scientist Anatoly M. Maksimchuk

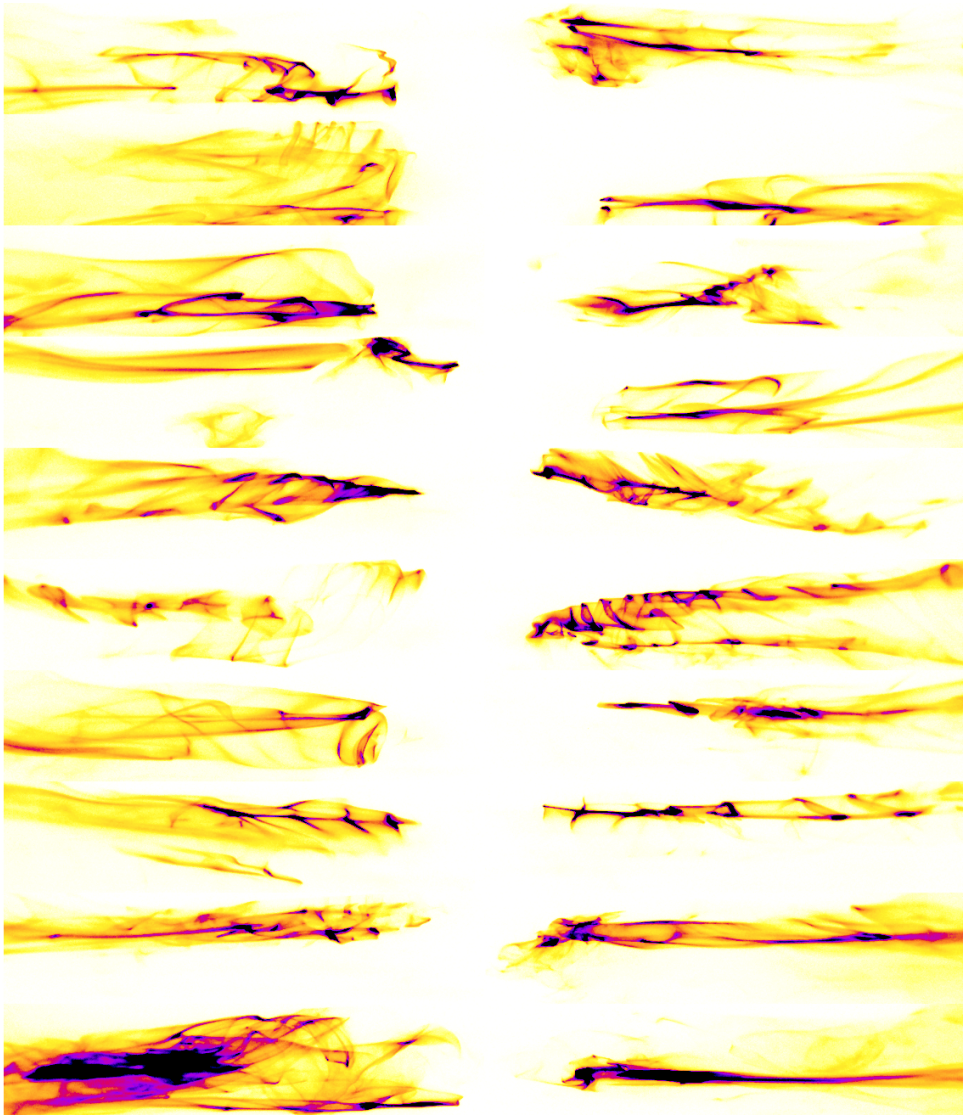

"I was like a boy playing on the sea-shore, and diverting myself now and then finding a smoother pebble or a prettier shell than ordinary, whilst the great ocean of truth lay all undiscovered before me."

-Sir Isaac Newton

For the advancement of science.

ACKNOWLEDGEMENTS

I would like to thank everyone who made this dissertation and my academic journey both possible and enjoyable.

First and foremost, I want to especially thank my advisors Karl and Alec. Thank you Karl for always sharing the big picture and believing in me, even going so far as trusting me with your cats. Thank you Alec for inspiring and encouraging my creativity, even with my many "brave proposals."

From our group, I must thank: Chris, for mentoring me and teaching me everything he could; Takeshi, for inspiration from his big ideas and his galactic "empire"; Tolya, for teaching me the "proper" techniques; Victor, Vladimir, and Bixue, for maintaining the HERCULES laser and making this thesis possible; Galina, for staying and supporting us on many late nights; John, for showing me how to be resourceful and clever; Louise, for always providing constructive criticism and feedback; Franklin, for being FRANKLIN^{TM}; Calvin, for being my private ski patrol; Mike V., for introducing me to surfing (the quintessential wakefield sport) and challenging me to become a better mentor; and Tony, for never being content with the status quo.

Of course, I must acknowledge those whom I have worked with from across the pond(s): Jean-Raphaël, for always being patient; Stefan, for his re-ridiculousness and awesome example; Nobu, for sharing takoyaki and Osaka; Mike B., for settling Catan; Gianluca, for being demanding of me (in the good way); Jason, for his impressive "tube stands"; Kris, for use of his posh London loft; Dan, for being bothered; and Darragh, for sharing Northern Ireland.

Also, I would like to thank the following for their support: NERS and CUOS staff, students, and scientists too numerous to list; RAL-CLF laser staff; Imperial College/Oxford plasma physics faculty and students; Lurie Nano-Fab staff; Physics machine shop staff; MPowered students; CFY instructors; many friends made along the way, especially: Manu, John Z., Ching-Han (Eric), Shreyas, Kyla, and Chas; the Greek gods of Mt. Olympus, especially Poseidon!; feline companions: Hubs (RIP), Sweetie, Punk & Bullsquid; and so many others whom I don't mention here.

Special thanks to Mike M. for his friendship and camaraderie through the best of times and the worst of times.

Last, but not least, I would like to thank my parents, Mark and Pam, and my grandmother, Doris. Without their continued support and interest for my educational success, I certainly would not have made it this far in my academic journey.

TABLE OF CONTENTS

LIST OF FIGURES

Figure

LIST OF TABLES

Table

LIST OF APPENDICES

Appendix

LIST OF ABBREVIATIONS

AR	Anti-Reflection
ASE	Amplified Spontaneous Emission
BGO	bismuth germanium oxide
BSI	Barrier Suppression Ionization
CCD	Charge Coupled Device
CPA	Chirped Pulse Amplification/Amplifed
CUOS	Center for Ultrafast Optical Science
DM	Deformable Mirror
DU	Depleted uranium
EOS	Equation of State
(X)FEL	(X-ray) Free Electron Laser
FROG	Frequency Resolved Optical Gating
FOP	Fiber-Optic Plate
FWHM	Full Width at Half Maximum
HDPE	High-Density polyethylene
HED	High-Energy Density
HERCULES	High-Energy Repetitive CUOS LasEr System
HHG	High-Harmonic Generation
HPGe	High-Purity germanium

HR	High Reflectivity
ICF	Inertial Confinement Fusion
ICS	Inverse Compton Scattering
IP	Image Plate
LCLS	Linac Coherent Light Source
LPA	Laser Plasma Accelerator
LWFA	Laser Wakefield Acceleration/Accelerator/Accelerated
MCA	Multi-Channel Analyzer
MCP	Micro-Channel Plate
MEC	Matter at Extreme Conditions
Nd:YAG	neodymium-doped yttrium aluminum garnet
Nd:YLF	neodymium-doped yttrium lithium fluoride
NLTS	Non-Linear Thomson Scattering
OAP	Off-Axis Paraboloid
OD	Optical Density
PIC	Particle-in-Cell
PMT	Photo-Multiplier Tube
PSL	Photo-Stimulated Luminescence
QE	Quantum Efficiency
(n)QED	(non-linear) Quantum Electrodynamics
QL	Quantum Level
RF	Radio Frequency
SCA	Single-Channel Analyzer
SHG	Second Harmonic Generation
SLAC	Stanford Linear Accelerator Center
SM-LWFA	Self-Modulated Laser Wakefield Acceleration
SNM	Special Nuclear Material

THG	Third Harmonic Generation
Ti:S	titanium-doped sapphire
TNSA	Target Normal Sheath Acceleration
TOF	Time-of-Flight
WDM	Warm Dense Matter
XPW	Cross-Polarized Wave
XUV	Extreme Ultraviolet

ABSTRACT

Pump-Probe Experiments & Radiation Generation using Laser Wakefield Accelerators

by

William Alexander Schumaker

Co-Chairs: Karl M. Krushelnick & Alexander G. R. Thomas

This thesis describes pump-probe experiments using Laser Wakefield Acceleration (LWFA) as the radiation source. LWFA systems generate highly relativistic electron beams in a compact geometry by driving a nonlinear plasma wave with an ultraintense laser pulse. These electrons beams, or the secondary radiation that they create, can be used to pump or probe interactions on fs-timescales due to inherent synchronization with the laser driver.

In this thesis, the first sub-ps measurements of magnetic field dynamics in ultra-intense laser-solid interactions are presented. This experiment employed the LWFA electron beam to probe the laser-irradiated target at different time delays, and by measuring the subsequent beam deflections, the evolution of the magnetic field could be inferred. The effect of laser temporal contrast on the laser-target interaction was observed to play a crucial role in the magnetic field dynamics. High-contrast laser conditions were observed to rapidly evolve over the course of ps-timescale as electrons propagated radially along both the front and rear of the target, establishing an azimuthal field that was stronger on the front surface. On the other hand, low-

contrast laser conditions allowed ablated plasma on the front surface of the target to limit magnetic field growth to only the rear of the target.

Using high-energy LWFA electron beams, bremsstrahlung radiation was created by interaction with various solid targets. Secondary processes generate high-energy electrons, positrons, neutrons, and pions, which can be measured using magnetic spectrometers, nuclear activation, bubble detectors, and Compton scattering. Presented in this thesis are proof-of-principle results from a high-resolution, high-energy gamma-ray spectrometer capable of single-shot operation as well as high repetition rate activation diagnostics. The first measurements of laser-generated neutral electron-positron plasma beams are also presented. The pump-probe interaction of these beams with other laser-produced plasmas will allow the study of astrophysical phenomena in a compact, laboratory setting.

One promising pump-probe application of LWFA is the compact implementation of nonlinear Thomson scattering (NLTS). Using high-energy LWFA electrons as a pump, a second, counter-propagating, ultraintense laser pulse can Thomson backscatter off these electrons and get upshifted to $\sim MeV$ energies, yielding a high-brightness source of high-energy photons. The experimental attempts of NLTS here at Michigan and in the United Kingdom are presented in this thesis and should help guide upcoming attempts at NLTS.

CHAPTER I

Introduction

1.1 Motivation

The development of particle accelerators in the last century has transformed our understanding of physics from the sub-atomic to astronomical scales. Early accelerators investigated nuclear structure, explored the stability of nuclei, and discovered synthetic isotopes (still an ongoing topic of research). Accelerators have since produced all 17 of the elementary particles predicted by the Standard Model and have shed light on the rules of particle interactions that shape the universe. High-energy accelerators today strive to achieve $> TeV$ center-of-mass collisional energies to search for exotic particles or physics lying beyond the heaviest particle, the recently discovered Higgs boson.

The first kind of particle accelerator - the electrostatic generator - was quickly transformed from an entertaining curiosity to an important scientiifc instrument. The accelerating potential of a single electrostatic accelerator stage is limited by the highest voltage which can be applied without breakdown (for example, a 10 MV Van de Graaff generator). A tandem accelerator can be used to double this maximum, and a stepped device such as a Cockcroft-Walton generator can be used to effciently synthesize high voltage. It was soon realized however that instead of accelerating entirely in single or modular stages, acceleration to very high energies could be made

Figure 1.1: Aerial photograph of the SLAC 3 km long linear accelerator. Note the I-280 expressway crossing over the facility for a sense of scale.

more practical by applying accelerating fields which are synchronized or cyclical with the accelerating particle. This is achieved in a Radio Frequency (RF) cavity such as a linear accelerator by applying a potential to a series of electrodes and advancing the potential so that it stays in front of the particle. In a cyclotron or betatron, accelerating particles are constrained to spiral orbits by a magnetic field, receiving a synchronized acceleration with each revolution. A synchrotron uses controllable magnetic fields to compensate for the increased difficulty of synchronized acceleration when particles reach relativistic energies.

Circular accelerator paths make the geometry of an accelerator more practical, but the bending of particles' trajectories comes with an inherent loss mechanism known as synchrotron radiation. Synchrotron radiation was originally considered an unfortunate loss mechanism in accelerators. However, the important applications of the radiation are now recognized and many of today's facilities generate the radiation intentionally, generally with an insertion device (undulator or wiggler) which is a series of alternating magnetic poles.

1.1.1 Current Accelerator Technology

The Stanford Linear Accelerator Center (SLAC) (now known as the SLAC National Accelerator Laboratory, shown in Figure 1.1) was the highest energy lepton accelerator in the world from 1966 until 1989, producing electron or positron beams

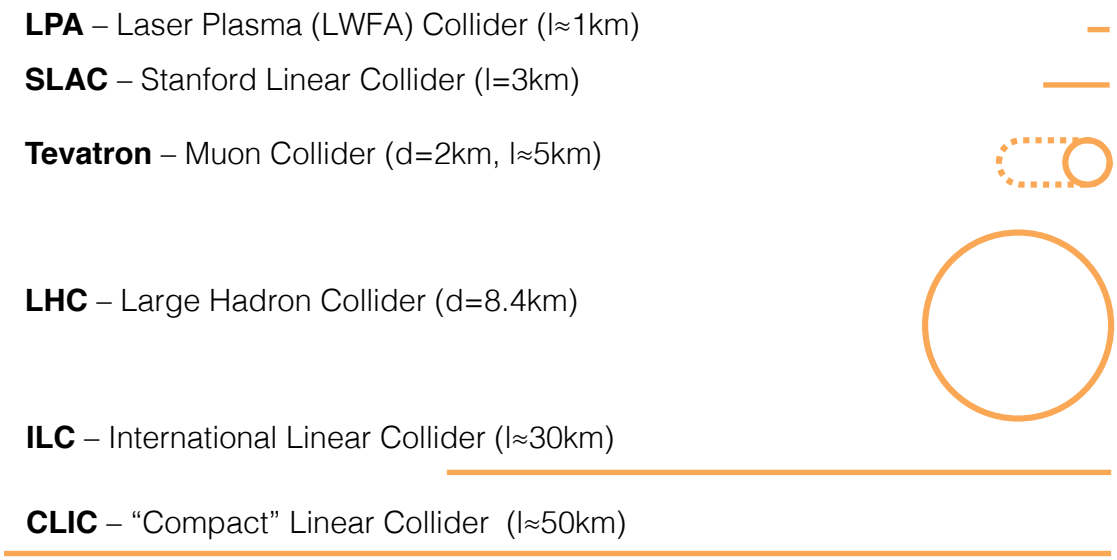

Figure 1.2: Scaled comparison of current (LHC) and proposed (LPA/LWFA, ILC, CLIC, Tevatron+Muon) particle colliders with TeV center-of-mass. The longest existing linear accelerator (SLAC) is shown for reference.

with up to 50 GeV energy. Due to growing demand for X-ray light sources, the last km of SLAC was reconfigured to become the Linac Coherent Light Source (LCLS), at which time a portion of the accelerator was replaced with a 132 m magnetic insertion device. The LCLS is the first X-ray free electron laser (XFEL) in the world, providing X-ray pulses with < 100 fs duration at 60 Hz repetition rate with photon energy in the range 0.48-10 keV. FELs differ from more common synchrotrons in that the emission is stimulated, producing a monochromatic, temporally coherent radiation source which also has a high degree of spatial coherence. This requires a long undulator and occurs because the electron beam and X-ray beam copropagate, causing the beam to bunch and oscillate with the same periodicity as the initial dominant X-ray wavelength. The LCLS total project baseline cost was $420M. The FEL produces 100 fs pulses with peak brightness of up to 5×10^{33} $photons/s/mm^2/mrad^2/0.1\%BW$.

The International Linear Collider (ILC) is a proposed lepton collider which may be built to collide 1.6 nC pulses at 500 GeV collision energy at 14 kHz using an

acceleration gradient of 31.5 MeV/m. The project would require over 30 km for the accelerator and undulator and cost an estimated $6.65B (USD). The Muon Collider is a proposed circular lepton (muon) collider using a high flux proton beam to generate muons that would be sent into the existiing Tevatron collider ring at Fermilab. A size comparison of proposed TeV accelerators is shown in Figure 1.2.

1.1.2 Applications

Electron accelerators have made many outstanding contributions to high-energy physics. While a handful of large accelerator facilities catch the headlines, there is a great number of smaller accelerators used for radiotherapy, radioisotope generation, and scientific research. Electron accelerators can be used for radiography or radiotherapy either directly or via X-ray generation. The prevalence of smaller scale accelerators has led to their widespread use as light sources, either through bremsstrahlung or synchrotron radiation. For example:

- Active interogation of special nuclear materials (SNM)
- Radiography
- Production of medical isotopes (^{11}C, ^{15}O, ^{19}F, etc.)
- Free Electron Lasers (FEL)
- Inelastic scattering from atomic and nuclear processes
- Time-resolved, pump-probe experiments
- Surface diffraction and scattering, crystal diffraction
- Protein crystallography

1.1.3 Laser Wakefield Acceleration

LWFA is a scheme of plasma acceleration in which a large-amplitude plasma wave is driven by the ponderomotive force of a high intensity laser. In 1979, the scheme was proposed although lasers with appropriate parameters were not available at the time [1]. The lasers available during the earliest LWFA experiments had pulse durations much longer than the relativistic plasma wavelength for high-densities. Large-amplitude plasma waves could still be driven, however. For example, the plasma beat-wave accelerator scheme used two laser frequencies to form a beat wave in the laser envelope with spacing equal to the relativistic plasma wavelength. Acceleration was observed for externally-injected electrons using beat waves from a carbon dioxide laser. Later LWFA schemes relied on the self-modulation by the wave itself. These schemes relied on external injection or injection by wavebreaking, a process which causes chaotic disruption of electron phase space [2, 3].

As sub-100 fs lasers became available with higher energy, allowing self-injection at lower density [4, 5, 6], LWFA moved from the self-modulated regime to the forced wakefield regime to the bubble regime [7, 8, 9]. In 2004, three groups independently reported experimental observation of 100 MeV quasimonoenergetic beams [10, 11, 12], which were made possible by self-injection rather than wavebreaking. Later, acceleration in a 3 cm capillary waveguide led to generation of a 1 GeV quasimonoenergetic beam [13]. The recent advance of LWFA research is documented in well over 500 scientific journal publications and review papers. While LWFA and other plasma-based accelerator schemes show a great deal of promise for constructing compact economical electron beam sources at moderate energy, it remains to be seen if such accelerators can be scaled to the energy frontier while retaining the cost and size benefits. Research is being conducted at many institutions around the world to assess the scalability. Recently, the BELLA facility at Lawrence Berkeley National Laboratory has demonstrated $> 4\,GeV$ energy electrons using a 1 PW laser and capillary targets.

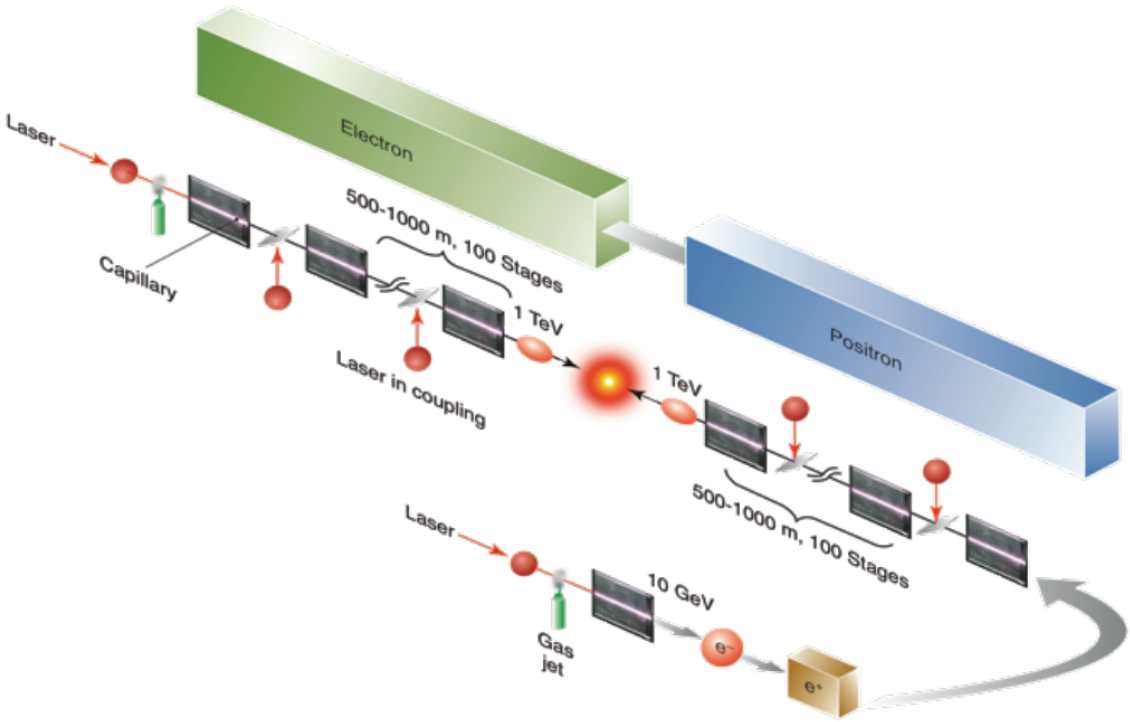

Figure 1.3: Schematic of a LWFA-based e^-/e^+ collider using 100 stages to reach TeV center-of-mass. Reproduced from Physics Today

Designs for multiple stage TeV-class laser wakefield accelerators have been presented based on staging BELLA-like systems (shown in Figure 1.3) [14]. However, new discoveries are still being made in the field, and some fundamental questions about these accelerators must be answered before a design of a large scale device can be selected. Laser wakefield accelerators could contribute to high energy physics if they can economically scale to the TeV energy range. At lower energies, the applications of their electron beams are primarily for industry and medical treatment, though laser-based ion beams are expected to offer more benefits in the treatment of tumors.

One particularly important application of LWFA outside of high energy physics is radiation generation. LWFA-driven electron beams can be injected into conventional undulator systems which convert some of the electron beam energy into a pulse of collimated synchrotron radiation. Low mass electrons are the preferred beam species for generating synchrotron radiation in these devices. The advantage of using a LWFA

beam as opposed to a conventional RF accelerator beam is that LWFA beams likely have pulse durations as short as a few fs [15]. Assuming the synchrotron radiation also exhibits this ultra-short pulse duration [16], it could be used as a probe to temporally resolve the evolution of ultrafast phenomena such as material equation-of-state (EOS) and chemical synthesis. Synchrotron radiation from LWFA-driven sources has so far been limited to the optical and VUV spectral range, which is limited by the smallest undulator magnet spacing which can be assembled (mm-scale). It was realized, however, that wiggler-like structures can be created, composed of the plasma wakefield itself having features with μm scale, leading to undulator or wiggler radiation in the X-ray range [17, 18, 19, 20]. In addition to making the applications available to a wider range of users and with potentially reduced scale and cost, the laser-driven electron and X-ray sources investigated in this dissertation could offer improvements in pulse duration, spectrum, and source size [21, 22].

1.2 Dissertation Outline

This dissertation describes research utilizing Laser Wakefield Acceleration (LWFA). This chapter discusses motivation for research in this field. Chapter II describes the facilities, diagnostics, and experimental techniques used for the research in this dissertation. Chapters III, IV, V present results obtained from different pump or probe experiments using LWFA. Finally, Chapter VI gives an overview of the electron and photon sources which have been delivered using these LWFA and draws conclusions about their applications and future potential.

CHAPTER II

Methods

2.1 Introduction

This chapter will describe the laser facilities, diagnostics, targets, and basic setups used in experiments presented in this thesis.

2.2 Lasers

LASER stands for "Light Amplification by Stimulated Emission of Radiation" [23] and the first was demonstrated in 1960 [24]. A laser is fundamentally composed of two components: a gain medium to supply energy to the radiation, and some sort of optical feedback to cycle the radiation and induce stimulated emission. This radiation is spatially coherent and highly focusable.

The ability of lasers to produce high-energy density conditions was realized shortly after its invention by Nuckolls at Lawrence Livermore Laboratory [25]. With the development of various methods to increase the instantaneous power of lasers, such as Q-switching and mode locking, different realms of physics were unlocked, as shown in Figure 2.1.

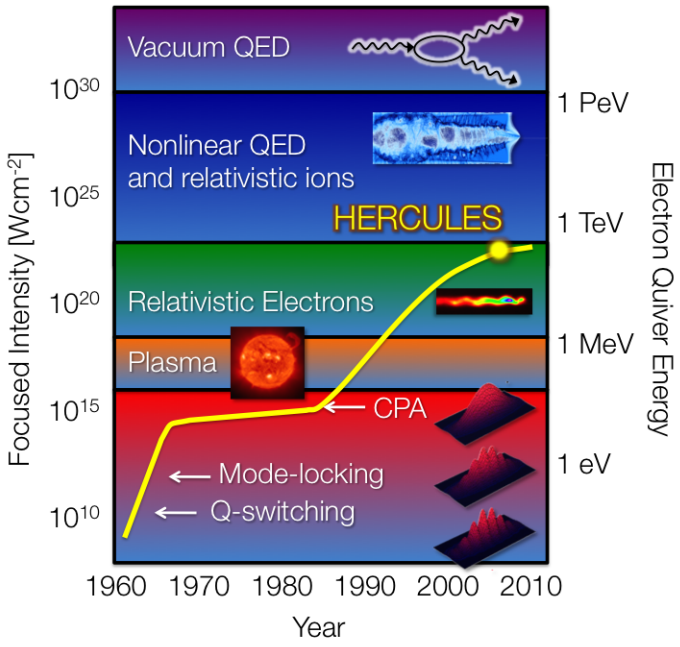

Figure 2.1: Focused laser intensity as a function of year.

2.2.1 Chirped-Pulse Amplification

By the early 1980s, peak laser power had plateaued to $\sim GW$ due to the limitations of Kerr-effect self-focusing within amplifers and which is defined by the critical power for self-focusing:

$$P_{crit} = \frac{\alpha \lambda_0^2}{4\pi n_0 n_2} \tag{2.1}$$

where λ_0 is the laser wavelength, n_0 and n_2 are the linear and non-linear indices of refraction, respectively, and α is a function of the initial intensity distribution. For example, air has a critical power of 2.4 GW, whereas silica has a critical power of 1.6 MW. If the critical power is exceeded, self-focusing will occur rapidly and cause damage to optics in the laser path.

The invention of chirped-pulse amplification (CPA) by Strickland and Mourou in 1985 [26] avoids this limitation by chirping (temporally stretching) the pulse to reduce the instantaneous power inside the amplifier to manageable levels. The pulse can now be amplified roughly by the factor of temporal stretching (roughly 10^6) before being

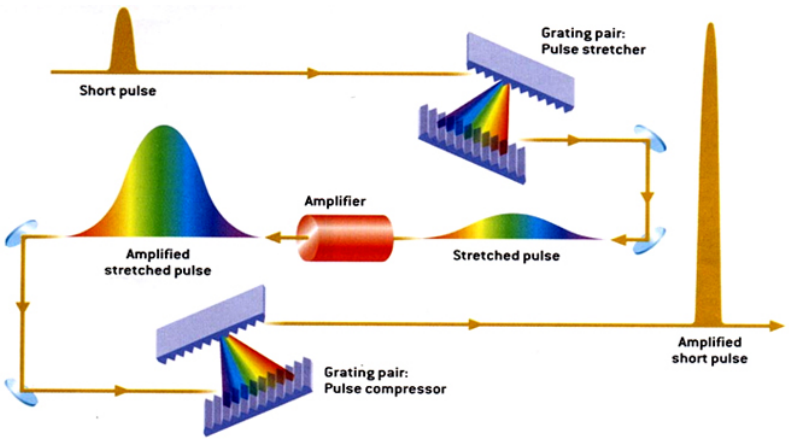

Figure 2.2: Schematic process of chirped pulse amplification. A short pulse is temporally stretched by a grating pair before undergoing amplification. This amplified stretched pulse is re-compressed by a second set of grating pairs to the original short pulse duration.

recompressed as shown in Figure 2.2. One complication of high-power CPA systems is that the recompressed pulse can easily exceed the critical power for self-focusing in air, requiring beam transport under moderate-to-high vacuum.

The current limit for CPA systems is the size (and, consequently, cost) of the diffraction gratings required to keep the fluence below the damage threshold of the gratings ($\sim 10^{12}\ W/cm^2$)[27]. Other schemes such as Raman amplification in plasma [28, 29] or coherent combination of fiber lasers [30] may overcome this limitation in years to come.

2.2.2 HERCULES Laser

The HERCULES laser system is located at the Center for Ultrafast Optical Science (CUOS) at the University of Michigan in Ann Arbor, Michigan. HERCULES was constructed in 2001, with its current configuration completed in 2008 [31]. HERCULES is a CPA laser based on titanium doped sapphire (Ti:S) gain media lasing at 800 nm wavelength. The majority of experiments detailed in this dissertation were performed on HERCULES and thus it was characterized in greater detail than ASTRA-GEMINI in

Section 2.3.

A schematic of the HERCULES laser is shown in Figure 2.3. The laser chain begins with a FemtoLasers FemtoSource Ti:S Kerr-lens mode-locking oscillator lasing at 800 nm, which generates a train of $\sim nJ$, 12 fs pulses at 75 MHz. After passing through the DAZZLER pulse shaper and a 10 Hz pulse picker (Pockels cell with a set of polarizers), the pulses travel through a 2-pass pre-amplifer to gain the μJ energy necessary to induce a $\chi^{(3)}$ nonlinearity in a pair of barium fluoride (BF_2) crystals required for the (optional) cross-wave polarization (XPW) pulse-cleaning technique. The pulses are then stretched using a folded Martinez pulse stretcher to 0.5 ns before being injected into the regenerative amplifier. In the regenerative amplifer ("regen"), the pulses perform 25 round trips to reach 30 mJ energies before they are ejected. The pulses are further amplified by a 4-pass amplifier to $\sim J$ energy, by a 3-pass amplifer to 3 J energy, and by a final 2-pass amplifier to 17 J energy. These amplifiers correspond to the "10 TW", "30 TW" and "100 TW" power modes of HERCULES amplifer system, respectively.The pulses are expanded from 50 to 150 mm diameter before entering the pulse compressor consisting of two-pairs of gold-coated holographic gratings (420×210 mm^2 and 220×165 mm^2, 1200 $lines/mm$) from Jobin Yvon. The compressor outputs a pulse with a maximum of 9 J of energy and minimum of 30 fs duration for a total of 300 TW of power. After compression, the beam is down-telescoped from 150 to 100 mm before being sent to the experimental areas.

The repetition rate of the laser is inherently limited to 0.1 Hz due to the Nd:Glass pump laser. However, with the removal of the cryogenic cooler for the 4-pass Ti:S amplifier in 2013, the effective rate is reduced to 0.02 Hz to prevent thermal lensing. The laser is P-polarized entering the experimental areas as the compressor gratings and high-reflector (HR) dielectric mirrors in the system are designed to optimally reflect P polarized light. The polarization can be changed after compression to circular or S polarization with the introduction of a thin Mica $\lambda/4$ or $\lambda/2$ waveplate, respec-

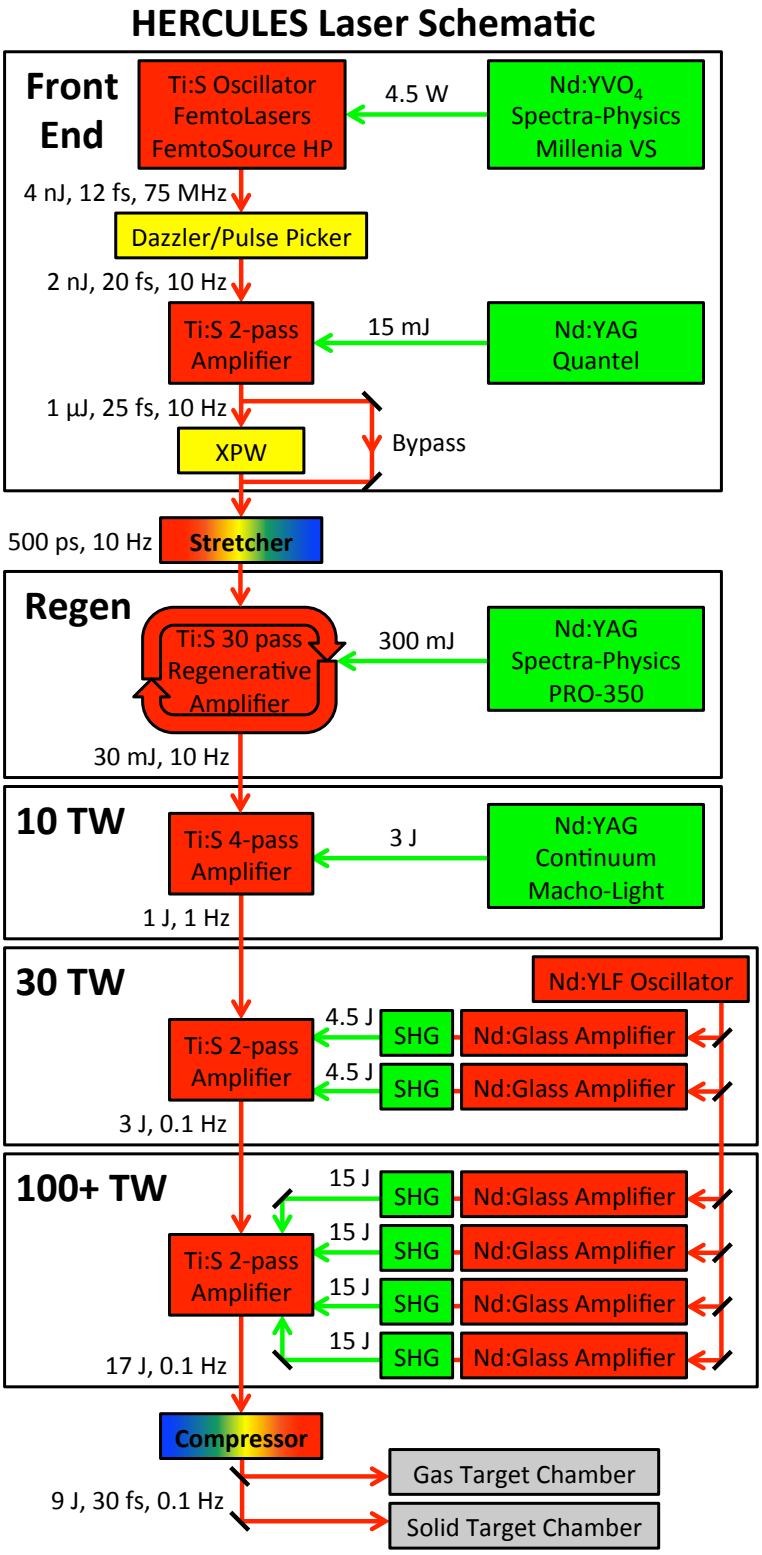

Figure 2.3: Schematic layout of the HERCULES laser system. The amplification stages are known colloquially (in order of higher power) as the Front End, Regen, 10 TW Stage, 30 TW Stage, and 100 TW (or PW) Stage.

Parameter	HERCULES	Astra-Gemini
Central Wavelength	800 nm	800 nm
Amplified Bandwidth	30 nm	25 nm
Repetition Rate	0.1 Hz	0.05 Hz
Miminum Pulse Duration	30 fs	40 fs
Maximum Pulse Energy	9 J	15 J ($\times 2$)
Maximum Pulse Power	300 TW	500 TW ($\times 2$)
Typical Pulse Power	100 TW	300 TW ($\times 2$)
ns Contrast w/ XPW	10^{11}	n/a
ns Contrast w/o XPW	10^{7}	10^{8}
ps Contrast	10^{6}	10^{6}

Table 2.1: Parameter comparison of the HERCULES and ASTRA-GEMINI lasers.

tively; however, for experiments in this thesis, only P polarized (in the horizontal plane) was employed for LWFA experiments.

2.2.3 ASTRA-GEMINI Laser

The ASTRA-GEMINI laser system is located at the Central Laser Facility (CLF) at the Rutherford Appleton Laboratory (RAL) in Didcot, England, United Kingdom. ASTRA was constructed starting in 1998, with the GEMINI upgrade/add-on completed in 2008 [32]. This system is analogous to HERCULES in many ways as shown in Table 2.1 and Figure 2.4, employing similar level amplification, pulse shaping (DAZZLER), pulse cleaning (plasma mirrors), and wavefront correction (DM) techniques. One unique feature of the GEMINI system is that the incoming ASTRA beam is split in two, with each resulting beam amplified independently. The consequent ability to use two fully amplified beams on ASTRA-GEMINI allows for a variety of different experimental configurations with independent control of each beam and is a important feature of this facility.

A schematic of the ASTRA-GEMINI laser is shown in Figure 2.5. The laser chain begins with a FemtoLasers CompactPRO Ti:Sapphire Kerr-lens mode-locking oscillator lasing at 800 nm, which generates a train of $\sim nJ$, 12 fs pulses at 75 MHz.

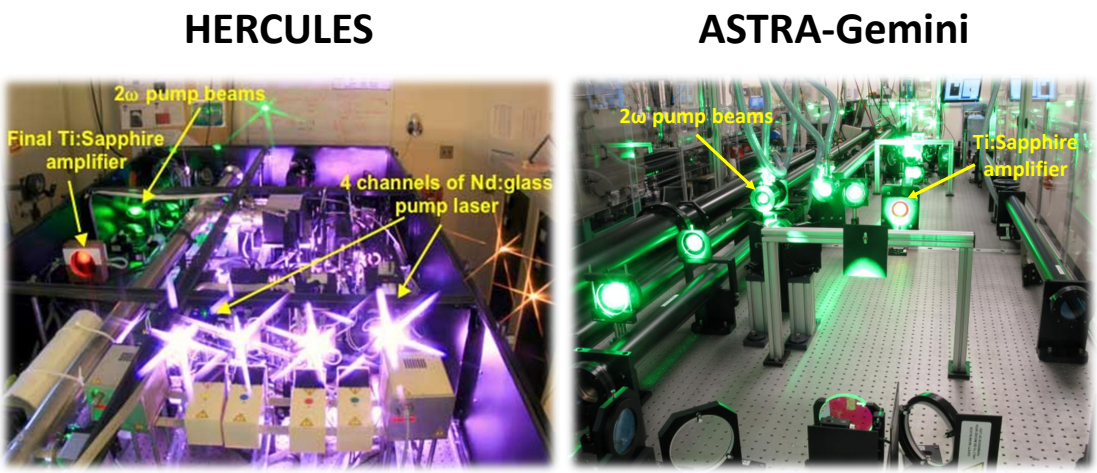

Figure 2.4: Photographs of the HERCULES (left) and ASTRA-GEMINI(right) lasers firing at full power. The green 2ω pump, the red Ti:S amplifier, and white light from the flashlamps are visible.

After passing through the DAZZLER pulse shaper and a 1 kHz pulse picker (Pockels cell), the pulses travel through a 9-pass pre-amplifer and gain mJ energy.

The pulses are sampled down to 10 Hz before being then stretched to 0.5 ns for use in the Astra Target Area 2 (TA2) or twice stretched to 1 ns for use in Gemini Target Area 3 (TA3). The stretched pulses are then amplified in the ASTRA system by a 3-pass amplifier to 5 mJ energy, by a 4-pass amplifer to 120 mJ energy, and by a final 4-pass amplifier to 1.5 J energy at 10 Hz. These amplifiers correspond to the "Low," "Medium," and "High" power modes of ASTRA amplifer system, respectively. These pulses are then divided between the TA2 and TA3 at a rate of 5 Hz for each system. Amplified pulses going through the TA2 compressor exit with 0.75 J in 30 fs (25 TW) pulses at a final rate of 2 Hz for use in the TA2 chamber (not used in this thesis). The remaining 5 Hz pulses are directed into the separate GEMINI amplifier bay located directly above TA3 and are split into two separate beams termed "North" and "South". Each pulse is amplifed with separate 4-pass amplifers to 25 J before entering separate compressors consisting of two-pairs of gold-coated holographic gratings (320×205 mm^2 and 265×420 mm^2, 1480 $lines/mm$) from

Jobin Yvon. The pulses exit the compressors with 15 J in 30 fs (500 TW) and enter through the roof of the TA3 chamber with beam diameters of 150 mm. The polarization of each beam is set by the direction of the bottom periscope mirror inside the chamber.

The South beam was used for the LWFA driver, delivering 12 ± 2 J pulses with 45 ± 5 fs. The South beam also has a deformable mirror to assist in the alignment and optimization of the $f/20$ paraboloid. The North beam was used in the NLTS experiment as the scattering pulse, delivering 11 ± 2 J pulses with 50 ± 5 fs. The repetition rate of the laser is inherently limited to 0.05 Hz due to the Nd:Glass pump lasers.

2.3 Laser Diagnostics

Due to the complexity and sensitivity of CPA laser systems, a dedicated effort to characterize the laser spatial and temporal profiles must be taken before, and during, experiments. This is particularly important for laser-plasma interactions as instabilities can crop up from the smallest perturbations in either spatial and temporal profiles. Moreover, the shot-to-shot pointing stability of the laser beam is also critical for spatio-temporal overlap in multi-beam experiments. This section will detail some of the methods used to characterize and optimize laser parameters.

2.3.1 Focal Spot Characterization

Invariably, it is important to maximize intensity on the target and ensure an optimal focal spot distribution with minimal abberations. Since the full intensity of the laser pulse far exceeds the damage threshold for materials ($\sim 10^{14}$ W/cm^2), it is necessary to run these lasers with lower power (regen or "Low" power mode) for most alignment and characterization purposes. Operating at a lower power level allows most low-order abberations to be observed and corrected with a simple microscope

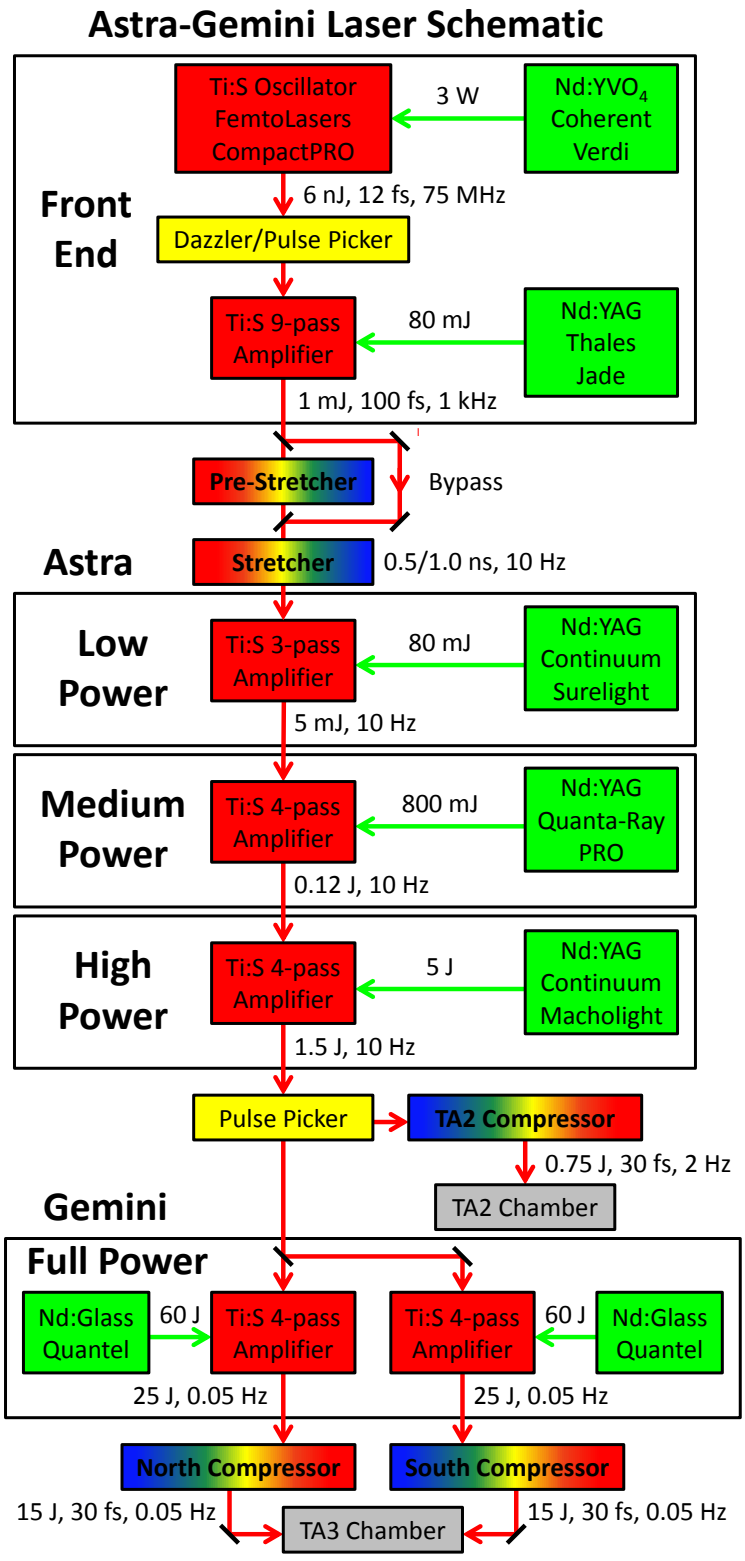

Figure 2.5: Schematic layout of the ASTRA-GEMINI laser system. The amplification stages are known colloquially (in order of higher power) as the Front End, Low Power, Medium Power, High Power, and Full Power (only available on GEMINI).

objective imaging system. For $f/20$ focusing geometries on HERCULES, a $10\times$ objective imaged the laser focus onto a 8-bit Watec CCD. The focal spot on HERCULES was measured daily to ensure that were no significant changes to the optical system and to provide a reference for the intensity distribution. The typical $f/20$ focal spot was slightly astigmatic, measuring 25 $\mu m \times 28$ μm FWHM as shown in the upper-left of Figure 2.6. An optional custom-fabricated pellicle apodizer could be installed in the chamber area to act as a "soft" aperture to clean up the "wings" of the spot, increasing the effective $f/\#$ to $f/27$ and consequently the spot size to 27 $\mu m \times 29$ μm FWHM as shown in the upper-right of Figure 2.6. However, this apodizer was not used for experiments in this thesis.

For the $f/20$-focused South beam on ASTRA-GEMINI, a $10\times$ long-working-distance microscope objective imaged the laser focus onto a 12-bit Stingray CCD. The $f/20$ focal spot was corrected daily with a deformable mirror (DM) to ensure that the intensity distribution was optimized. The typical $f/20$ focal spot was slightly ellipitcal, measuring 28 $\mu m \times 35$ μm FWHM with DM correction as shown in the lower-left of Figure 2.6. An optional serrated apodizer could be installed in the amplifer area before the final spatial filter, increasing the effective $f/\#$ to $f/27$ and the spot size to 30 $\mu m \times 40$ μm FWHM, while decreasing the pulse energy by 15% as shown in the lower-right of Figure 2.6. For the $f/2$-focused North beam on ASTRA-GEMINI, a $40\times$ long-working-distance microscope objective imaged the laser focus onto a 12-bit Stingray CCD. The spatial distribution is discussed in greater detail in Chapter V.

2.3.2 Temporal Characterization

Knowing the temporal structure of the laser pulse is crucial for understanding how the laser energy is deposited into the target. Over long timescales ($\sim ns$) before the peak of the pulse, the pulse may contain residual amplified stimulated emission (ASE) from the amplifiers that is leaked through the Pockels cells in the system.

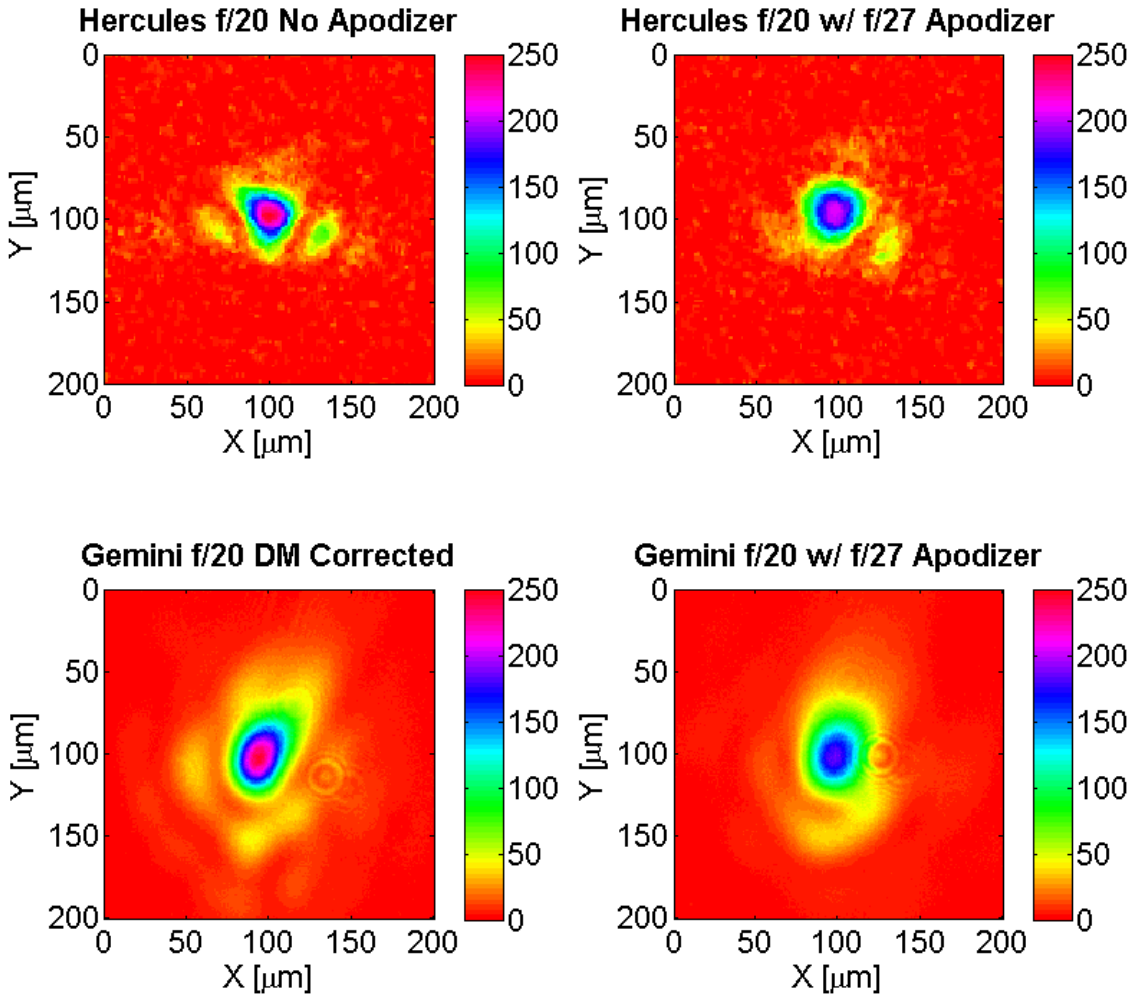

Figure 2.6: $f/20$ focal spots of HERCULES (top) and ASTRA-GEMINI (bottom) without (left) and with $f/27$ apodizers installed (right). Note the color and spatial scales are the same for all images.

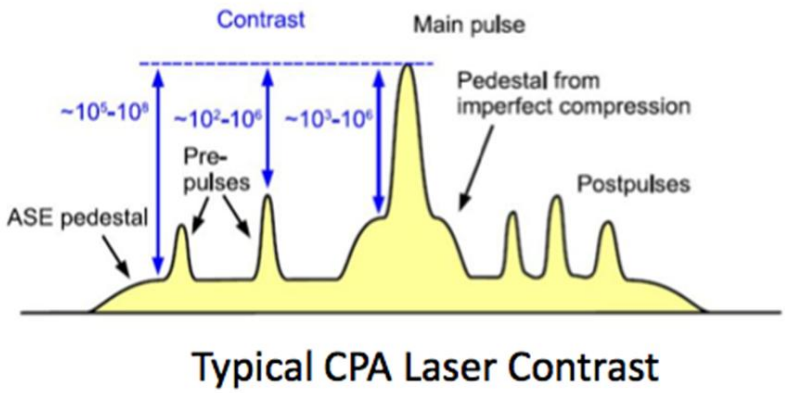

Figure 2.7: Representation of the typical contrast structure of CPA laser systems. Note that this figure does not properly indicate the temporal symmetry of shot-pulse pre/post-pulses.

Even though the intensity of the ASE pre-pulse may be $10^6 - 10^{11}$ times smaller than the peak of the pulse (shown in Figure 2.7), this level of pre-pulse still means that the target can experience intensities on the order of $\sim 10^{13}\ W/cm^2$, greater than the damage threshold for many materials, and create plasma. The ASE contrast ratio can be measured simply with a fast-rise (sub-ns) photodiode and an appropriate set of filters to establish the baseline. On HERCULES, the ASE contrast ratio (main pulse compared to pre-pulse) was measured to be 10^{11} with and 10^8 without the XPW pulse cleaning technique [33]. This is sufficent for most LWFA experiments where the ASE intensity is on the order of $\sim 10^{11}\ W/cm^2$ and is not enough to cause the gas target to significantly change its profile.

Over short timescales ($\sim ps$), the ability to measure temporal features of the pulse becomes much more complicated. There are two main effects in this temporal region: the ps pedestal from imperfect pulse compression and short-pulse pre-pulses. The ps pedestal comes from the inability of the compressor to correct higher order phase terms in the laser pulse ($\varphi^{(4)}(\omega)$ and greater). This is an extremely important reason to keep the grating pairs as parallel as possible. On the other hand, the short-pulse pre-pulses originate from reflections in improperly aligned or uncoated/unwedged

optics in the system (before the amplifers) which form a post-pulse from a double back-reflection. Normally, post-pulses themselves will not affect the main pulse interaction. However, if the stretched post-pulse temporally overlaps with the stretched main pulse in the amplifers, gain will produce a non-linear spectral beatwave between the two pulses and consequently shift energy spectrally to form a pre-pulse [34]. This means that care must be taken to remove any un-wedged or un-coated optics in the laser chain.

Since electronic detectors read out on the order of $\sim ns$, the compressed pulse must be measured indirectly with some process occuring on a similar timescale. One option is to use a streak camera. A streak camera works by initially converting the laser photons into electrons with a photocathode and accelerating them into a region with a fast sweeping voltage before the electrons impact a phosphor screen which is then imaged. Depending on when they interact the sweeping voltage, the electrons are dispersed differently in one direction on the phosphor or micro-channel plate (MCP) screen. By using a slit to reduce the spatial extent of the input electrons to the other axis of phosphor, the streak camera outputs a 2-D image with one dimension representing for space and the other for time. Since the temporal sweep is linear, the time axis is unambiguous, meaning that it directly represents the temporal shape of the pulse. This unique feature of steak cameras is particularly useful for unambiguous detection of short-pulse pre-pulses and is something autocorrelators are unable to resolve even with considerable analysis. Some drawbacks of the streak camera are their limited temporal resolution ($>100\ fs$), expensive cost ($\sim$ \$100,000), and shot-to-shot timing jitter of the sweep voltage.

A streak camera trace from HERCULES without XPW is shown in Figure 2.8 generated using a Hamamatsu model C1587 streak camera unit imaged with a CoolSNAP CCD. To observe the lower intensity post-pulse, the main-pulse is allow to saturate the photocathode and "bloom" on the read-out MCP. There are a number of identifiable

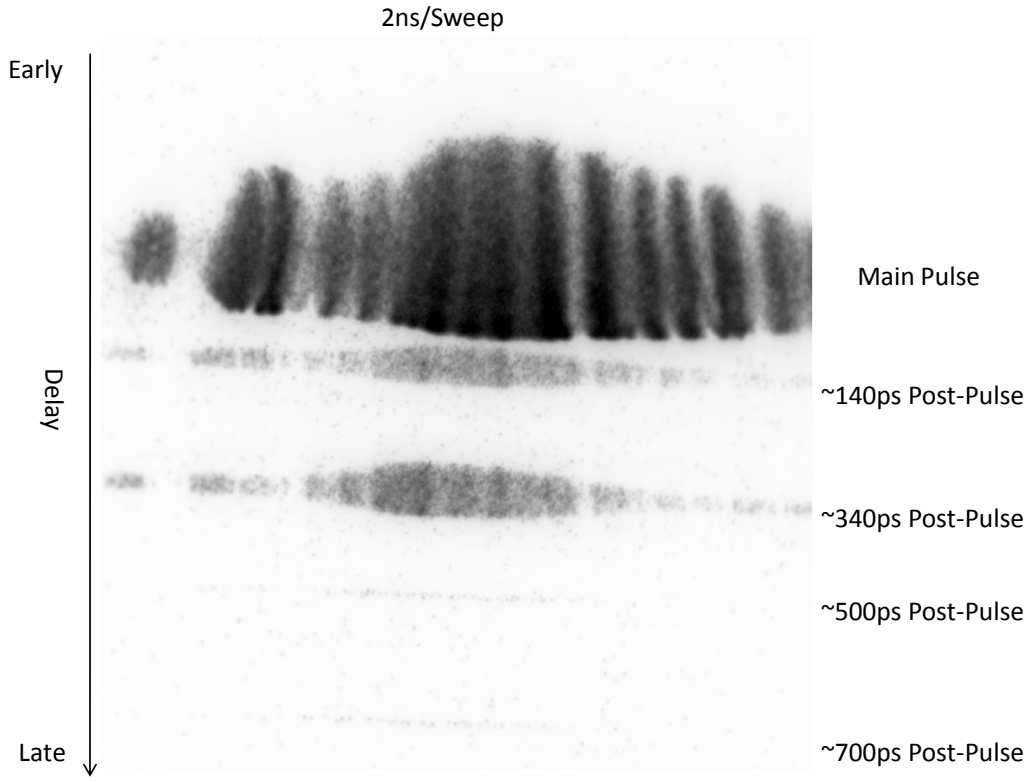

Figure 2.8: Streak camera trace of HERCULES without XPW. The post-pulses can be observed at 140, 340, 500, and 700 ps.

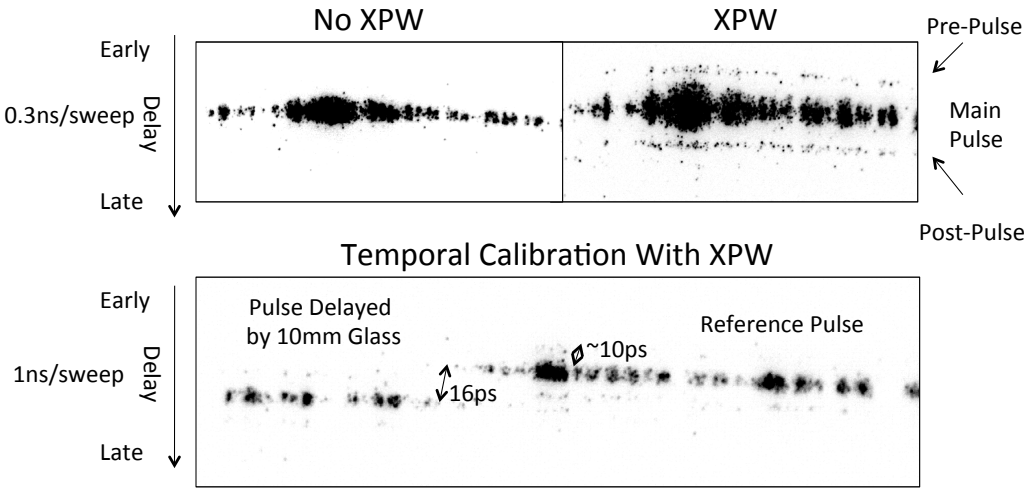

Figure 2.9: Streak camera traces of with (top-right) and without (top-left) XPW. The location of the pre-pulse can be determined by placing glass to introduce a known delay (bottom).

post-pulses at 140, 340, 500, and 700 ps - corresponding to a back-reflections from various optics (amplifiers, Faraday rotator, glass polarizers) in the system. Moreover, since the original XPW crystals were unwedged and uncoated, they introduced a $\sim$10 ps post-pulse which readily becomes a pre-pulse in the regen amplifier [34]. This was measured with the streak camera and was partially corrected by angling the crystals as shown in trace in Figure 2.9.

For resolving effects less than 100 fs, the pulse can act as its own reference in a process called autocorrelation. An intensity autocorrelator employs a non-linear (such as second harmonic generation, SHG, [35] or third harmonic generation, THG) process to produce an intensity output that is relative to the combined intensity of the both the signal and reference with their respective delay to one another. For a second-order (SHG) autocorrelator, this relation is given by:

$$I_{2\omega}(\tau) = \int I_{\omega}(t) I_{\omega}(t-\tau)\,\mathrm{d}t \tag{2.2}$$

where τ is the delay between pulses, $I_{\omega}(t)$ is the intensity of the input signal, and

$I_{2\omega}(\tau)$ is the intensity of the SHG output at a delay of τ. By scanning the delay between signal and reference pulses for a second-order autocorrelator, the time-symmetric temporal profile of the pulse is resolved. This enables high accuracy meaurements of the width of Gaussian-shaped main pulses as well as efficient detection of any pre/post-pulses with the simple adjustment of a delay stage. However, since the even-order process creates an ambiguity in time, it is impossible to determine the direction of the time and consequently whether it is a pre- or post- pulse.

To overcome temporally symmetric signal resulting in a temporal ambiguity, an odd-order process (such as THG) can resolve the temporal axis to a certain degree. For a third-order autocorrelator, the relation is given by:

$$I_{3\omega}(\tau) = \int (I_\omega(t))^2 I_\omega(t-\tau)\,\mathrm{d}t = \int I_{2\omega}(t) I_\omega(t-\tau)\,\mathrm{d}t \tag{2.3}$$

where τ is the delay between pulses, $I_\omega(t)$ is the intensity of the input signal, and $I_{3\omega}(\tau)$ is the intensity of the THG output at a delay of τ. Although this process now resolves the time axis more closely, there is still a subtle ambiguity in the pre/post pulses since they can still generate enough SHG signal ($I_{2\omega}$) to create "ghost" pulses in the temporal profile on the opposite side of the time axis. However, by measuring the intensity at delays on both sides of the axis, the temporal location can be roughly deduced. Although not performed during this thesis, a third order autocorrelation of the HERCULES and ASTRA-GEMINI lasers can be found in [33] and [32], respectively. An example trace is shown in Figure 2.10. Used in conjunction with a streak camera, a third order autocorrelator enables a good understanding of the long-timescale structure of the laser pulse.

Due to the simplicity of autocorrelation, it can only resolve the intensity of the main pulse. To measure the phase of the pulse, a technique called Frequency Resolved Optical Gating (FROG) can be employed. FROG is an extention of autocorrelator,

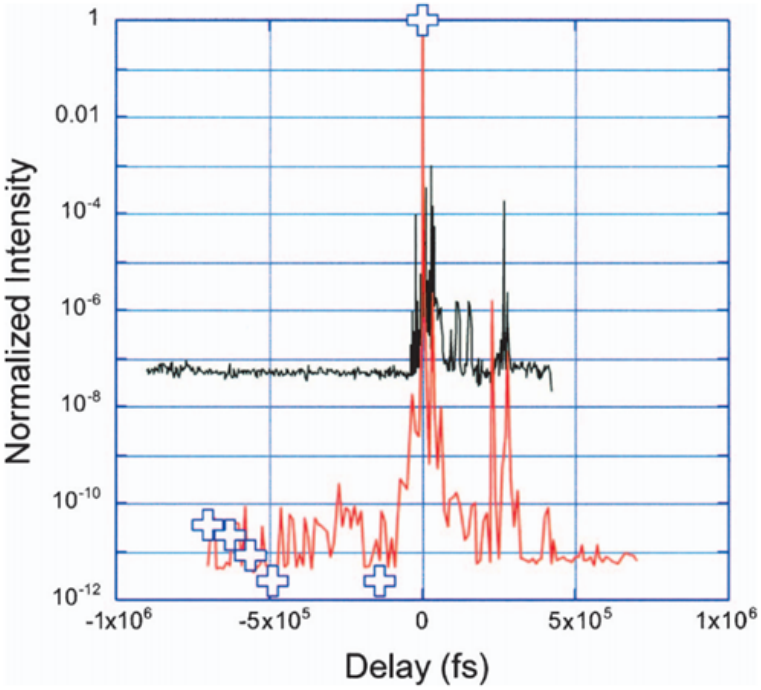

Figure 2.10: Third order autocorrlator trace of HERCULES regen with (red) and without (black) XPW. Note that the post-pulses seen can create pre-pulses under amplification. Reproduced courtesy of Vladimir Chvykov, University of Michigan.

where the spatial axis is now spectrally resolved in conjunction with the temporal axis. This temporal-spectral information can be fed into a genetic algorithm to retrieve the phase, and consequently the electric field profile, of the pulse.

Once the temporal shape is characterized on the low-power/regen level power, it may become necessary to measure how much the power amplifiers affect the characterization. Since most diagnostics cannot withstand the intensity of the main pulse, the beam can either be attenuated with wedges or with a leakthrough before use. Another diagnostic of the short-pulse pre-pulse is the measure the breakdown of plasma using a transverse probe (in this case, one arm of the interferometer described in Section 2.5.1). This directly measures the pre-pulse interaction with a plasma, detecting short-pulse pre-pulses formed from post-pulses in the final amplifiers that are intense enough to ionize a gas target before the arrival of the main pulse. To ensure only short-pulses are ionizing the gas locally, the laser focus must be small (resulting from an $f/10$ focus or smaller) and the gas target must be low-Z (H_2 or He) and high-density.

2.3.3 Laser Power

By simultaneously measuring the laser spectrum and energy, the laser power for a given shot can be calculated. A simple full power diagnostic of the pulse spectra is a Thorlabs CCS175 fiber spectrometer which takes a leak-through of a mirror before the compressor. The full power spectrum allows the pulse duration to be estimated given the bandwidth and central wavelength. The bandwidth is the most limiting factor in calculating the pulse duration due to the time-bandwidth constraint:

$$\tau_L \cdot \Delta\omega_L > 0.44 \; (Gaussian\; shaped\; pulse) \tag{2.4}$$

where τ_L is the laser pulse duration and $\Delta\omega_L$ is the laser bandwidth. This implies that a 30 fs Gaussian-shaped pulse requires 31 nm of bandwidth near 800 nm. The regen typically provides 30-35 nm of bandwidth; however, with gain narrowing of the power amplifiers, this can be reduced to 15-20 nm (corresponding to 60-45 fs output pulses, respectively), so it the spectral width must be monitored closely.

The central wavelength is also important for the proper compression of pulse. If the central wavelength shifts by 10 nm, the compressed pulse is effectively doubled from 30 to 60 fs as the compressor grating separation is no longer optimally matched to the central wavelength. Since the gain narrowing of the final amplifers is pre-compensated (the spectra is intentionally blueshifted to offset the redshift of the amplifiers). This is particularly important when using XPW since the process is third-order and any modulations in the spectra can lead to splitting and shifting of the spectra in the later amplifers. In certain cases, the spectra actually splits into two different lobes, leading to stretched, multiple pulses. Furthermore, the reduction of the spectrum is hazardous to the final amplifers and gratings as the laser energy is contained in a narrow portion of the spectra, potentially leading to damage if uncorrected. As such, the spectrum of the oscillator output in the HERCULES system is monitored in order to automatically shut-down the amplifiers if there is a loss of sufficient bandwidth that could damage the system. Also, loss or splitting of bandwidth after the final amplifiers is a sign that the laser needs re-alignment.

The laser pulse energy is measured two ways: summing the near-field image through a leak-through after the each amplifer and focusing the leak-through light before the compressor onto a Thorlabs DET10 photodiode read out by a oscilloscope. The images after each amplifer are subject to more shot-noise (scattered light, interference on video signal) and, therefore, can be inconsistent from shot-to-shot. However, they allow the laser user to detect damage in the amplifer optics (seen in the form of growing diffraction) and isolate which amplifier is causing the laser power

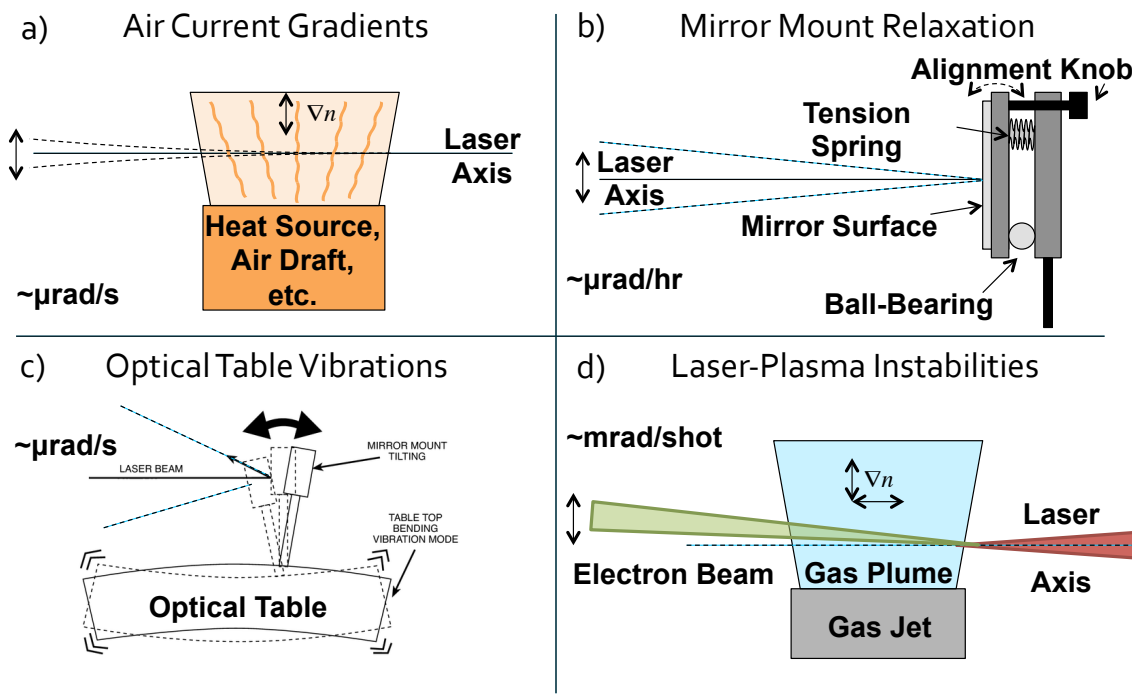

Figure 2.11: Instabilities known to affect shot-to-shot reproducability: a) air current gradients, b) mirror mount relaxiation, c) optical table vibration, and d) laser-plasma instabilities.

to drop. On the other hand, the photodiode measurement is extremely linear compared to the imaging system and is a good indictor of the laser power. Both systems are cross-calibrated with a integrating sphere at the beginning of each shot run.

It must be noted that subtle issues (temperature, humidity, incident angle, optical coating, alignment, polarization) with the leak-through measurements can affect the relatively weak transmission of the spectra and energy through the high-reflection dielectric mirrors. This affects all of the diagnostics mentioned in this section to a certain degree; however, only the trend over a few shots is usually considered due to shot-to-shot fluctuations.

2.3.4 Laser Alignment and Pointing

To ensure the laser is reproducibly focused onto the target, an alignment procedure must be performed and checked constantly. As shown in Figure 2.11, there are a number of fluctuations that can affect the laser - and consequently the electron beam - pointing and profile. In HERCULES, the most prominent source of fluctuations is from vibrations in the optical tables. Although all the transport optics are mounted on damped tables which are isolated from vibrations of the vacuum chambers and in the ground, the air-conditioning (AC) unit in the laser room vibrates so much in amplitude that it couples to the tables. This has been clearly measured to affect the pointing up to 100 μrad at a rate of 0.5 Hz. This can easily be remedied by shutting off the AC temporarily before a shot. Another fluctuation is caused by temperature, pressure, or density gradients across the beam caused by air drafts or heat sources. These gradients create subtle changes in the index of refraction in air across the beam, acting like optical wedges to redirect the beam. In this case, it is important to enclose the laser beam from external air currents and avoid placing electronics dissipating heat near the beam. Neglecting this can not only cause slight pointing variations, but also distortions to the focus. Finally, over the course of an hour, the springs used to hold mirrors in the system begin to relax due to subtle changes in temperature. This relaxation results in a systematic drift which can affect fine alignment, especially in the case of multiple-beam experiments, but does not usually affect single-beam experiments.

To characterize the pointing drift of the beam, a far-field pointing monitor consisting of a lens and a 10X microscope objective was installed after the leakthrough of the first mirror in the Gas Target area of HERCULES. This serves two purposes: first, as a alignment diagnostic to ensure the beam axis entering the chamber was parallel to the alignment axis, and second, as a full-power diagnostic (when properly filtered) to track the shot-to-shot fluctuations and shape of the focus.

The periscope mirrors directly after the compressor steer the beam to be parallel to the alignment axis of this diagnostic, acting a first point of alignment in the system. The focal spot monitor (described in Section 2.3.1) was used as the second point of alignment in the system and allowed the beam focus to be checked before shooting.

2.4 Targets

Once the laser pulse was characterized, the next step was to install a target in the laser path depending on the particular experimental goals. For LWFA, the target needs to have a density of $\sim 10^{19}\ cm^{-3}$, low Z, and mm lengths. For these conditions, gas jets and gas cells are ideal and can be tailored for the appropriate longitudinal density profile. For overdense laser-plasma interactions, the targets need to exceed the critical density ($\sim 10^{21}\ cm^{-3}$) and have $\sim \mu m$ lengths, so thin solid foils are used. For secondary conversion processes, the target needs to be dense (solid density, $\sim 10^{23}\ cm^{-3}$) and thick ($\sim cm$ lengths) to maximize conversion.

2.4.1 Gas Jets

Gas jets are a simple, yet reliable, gas target that offers a wide variety of gas densities and lengths. They have been used on laser plasma experiments for decades and were the targets used for the first observation of quasi-monoenergetic electrons from LWFA [10]. The typical design is a conical nozzle approximating an ideal *Laval* nozzle in order to optimize the supersonic expansion of gas into vacuum [36]. The design is shown in Figure 2.12a. A simple formula based on conservation of flux can estimate the required backing pressure based on the nozzle input and output:

$$n_{exit} \approx n_{entrance} \times \left(\frac{A_{entrance}}{A_{exit}}\right) \approx n_{entrance} \times \left(\frac{r_{entrance}}{r_{exit}}\right)^2 \tag{2.5}$$

where n is gas density, A is the nozzle area, and r is the nozzle area.

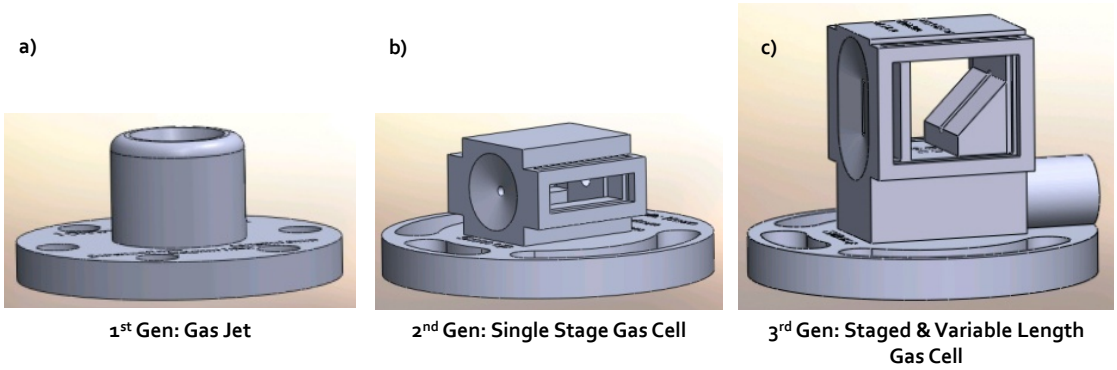

Figure 2.12: Typical rapid-prototyped gas targets used for LWFA: (a) gas jet, (b) single stage gas cell, and (c) staged and variable length gas cell. Reproduced courtesy of Michael Vargas.

The majority of the gas jets were machined out aluminum, with some plastic or brass used in different scenarios, in order to minimize bremsstrahlung from low-energy electrons impacting the nozzle. Since the chamber must be at high vacuum (10^{-3} *mbar* or lower) for the laser to propagate without self-focusing, the gas jet is pulsed 20-30 *ms* before the laser arrives with a solenoid valve (Peter Paul Model # EH22H9DCCMG). The backing pressure ranged from 1.5-600 *bar* depending on the nozzle length and gas type.

Unless otherwise stated, the gas jets were placed 1 *mm* below the laser axis to minimize laser damage and to ensure that the gas flow is supersonic and the profile is relatively flat-top. When the gas jet is closer to the laser axis or over the course of 1000's of shots on a particular nozzle, the laser can damage the inner surface of the gas jet, resulting in turbulent flows which can disrupt the LWFA process through shocks or density purturbations. On the other hand, if the nozzle is too far away from the axis, the gas flow can become subsonic and begin to diffuse in a more Gaussian shaped profile. The gradients in this profile can steer the laser pulse similar to a gradient index (GRIN) lens, redirecting the laser (and its trailing electron bunch) in the direction with lower density (away from the nozzle).

2.4.2 Gas Cells

Gas cells offer the flexibility of implementing practically any complex density profile, including multiple gas types [37]. This is especially true with the rise of rapid prototyping in the form of 3D printing [38]. A gas cell target design can be modeled using computer aided design (CAD) software and 3D printed in a matter of hours. This iterative process allows for quick turnover of ideas and has led to a number of significant improvements in the reproducibility of electron beams in the LWFA process [39]. The design is shown in Figure 2.12(b,c).

In general, gas cells provide a nearly uniform density within the volume once an equilibrium is reached [40, 41]. This is a significant improvement over the Gaussian-shaped density profiles generally produced in gas jets and allows for the laser to interact more uniformly with the resultant plasma [42]. However, since the gas also flows out of the entrance and exit holes of the cell, the laser interacts with longitudinal density gradients on axis. This is potential advantageous for the self-focusing process and for assisting trapping [42]. However, small-volume gas cells present a few unique practical issues such as gas mixing between the stages and difficulty maintaining low backing pressures.

2.4.3 Solid Targets

For experiments in Chapter III, a variety of solid targets were shot with a portion of the laser beam. These targets included 5-200μm foils of Al, Cu, Au, glass (SiO_2), and Mylar ($C_{10}H_8O_4$) and $\varnothing 5 - 25\mu m$ wires of Cu or Ni.

Since the laser ablates or entirely destroys the target after a shot, a new target must be precisely positioned at the laser focus for the optimum interaction to occur. Two separate imaging systems and an alignment laser are used to help position the target. The low magnification system ("low-mag") allows the user to visually position the target within $\sim$ 100 μm of the laser focus. Using an alignment laser

co-propogating with the main laser, the high magnification system ("hi-mag") allows the user to triangulate the target positon to the laser focus using the scattered light from the alignment laser.

For experiments in Chapter IV, a variety of solid targets were used for bremsstrahlung conversion. Although any material may be used to convert radiation via bremsstrahlung, the scaling is strongly dependent on the number of radiation lengths encountered. This implies that the process efficiency is proportional to Z^2/A, thickness (d), and density (n). For electron beams creating bremsstrahlung photons and positrons, this means targets of high Z materials with thicknesses on the order of a radiation length $d \sim L_{rad}$. Targets typically included Pb or Ta due to their high-density and high-Z.

2.5 Interaction Diagnostics

Once the laser is characterized and a target is selected for a given experiment, the interaction of the laser with the target must be quantified. This generally falls into two categories: optical and high-energy radiation diagnostics. This section will focus on the former, using optical light to help diagnose the laser-plasma interaction. A summary of the scientific cameras used for optical diagnostics used in this thesis is shown in Table 2.2.

2.5.1 Interferometry

To measure the plasma density profile of the gas target, plasma interferometry was performed using a small portion of the main laser pulse to probe the plasma. On HERCULES, a 2 μm thick nitrocellulose pellicle (National Photocolor) with one side anti-reflection (AR) coated was used to pick off the 4% Fresnel reflection from the main beam to transversely probe the laser-plasma interaction before entering a shearing Michelson interferometer. On ASTRA-GEMINI, small pick-off mirror was placed in the main beam to transversely probe the laser-plasma interaction before

Manufacturer	**Photometrics**	**Andor**	**Allied Vision**
Camera	**CoolSNAP *cf***	**iXon**	**Stingray F-033**
QE at 800 nm	6%	76%	12%
QE at 545 nm	36%	90%	38%
QE at 400 nm	32%	72%	24%
Pixels	1392 × 1040	1024 × 1024	656 × 492
Pixel Size	4.65× 4.65 μm^2	13 × 13 μm^2	9.9 × 9.9 μm^2
Dynamic Range	12-bit	16-bit	12-bit
Readout Noise	± 4 counts	± 2 counts	± 4 counts
Connector	PCI Frame Grabber	PCI Frame Grabber	Firewire

Table 2.2: Specifications of optical scientific cameras used in experiments. QE stands for quantum efficiency, which is the photon-to-electron conversion efficiency in the sensor for a given photon energy/wavelength.

entering an offset Mach-Zehnder interferometer. In both cases, a delay stage was used to adjust the temporal overlap between the main and probe pulses such the probe pulse arrived $\sim ps$ after the main pulse had passed throught the entire plasma length.

The amount of phase shift ($\Delta\phi$) accumulated in the interferometer fringes is the integral:

$$\Delta\phi = \frac{2\pi}{\lambda_L}\int_P (1-\eta(x))\,\mathrm{d}x \tag{2.6}$$

where λ_L is the laser wavelength and $\eta(x)$ is the refractive index of the plasma as a function of position. Assuming the plasma is cylinderically symmetric, the density profile can be found by taking an Abel inversion to extract the radial density profile. A LABVIEW program written by Nicholas Matlis was used to compute density maps via Abel inversion of interferometer images.

2.5.2 Timing Diagnostics

Due to the fs timescales of the pump-probe interactions in this thesis, precise temporal synchronization techniques are required. For all of these techniques to be practical, the coarse ns timing must first be established by setting optical path lengths

to within *cm*'s for separate beams before using a delay stage to dial in finer timing. If the paths cannot be measured easily, a fast photodiode and oscilloscope (rise time of $\sim 50\ ps$) can be used to overlap the beams at (or near) the interaction point.

For experiments in Chapter III, two different fine timing methods were employed: temporal interferometry and optical breakdown in air. For temporal interferometry, the counterpropagating beams were overlapped using a glass microscope cover slip of 160 μm thickness to reflect a portion of the $f/3$ beam onto the transmitted $f/18$ beam. When synchronized, the two beams produced fringes where the beams overlapped on a CCD. However, the thick glass introduced a few sources of error. First, it produced a secondary reflection of similar intensity from the rear surface that could be easily be mistaken for the main reflection, except $\sim 500\ fs$ delayed. Second, the glass refractive index and thickness at the given angle were not precisely known, giving an error of $\pm 100\ fs$. Finally, the glass was not placed exactly at the $f/3$ focus, yielding a positioning error on the order of 100 fs. The other timing method used the $f/3$ focus to induce optical breakdown at its focus in air. The resultant plasma was backlit with the $f/18$ beam on a CCD camera. Since the plasma forms at the peak of the $f/3$ pulse, the $f/18$ light is only scattered after the plasma is formed, indicated by a spatial intensity depression that disappears when the $f/3$ is blocked. This technique enabled nearly pulse duration ($\sim 30\ fs$) synchronization of the two pulses. One caveat for this technique is that the beams must be split under vacuum, lest the relative optical path lengths change due to the slight difference of refractive index between vacuum and air.

For experiments in Chapter V, separate fine timing methods were used based on the laser system: optical breakdown for HERCULES and spectral interferometry for ASTRA-GEMINI. On HERCULES, the optical breakdown method was similar to above with the exception that the two foci (from $f/2$ and $f/20$ beams) are closely overlapped. Since the $f/20$ did not always overlap with the $f/2$ breakdown, a non-

dispersive diffuser (tissue paper) was used to spread the beam over a larger area to ensure backlighting the breakdown. For spectral interferometry on ASTRA-GEMINI, a 5 μm thick pellicle was used to reflect a portion of the $f/2$ beam to overlap with the $f/20$ beam on a diffraction grating. The first order diffraction was imaged to a CCD camera. Since the spectra of the pulses essentially stretched over time in one direction of the camera, fringes will appear over ps timescales, with the fringes rotating as the delay is changed. When the fringes are parallel between the two beams, the pulses are closely overlapped in time. Since the relative fringe rotation slowly varies with temporal overlap, this technique was only accurate to $\sim 100\ fs$.

2.5.3 Scattered Light Diagnostics

Thomson scattered light from the plasma can help diagnose the laser-plasma interaction in a variety of ways. The primary scattered light diagnostic was the top scatter or "top view" imaging system used in conjunction with gas jet targets. This scattered light showed how far and how well the laser propagated through the gas target. It was also used for alignment of the gas jet nozzle with the laser. Lastly, a portion of this scattering light was sent to an imaging spectrometer (Horiba MicroHR) which could image the scattered laser spectra as it propagates. Backscattered light from NLTS counter-propagating geometry was also monitored due to the risk of sending collimated light back into the laser chain, potentially damaging optics in the front end of laser chain due to residual gain in the amplifiers after a shot. This backscattered light could be measured by imaging the back-sacttered leak-through of a dielectric mirror.

2.6 Radiation Detectors

If the laser is sufficently intense when it interacts with the plasma, a wide variety of radiation can be emitted. This section will describe a variety of methods to measure

Manufacturer	**Hamamatsu**	**Hamamatsu**	**Hilger Crystals**
Model	**J6677**	**J6677-01**	**Custom**
Scintillator	CsI	CsI	BGO
Coupling	6 μm FOP	6 μm FOP	Direct
Relative Light Output	70%	40%	n/a
Scintillator Thickness	150 μm	150 μm	50 mm
Area	50×50 mm^2	50×50 mm^2	27×27 mm^2
Resolution	100×100 μm^2	50×50 μm^2	1×1 mm^2

Table 2.3: Specifications of camera-coupled scintillators used in experiments.

this radiation. This typically involves either direct measurement of the radiation or conversion of the radiation into light or some other measurable unit for indirect detection.

2.6.1 Scintillators

Scintillators are the primary radiation diagnostics used for high-energy radiation. As with most radiation detectors, scintillators trade off efficiency for spatial resolution.

For the majority of high-repetition rate ($\sim$ 1 $shot/min$) experiments, we used Kodak LANEX scintillator screens to image the electron beam spatial or spectral distribution. LANEX is composed of a thin layer of Gd_2O_2S doped with La_2O_2S, scintillating light isotropically at a peak around 545 nm. The front of the LANEX screens were shielded by Al or brass to block laser light and low-energy electrons or X-rays from creating noise. The rear was imaged with visible light scientific cameras (either CoolSNAP or iXon cameras, detailed in Table 2.2) using either BG39 glass or 545 nm bandpass filters to block laser or other contaminant light. Due to the variety of cameras, lenses, and geometries used, cross-calibration was performed with image plates (Section 2.6.2) for each scenario.

For indirect 20-100 keV energy X-ray detection, scintillators coupled to fiber optic plates (FOP) can be directly attached to a camera to increase conversion of X-ray energy into more easily detectable visible light. For such experiments, we used Hama-

matsu J6677 or J6677-01 scintillator packages (Table 2.3) depending on the emphasis of yield or resolution, respectively.

For spatial measurements of high energy photons ($> 100\ keV$), a pixelated scintillator array manufactured by Hilger Crystals was used. The array consisted of $1 \times 1 \times 50$ mm^3 blocks or "voxels" of bismuth germanate oxide (BGO) to absorb as many of the high-energy photons as possible. The voxels were separated by a 100 μm coating of titanium dioxide (TiO_2) to isolate different channels. This array was specifically design to be coupled to the Andor iKon-L HF camera described in Section 2.6.3.

For the activation diagnostic in Section 4.2.2, a matched pair of NaI scintillators of $Ø75mm \times 75mm$ size were used to measure 511 keV photons from β^+ decays. The high-Z iodine helps increase the total photon absorption in the scintillator, and reduces scattered photons from leaving the volume. To measure the 511 keV photons in coincidence, special nuclear electronics are required. A timing single-channel-analyzer (timing SCA) takes the readout signal and gates it spectrally for the desired energy range, before outputing a logic pulse after the signal's peak. These logic pulses are fed into a coincidence unit which acts as a hardware "AND" function, outputing a logic pulse if the inputs fall within a certain time range (usually $> 100\ ns$). These output logic pulses can be summed in an analog or digital counter, depending on the application.

Plastic scintillators (Eljen Technologies, EJ-200) were used for general, pulsed radiation diagnostics around the interaction chamber. These $Ø25mm \times 100mm$ scintillators were placed in three locations: on-axis with the drive laser, behind the electron spectrometer beam dump, and opposite of the beam dump. The relative X-ray signal amongst the different scintillators was strongly correlated with LWFA electron beam generation and allowed initial diagnosis when the electron beam was not optimized.

For the NaI or plastic scintillators, photomultipler tubes (PMT) were coupled to the scintillators for readout to a fast oscilloscope. A PMT works on the principle of

cascaded electron multiplication in a vacuum tube, resulting in a high gain and low noise readout from light entering the photocathode.

2.6.2 Imaging Plates

Photo-stimulatable phosphors, colloquially known as imaging plates (IP), are a form of delayed scintillator (commonly used in medical X-ray detectors) based on the principle of photostimulated luminescence (PSL). IPs contain an active layer of barium fluorohalide phosphor crystals (BaF(Br,I):Eu^{2+}) which can be excited by ionizing radiation. This excitation relaxes to a meta-stable state in Eu^{2+} sites, which can be externally photo-stimulated (in this case with a HeNe laser emitting 632.8 nm light) to re-emit a photon of higher energy ($\sim$ 400 nm). These photons are collected with a photomultipler tube (PMT) to maximize the sensitivity and dynamic range of the detector. After being readout, the IP can be "erased" by exposing it to white light which de-excites any remaining Eu^{2+} sites. However, this also means that the IP must be protected (typically with Al foil) from external light before being read out.

IPs are preferred to X-ray film for a number of reasons: more linearity, larger dynamic range, simple readout, and re-usability [43]. They can be easily placed around the interaction, requiring nothing more than a light-tight wrapping. They are also much more sensitive than scintillator screens and have been absolutely calibrated for practically every form and energy of radiation [44]. However, the primary drawback for high-repetition rate experiments is the need to remove and read-out the plate for every exposure.

There are three main variety of Fujifilm brand IPs used in our laser-plasma experiments: MS (more sensitivity), SR (super resolution), TR (tritium detection). The MS variety was typically employed for these experiments, as the 100 μm resolution and high sensitivity is sufficient for most purposes. The SR and TR offer higher reso-

lution (50 μm) but less sensitivity due to their thinner active layer [45]. Additionally, the TR has no protective plastic coating which allows for the detection of ions and $> keV$ photons, but this means that it is highly hygroscopic (retains water) and must be handled with care to avoid degrading the phosphor. For experiments on HERCULES and ASTRA-GEMINI, Fujifilm-BAS 1800-II and Fujifilm-FLA-5000 readers were used, respectively.

The direct readout from the IP reader is in units of quantum levels (QL). This needs to be converted into linear units of PSL before analysis can be easily performed. The relationship is given by:

$$PSL = \left(\frac{R}{100}\right)^2 \times 10^{5(\frac{QL}{G}-\frac{1}{2})} \tag{2.7}$$

where R is the typical scanning resolution (in μm) and G is the graduation scale. These are set by the scanning parameters where typically $R = 100$ μm resolution and $G = 65536$ (16-bit digitization) are used.

Despite the high sensitivity and dynamic range of IP, there are some cases where the IP can be overexposed for immediate direct readout. This can be solved in a few ways. Since the excited states in the Eu^{2+} decay over time (fast mode ~ 20 min, slow mode ~ 12 $hours$), the plate can be allowed to decay over time to reduce the signal, although this method is slow and inefficient for determining the actual signal exposed. One other method involves the decay caused by active readout since the HeNe laser used to read the signal de-excites the Eu^{2+} at a constant rate. This method is useful for signal just above saturation of the readout, but can become tedious for highly saturated IPs. Another method involves the use of a thin neutral density filter placed on top of the image plate. This attenuates not only the HeNe light incident on the IP and but also the de-excitation light emitted from the IP. For an OD-1 neutral density filter, this allows IPs with roughly a factor of 100$\times$ more signal to be read easily.

Manufacturer	**Andor**	**Andor**	**Princeton Instr.**
Model	**iKon-M SO**	**iKon-L HF**	**PIXIS XF**
Peak QE	95%	95 %	12%
Pixel Array	1024 × 1024	2048 × 2048	1392 × 1040
Pixel Size	13 × 13 μm^2	13.5 × 13.5 μm^2	20 × 20 μm^2
Light Collection	Direct detection	Fiber-coupled	Fiber-coupled
CCD Format	Deep-depletion	Back-illuminated	Front-illuminated
Fiber Diameter	n/a	6 μm	10 μm
Dynamic Range	16-bit	16-bit	16-bit
Readout Noise	± 2.9 e^-	± 4.9 e^-	± 10 e^-
Connector	USB	USB	PCI Frame Grabber

Table 2.4: Specifications of X-ray cameras used in experiments.

2.6.3 X-Ray CCDs

Although charge-coupled device (CCD) cameras are typically used to image optical light, the same principle can be applied to X-rays. As X-rays are absorbed into the active pixel substrate medium, electrons are freed in a similar manner to optical light absorption. The key difference is that X-rays have roughly 1000× more energy than optical photons, so that one X-ray photon can create a much larger amount of signal in the pixel. Figure 2.13 shows a comparison of different CCD sensor geometries. Front-illuminated sensors (Figure 2.13(left)) require light to propagate throught the pixel readout gates and insulation layers, reducing the overall efficiency. Back-illuminated sensors (Figure 2.13(middle)) are made with thinned substrates which can absorb more incident light if illumated on the substrate from the rear. Deep-depletion sensors (Figure 2.13(right)) have a thicker substrate, allowing for higher energy photons to get absorbed in a back-illuminated geometry.

An Andor iKon-M SO camera was used for betatron imaging (not included in this thesis) due to its direct detection, back-illuminated, deep-depletion sensor. This allowed for efficient imaging of photons from 5-20 keV.

The Andor iKon-L HF camera was used for the majority of high-energy detection

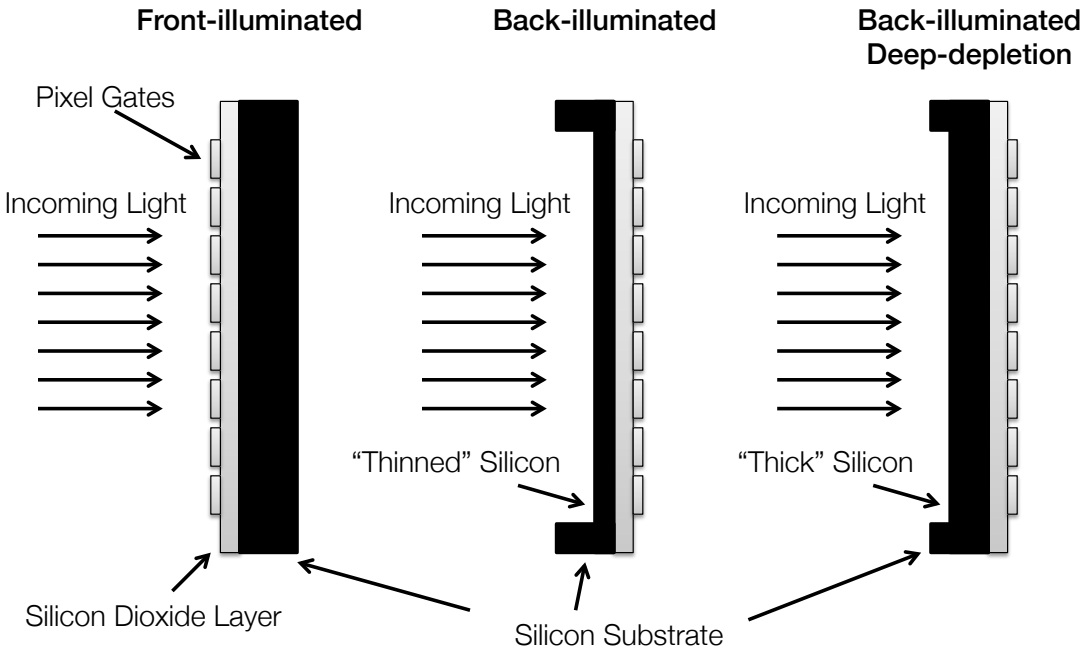

Figure 2.13: Comparison of different types of CCD sensor geometries.

(Chapter IV) due to its fiber-coupled, back-illuminated sensor which could be fitted with various scintillators (Section 2.6.1. Since the scintillators emit light between 400-550 nm, the sensor did not need to be thick (for deep-depletion) to efficiently absorb the scintillator signal. With the Hamamatsu FOP scintillators, photons from 20-100 keV were efficiently imaged. In conjunction with the Hilger pixelated BGO scintillator, photons up to 10 MeV could be coarsely imaged.

For both Andor cameras to achieve 16-bit resolution with low readout noise, the sensors were thermo-electrically cooled to -35° C or lower.

2.6.4 Gamma Spectroscopy

Due to the poor resolution of scintillators, semiconductor detectors were employed to get high-accuracy γ-ray spectra from activation and photo-fission products. Specifically, high-purity germanium detectors (HPGe) were used for γ-ray spectroscopy of the activated products. The liquid nitrogen cooled ORTEC GAMMX Ge(Li) detec-

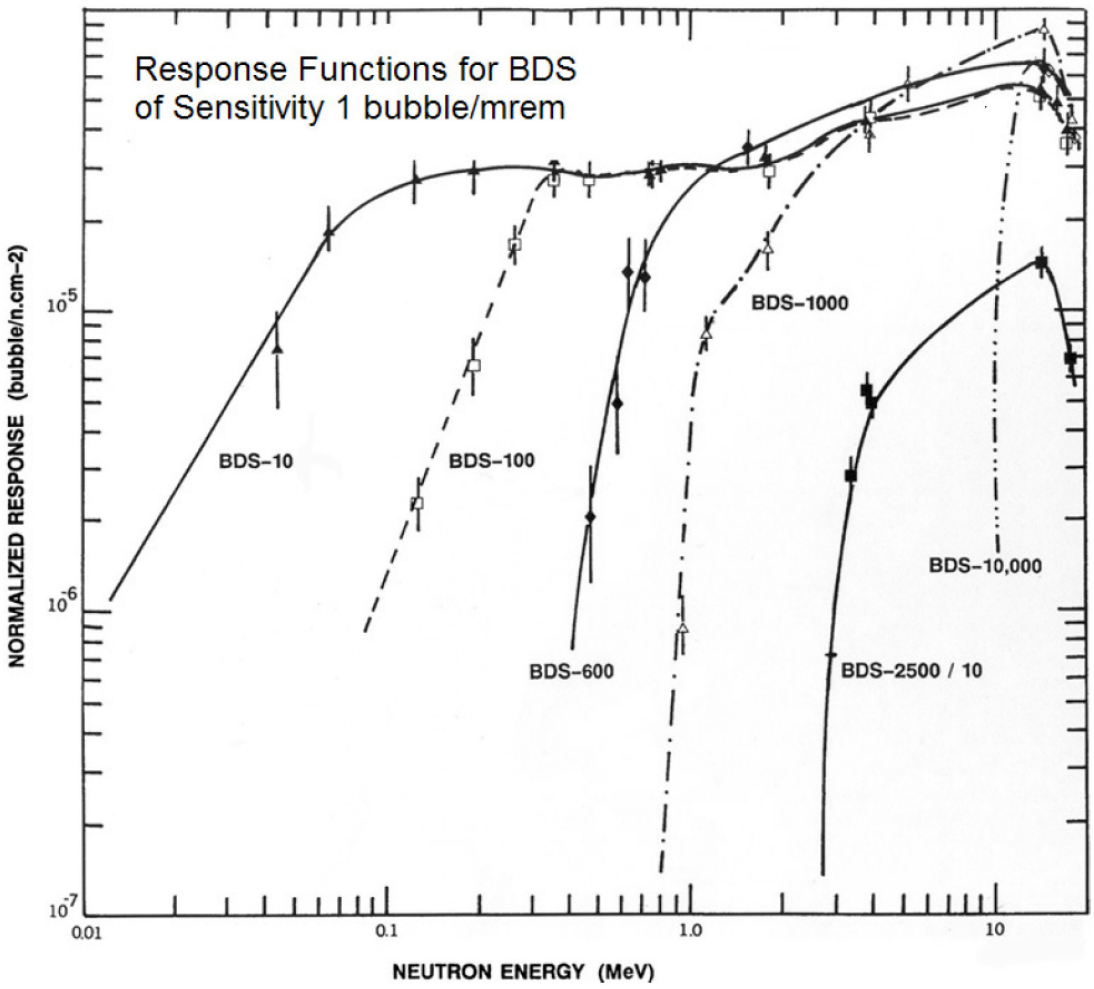

Figure 2.14: Sensitivity of energy-threshold bubble detectors used at ASTRA-GEMINI. Note that the BDS-2500 response is divided by an order of magnitude to fit on the chart. Reproduced from the BDS Series Manual.

tor was used for the photofission measurements. The signal was read by a ORTEC multi-channel analyzer (MCA), which digitized the data for analysis on a computer.

2.6.5 Neutron Detection

Since neutrons are uncharged, they interact weakly with most matter. As such, they are difficult to detect directly and generate very little scintillation light compared to charged particles and photons. This becomes an issue as these other, more easily detected forms of radiation are generated in conjunction with the neutrons.

One solution is to use low-Z (plastic) scintillators to perform time-of-flight (TOF) measurements [46].

Another method of neutron detection uses the principle of historical bubble chambers to create visible "bubble" tracks in a superheated emulsion when a neutron is absorbed. Using chlorofluorocarbon gels, this"bubble detector" can be formed into various shapes and will retain the bubbles until the emulsion is re-compressed. By changing the emulsion mixture and, consequently, the critical point, the low energy threshold can be tailored for different spectral sentivities. Figure 2.14 shows the response of the energy sensitive bubble detectors used on the ASTRA-GEMINI experiments with six different energy thresholds: 10, 100, 600, 1000, 2500, and 10000 keV. Since the higher energy spectral response is similar between the different bubble detectors, the neutron spectrum can be calculated by subtracting the high-energy signal from the low energy bins to find, assuming the neutron flux is consistent across the various bubble detectors. This spectral deconvolution or "unfolding" can be performed easily with a simple spreadsheet, knowing the calibration constants for each bubble detector.

2.7 Computational Modeling

Due to the complexity of interactions studied by the aforementioned experimental diagnostics, the use of computer simulations can deepen the understanding of the underlying physics which may be difficult to study independently. This section will detail some of the computational methods employed for understanding results in this thesis.

2.7.1 Particle-in-Cell Simulations

Particle-in-Cell (PIC) methods are useful for studying collective effects in non-fluid-like plasmas, such as in the process of LWFA and laser-solid interactions. PIC

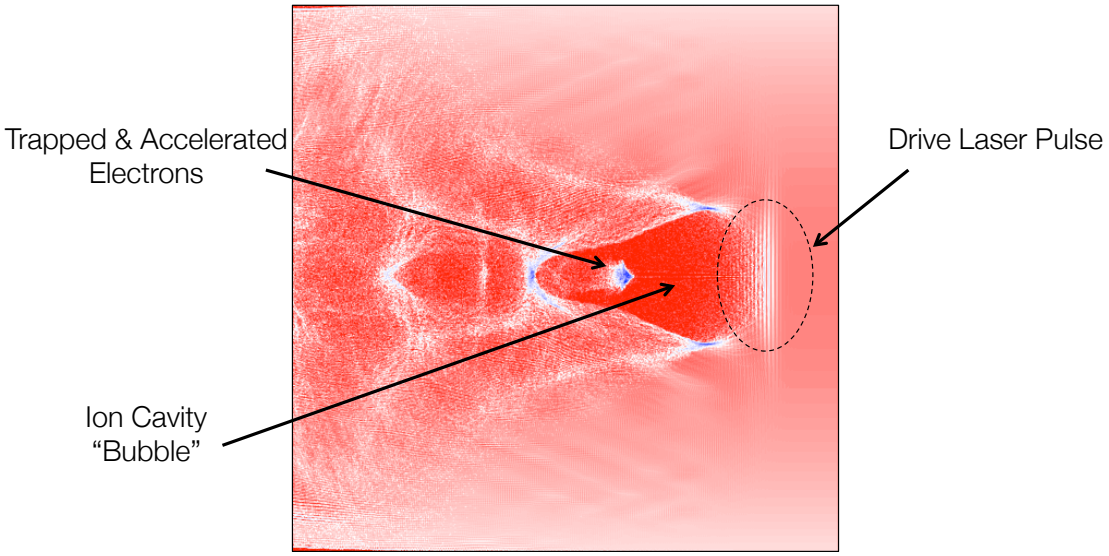

Figure 2.15: Particle density snapshot of a 2D PIC simulation with $a_0 = 5$ laser pulse interacting with a plasma channel with $n_e \simeq 8 \times 10^{18}\ cm^{-3}$ on axis, showing the typical structures of a LWFA.

simulations work by using finite difference methods to move "macro" or "quasi" particles on a grid according to equations of motion. The macroparticles and gridding greatly increase the speed of the plasma simulation since the number of Coulomb interactions required is reduced from the full N^2 down to N.

The process begins by distributing particles to a grid. A electromagnetic field distribution can be interpolated from the particle distribution and assigned back the grid. The particles are then pushed by the field to a new position. The cycle then can repeated, provided the radiation wavelength, Debye length, and the Courant-Friedrichs-Lewy condition ($\Delta x \geq c\Delta t$) are properly resolved to avoid developing spatial, thermal, or temporal instabilities, respectively. The OSIRIS [47] code was used for all PIC simulations used in this thesis, most of which were run on the Nyx cluster at the Center for Advanced Computing (CAC) in the University of Michigan.

PIC simulations of laser-solid interactions were crucial for understanding the field shape and magnitude for the electron radiography experiments (Chapter III) and

are shown in Section 3.4. These simulations required a solid density plasma with a exponential decreasing density of pre-plasma on either side. The density scalelengths were estimated from techniques described in Section 2.7.4. As the laser pulse reflects off the overdense plasma, the simulation boundary conditions were set to be absorbing.

A typical PIC simulation of the LWFA is shown in Figure 2.15. Since the laser readily propagates through the underdense plasma and is of primary interest, a moving frame simulation is used to track the laser pulse and consequent plasma evolution, also greatly reducing the computational time due to the smaller number of particles and grid size.

2.7.2 Monte-Carlo Simulations

Monte-Carlo methods are a type of computer algorithm that employ random sampling to quickly converge on a numerical solution. These techniques were first developed during the Manhattan Project for studying radiation transport in nuclear weapons. However, these can be used for a wide range of stochastic (non-deterministic) problems such as calculation of bremsstrahlung spectra and beam fluctuation analysis.

To support the bremsstrahlung results (Chapter IV), Monte-Carlo simulations using the FLUKA [48] and MCNP codes were performed to simulate the radiation transport and conversion of electron beams into bremsstrahlung and secondary particles. Due to its focus on nuclear fission processes and limited cross-section libraries for high-energy positrons, MCNP5 was primarily used for simulating photon spectra/divergence and ^{238}U photofission yield (MCNPX has a more extensive library of particles and cross-sections, but requires a different source and input; MCNP5 and MCNPX will soon be merged into MCNP6, remedying this issue). Thus, the high-energy physics FLUKA code was used to simulate situations where positrons (and pions) were of primary interest, such as the Compton scattering spectrometer (Section 4.2.2) and

positron measurements (Section 4.3).

Both codes start with an input deck of particle energies and directions. The particles propagate a random distance (normalized to the mean-free path) before undergoing a randomized process (scattering, absorption, pair production, etc.) according to the relative cross-sections. The particle continues along its "random walk" until it leaves the simulation or gets absorbed. The radiation created along the path is likewise propagated until it terminates. The process is repeated with the next test particle. The desired simulated quantity (particle type, spectra, divergence, etc.) is then tallied. Over the course of the numerous (typically 10^6) particle runs, statistically significant processes can be observed.

To better understand the difficulty of beam-particle overlap for NLTS, a proprietary Monte-Carlo algorithm to simulate pointing fluctations and their effects was developed by Martin Farlotti and the author (Section 5.3). This code normally distributed the electron and laser beams separately on a 2-D grid before calculating the backscattered photon distribution from the interaction of the beams. A parameter scan of temporal and spatial offsets, divergences, and perturbation amplitudes was performed and is detailed in Section 5.3.

2.7.3 Particle Tracking

To study single particle motion in a static, deterministic system, simple algorithms using the Lorentz force equation can be implemented to calculate the particle trajectory. Various codes were used for mapping electron trajectories in the following scenarios relevant to this thesis: electron deflection in magnetic spectrometers, injected electron motion inside the wakefield bubble, and beam deflection after probing magnetic fields on solid targets.

Proprietary codes written in MATLAB and Microsoft Excel as well as simulations using the COMSOL Particle Tracing package were used to calculate electron trajectories

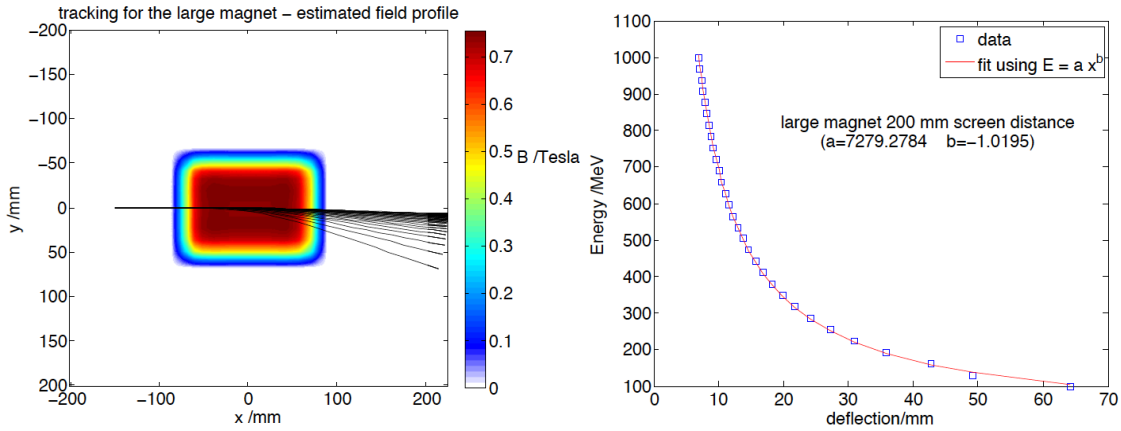

Figure 2.16: Trajectories (left) and overall deflection on the scintillator (right) of electrons with different energies entering the spectrometer magnet used in HERCULES experiments. Courtesy of Stefan Kneip.

in the electron spectrometer. These required the experimental geometry and magnetic field parameters to calculate the deflection as a function of electron energy. Example particle trajectories are shown in the left of Figure 2.16 and the resultant spectral correspondence on the scintillator screen is shown on the right of Figure 2.16.

For understanding results in Chapter III, a 2D particle tracking code written by Calvin Zulick was employed to study electron beam propagation through strong electromagnetic fields. This code used an electron beam spectrum/profile, a test magnetic field profile, and the experimental geometry as inputs and produced an output electron beam profile, as shown in Figure 3.12.

2.7.4 Fluid Simulations

Although the work in this thesis typically occurs on fs timescales which mostly ignore the "slow" ($> ns$) fluid dynamics, the target dynamics before the laser pulse arrives are extremely important for how these fs processes evolve.

For solid target interactions, 1D radiation hydrodynamic simulations were performed using HYADES [49] to study the effects of ns contrast on the pre-plasma scale-

length of solid target interactions. These simulations were run with a ramped laser pulse based on measurements from Section 2.3.2 interacting with a step function target with solid density surrounded by vacuum. As a function of the laser temporal intensity distibution, an exponential density distribution of pre-plasma can form from the material ablated off the target [50]. This exponential scale-length is critical for understanding of certain laser-plasma applications such as high-harmonic generation (HHG) [51] and will be discussed further in Chapter III.

For gas target dynamics, 2D computational fluid dynamics (CFD) simulations were performed using the COMSOL CFD package [52] to study the gas flow in and around the jets/cells. These simulations were run with a ramped gas pulse based on settings from Sections 2.4.1 and 2.4.2 interacting with the target boundaries surrounded by vacuum. As a function of the backing pressure and geometry, a lineout of the density distribution on the the laser could be taken [39] and consequently fed into PIC simulations (Section 2.7.1) to get more realistic parameters.

CHAPTER III

Electron Radiography of Laser-Solid Interactions

3.1 Introduction

Laser-solid interactions have been studied since the creation of the first laser in 1960. Understanding the dynamics of such interactions have been key to the development of numerous laser applications. At high laser powers/intensities, the prominent applications of laser-solid interations include inertial confinement fusion (ICF) [53], laser-based ion acceleration, and high-order harmonic generation (HHG) [51].

Strong magnetic fields are well known to be generated by a variety of mechanisms in laser interactions at a solid density plasma-vacuum interface, including the important Biermann battery effect [54]:

$$\frac{\partial \mathbf{B}}{\partial t} = -\frac{k_B}{e n_e}(\nabla n \times \nabla T) \tag{3.1}$$

In such interactions, the laser field generates hot electrons which can circulate through the target and spread along the target surfaces (front and rear), generating an electromagnetic sheath field that expands from the laser focus [55, 56, 57, 58]. Furthermore, complex magnetic fields may arise by filamentation of the expanding current sheet [59]. Measurements of such fields have previously been performed using laser-generated proton radiography [60, 61, 62, 63, 64, 65], including time resolved mea-

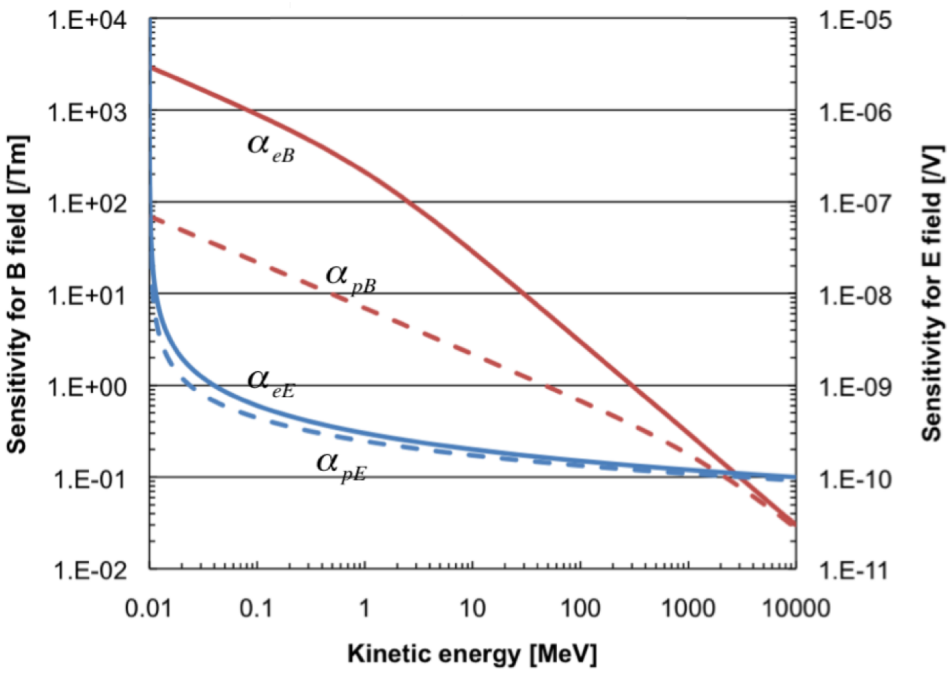

Figure 3.1: Sensitivity of protons (dashed) and electrons (solid) for electric (blue) and magnetic (red) fields. Note that the (time-independent) magnetic field sensitivity of 10 MeV protons from TNSA is similiar to 100 MeV electrons from LWFA.

surements of magnetic fields advecting with plasma flows [66, 67, 68]. Current laser driven sources of protons [69, 70, 71, 72] are usually produced by target normal sheath acceleration (TNSA) and are non-relativistic, thereby limiting temporal resolution. In contrast, highly relativistic electron bunches (>100 MeV) generated by laser wake-field acceleration (LWFA) typically have durations less than the driving laser pulse (<30 fs) [73, 15] and can be optically synchronized, therefore enabling the observation of faster dynamics in field structures than can be easily performed with TNSA. A comparison of sensitivities between protons and electrons to electric/magnetic fields is shown in Figure 3.1.

In the interaction of an oblique incidence relativistic intensity laser pulse ($a_0 \gg 1$), the particles are heated primarily by a combination of resonance absorption [74] and Brunel absorption [75] to produce relativistic electrons. These electrons propagate

throughout the target and into the vacuum, forming expanding sheath fields on the front and rear surfaces. For metal or plasma targets, the net current within the target volume will be approximately zero [76], but fast electrons will be free to propagate in the vacuum near the surface, balanced by a return current just inside the bulk material. This leads to a thin Debye sheath with an electric field perpendicular to the surface and an inductively generated azimuthal magnetic field, both expanding radially at close to the speed of light.

In this Chapter, we demonstrate proof-of-principle radiography of electromagnetic fields relativistically expanding from the interaction of intense laser pulses with planar, foil targets, using LWFA electron beams.

3.2 Experimental Setup

For these experiments, the HERCULES laser was operated at 100 TW with native 10^8 contrast ratio between the main pulse and the amplified spontaneous emission (ASE) on the nanosecond pulse pedestal and 10^4 contrast ratio for the picosecond pulse pedestal. The cross-polarized wave (XPW) pulse cleaning technique could be enabled for contrast improvement, yielding up to 10^{11} contrast ratio for the ASE [33]. The experimental and optical geometries are shown in Figures 3.2 and 3.3, respectively. A pick-off mirror sent the central portion of the beam to an $f/18$ off-axis paraboloid (OAP) mirror focusing the pulse to an intensity of 1.6×10^{19} W/cm^2 ($a_0 = 2.8$) into a He-N_2 (95:5 mass ratio) plasma of 2×10^{19} cm^{-3} peak density above a 1.3 mm supersonic gas jet nozzle, generating a broad energy spectrum electron beam with up to 120 MeV energy and 100 pC charge via ionization injection [77, 78]. The remaining annular beam was sent to a delay stage with 300 ps of adjustable delay and was then focused with an $f/3$ OAP mirror to an intensity of 4×10^{19} W/cm^2 ($a_0 = 4.4$) onto a solid target at 30° incidence. The $f/3$ focus was spatially overlapped on the $f/18$ beam axis 10 cm behind the $f/18$ focus. Timing overlap was achieved

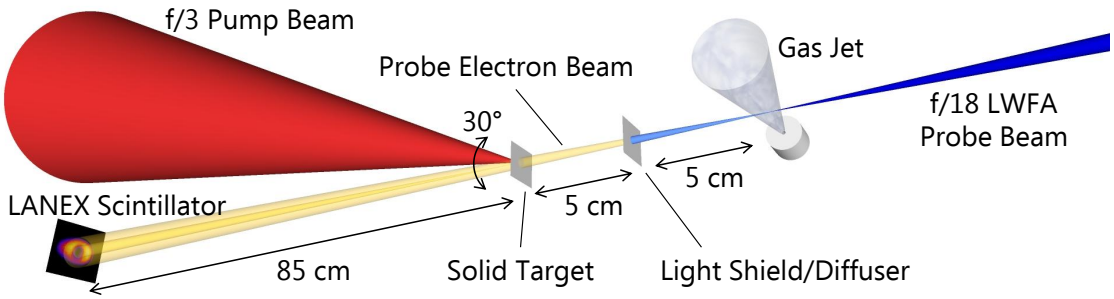

Figure 3.2: Simplified experimental geometry for electron radiography.

using the $f/18$ beam to backlight the breakdown in air at the $f/3$ focus, yielding an optical timing accuracy of $\pm 30\ fs$ between the two beam paths.

Since the electron beam exits the gas jet plume with a relatively narrow, but elliptical, divergence ($<$10 $mrad$) and a large energy spread ($\Delta E/E \sim 100\%$), a 75 μm thick aluminum foil was placed 5 cm behind the gas jet. This acted both as a shield to block any remaining $f/18$ light from interacting with the rear surface of the solid target as well as a diffuser to allow the electron beam to radiograph a larger area of the target while scattering away the low energy ($<$15 MeV) electrons as [79]:

$$\theta_{scatter} \propto \frac{1}{E_{e^-}} \tag{3.2}$$

After the electron beam probed the solid target, the electron beam profile was measured 85 cm away from the target by a LANEX scintillator screen at 45° to the beam imaged with a CCD camera at 90° to the beam to minimize distortion. After passing through the diffuser and target, the electron beam had a Gaussian profile elliptical about the polarization axis with a divergence of $\sim$ 20 $mrad \times 30\ mrad$ FWHM. Because an accurate electron spectrometer could not be placed behind the solid target, diffuser, and LANEX screen, a charge-calibrated spectrometer with a 0.8 T magnet and LANEX screen was installed directly behind the gas jet and was used to characterize the electron beam energies in a separate shot series. A typical

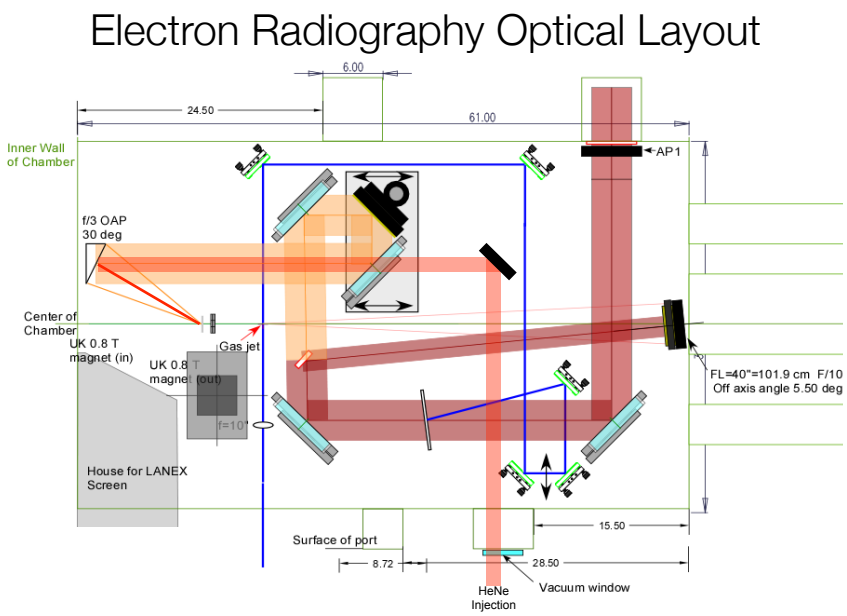

Figure 3.3: Optical layout of the electron radiography experiment.

electron spectrum is shown in Figure 3.4.

The focal position on the solid target was found by optimizing the X-ray signal with a shielded plastic scintillator coupled to a PMT over a number of shots while blocking the $f/18$ beam. Next, the $f/3$ beam was blocked and the electron beam was checked for pointing and charge stability both with and without the diffuser. After optimizing the solid target focus and electron beam, both beams were unblocked and a series of shots were taken while varying the relative time delay of the $f/3$ beam with respect to the $f/18$ beam. The solid target and diffuser were refreshed after each shot and aligned to the optimum focal position. A variety of solid target thicknesses ($10-200\ \mu m$) and materials (Al, Cu, Au, and Mylar ($C_{10}H_8O_4$)) were investigated for this experiment, although thin ($10-13\ \mu m$) targets were primarily used to minimize scattering.

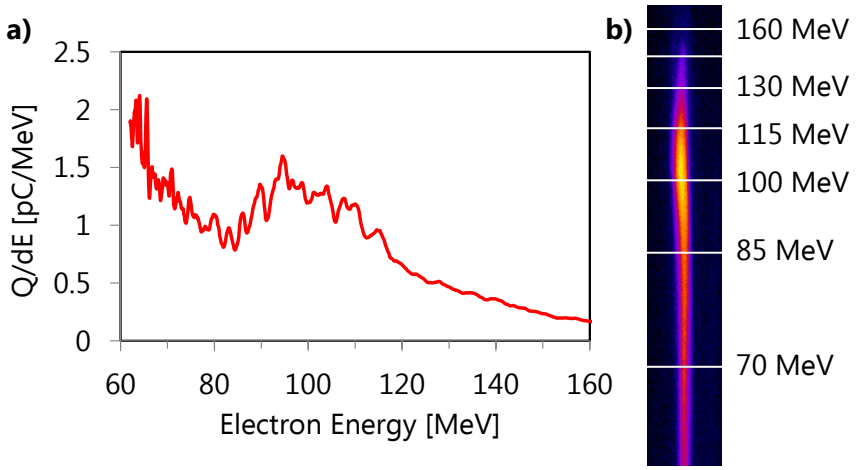

Figure 3.4: (a) Calibrated electron spectrum and (b) spectrometer image for a typical probe electron beam.

3.3 Experimental Results

When the $f/3$ was incident on the target, distinct features were observable, depending on the relative timing $\Delta\tau$, laser contrast level, and the target material. Such features included a focused region of electrons, an area depleted of electrons or a ring structure, and asymmetric structures. Differences in observed features can be explained by the underlying dynamics of the laser-target interaction since laser contrast and target type (metal vs. dielectric) greatly affect the scale length of the pre-plasma and absorption of laser energy. For low contrast shots (10^8) with dielectric Mylar targets, focused structures (Figure 3.5) were consistently observed out to 7.5 ps, indicating that the front surface fields dominated the interaction. For low contrast shots with metallic aluminum targets (Figure 3.6) both focusing and de-focusing could be observed, with focused features appearing for earlier times before de-focusing holes in the electron beam profile appeared at longer timescales (>1.5 ps). This indicated that the front surface field dominated early in time before either: (a) the beam over-focused and creating a de-focusing feature, or (b) the rear surface became dominant at longer time scales. Since the material composition (metallic versus dielectric) and

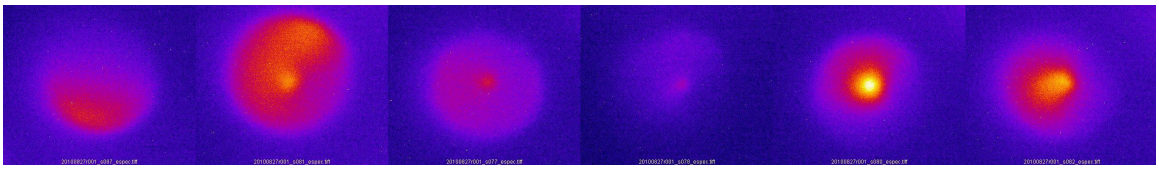

Figure 3.5: Radiographs of low-contrast shots taken on 13 μm Mylar foil. Note the constant focusing structure over time.

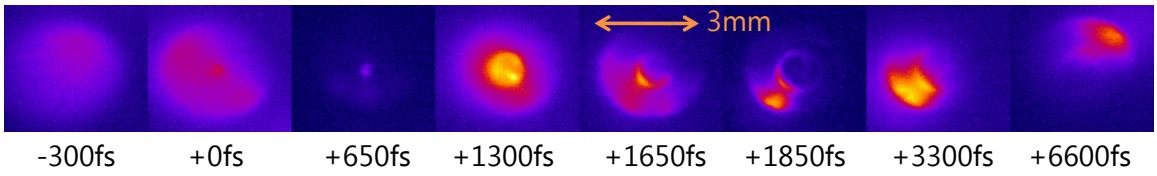

Figure 3.6: Radiographs of low-contrast shots taken on 10 μm Al foil. Note the focusing structure early transitioning to defocusing later in time.

laser contrast ratio affect the amount of pre-plasma formed, we decided to re-attempt the 10 μm aluminum experiment with XPW, which improved the laser contrast to 10^{11} from 10^{8}. With high contrast shots on 10 μm aluminum, the observed feature was a hole in the electron beam expanding linearly in time (Figure 3.7) out to 1.5 ps after an initial period of focusing.

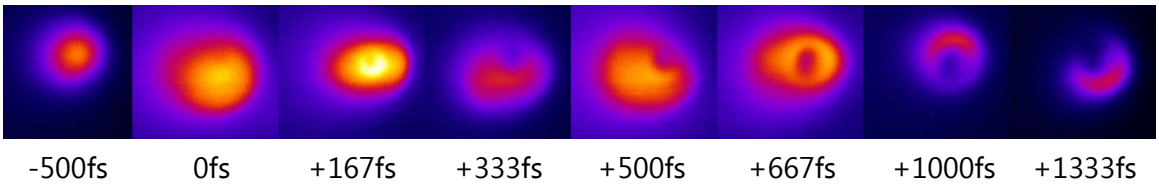

Figure 3.7: Radiographs of high-contrast (XPW) shots taken on 10 μm Al foil. Note the defocusing structure rapidly growing in time.

3.3.1 High-Contrast Interactions

To quantify the size of the high contrast deflection feature while compensating for the irregular probe pointing overlap, the average of four lineouts were taken across the center of deflection region in slices rotated at 45° intervals. For each lineout, the mid-point from the top peak to lowest point of the valley was used to calculate the threshold for the curvature of the feature. A circle was then fit to the feature at this threshold level to find its diameter on the scintillator. Dividing this by the projection magnification (18× in our case, taking the diffuser as the effective source), the diameter of the feature on the target can then be calculated. Figure 3.8(d) shows the size of this feature as a function of pulse delay, indicating that the speed of the expansion of the field structure is $(0.98 \pm 0.08)c$. An example lineout for a high contrast shot is shown in Figure 3.8(b).

For a radially symmetric azimuthal magnetic field, the probe electron beam will either experience a momentum dependent defocusing or focusing effect, whereas a focusing/defocusing electric field would be radially directed. Since the strongest electric field component is expected to be normal to the target surface and therefore parallel to the electron beam direction, the inductive magnetic field associated with the expanding electric sheath [58] is likely to be the origin of these features. The front surface sheath (facing towards the incident $f/3$ pulse) will generate a magnetic field oriented to focus the probe electron beam, whereas the rear surface sheath (facing towards the probe electron beam) will generate a defocusing magnetic field structure.

3.4 Simulations & Analysis

To simulate the laser-solid interaction and magnetic field generation, 2D particle-in-cell simulations were run using the OSIRIS 2.0 framework [47]. The charge density profile was constructed piecewise from a rectangle function with exponential ramps

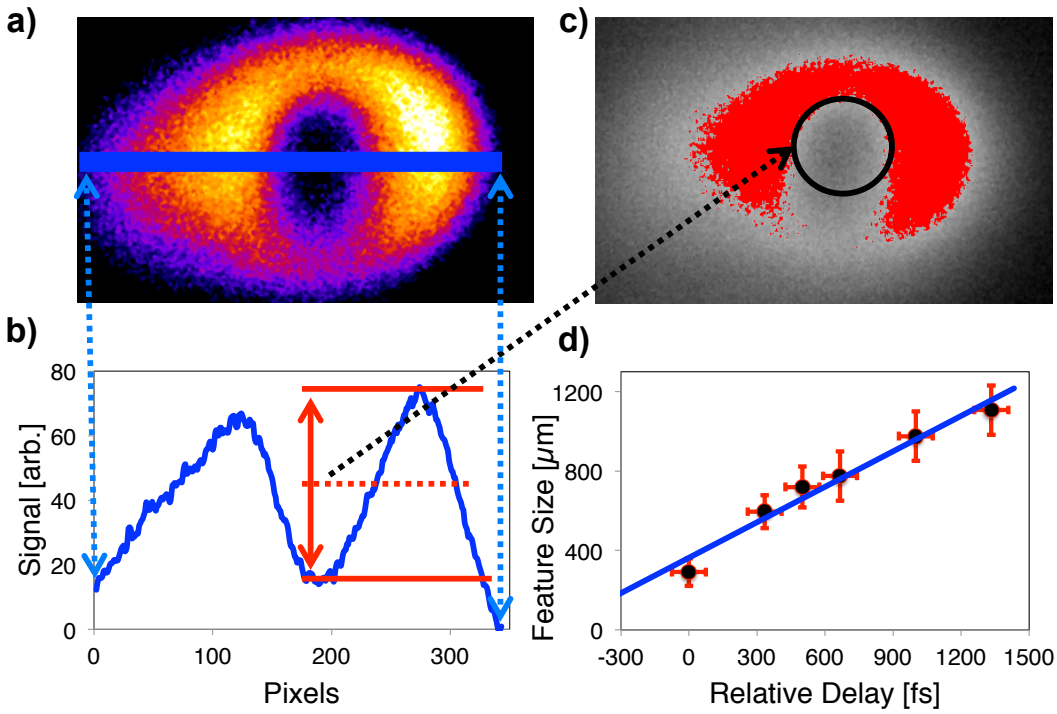

Figure 3.8: (a) Radiograph from Figure 3.7 with location of lineout. (b) Lineout plot with mid-point between peak-to-valley indicated. (c) Radiograph with threshold set to mid-point and a circle fit to curvature to determine feature diameter. (d) Plot of measured feature size versus delay timing taken from analysis of Figure 3.12(a). The error bars represent the variance in determining the diameter over multiple lineouts as well as the timing uncertainty. The linear fit (solid line) indicates that the velocity of the expanding feature is $(0.98 \pm 0.08)c$.

on the front and rear surfaces. The peak density ρ_0 was taken as $\rho_0 = 100n_c$, where n_c is the critical density, the target thickness was $L = 60c/\omega_0$ and the exponential scalelength was $\lambda_{pp} = 6c/\omega_0$. The target was at a 30° angle with respect to the simulation box. A Gaussian laser pulse with $a_0 = 6$ was launched in the x_1 direction, linearly polarized in the x_2 direction with a waist of $w_0 = 40c/\omega_0$ and a 5th order polynomial temporal shape with a duration of $\omega_0 t_0 = 80$.

Two particle species were used; one with charge to mass ratio $q/m = -|e|/m_e$ initiated with a thermal momentum of $p_{th} = 0.01 m_e c$ and one with $q/m = +|e|/m_p$ initiated at rest, where m_p is the proton mass. 9 particles-per-cell were used with a quadratic interpolation charge weighting scheme. The domain was divided by 10000 grid cells in x_1 by 4000 in x_2, yielding cell sizes $\Delta x_1 = 0.1c/\omega_p$ and $\Delta x_2 = 0.2c/\omega_p$. The simulation was run for $\omega_0 t = 1000$ in steps of $\omega_0 \Delta t = 0.07$. Compensated binomial smoothing was applied to fields and currents on the grid.

The high-contrast simulations indicate that the laser energy is absorbed into a near isotropic population of energetic electrons that propagate through the target and into the vacuum. Within the target volume, background electrons cancel the fast current, but at the interfaces the hot electron density exceeds the background cold electron density. This leads to unneutralized currents in the sheaths at the edges of the targets. A cold return current is drawn from electrons in the higher density region, the net result being oppositely directed currents along the surfaces of the target. The oppositely directed current sheets result in a magnetic field that is approximately a scalelength (λ_{pp}) thickness between them, expanding along the surface at the speed of light (Figure 3.9). The net result is a relativistically expanding Debye sheath.

To simulate low-contrast conditions, a large pre-plasma scalelength ($\lambda_{pp} = 100$ μm) was added to the front of the target. The rear of the target was assumed to be similar to the high-contrast case since there is no laser ablation. The laser was sent normal to the surface since the laser absorption is dominated by the pre-

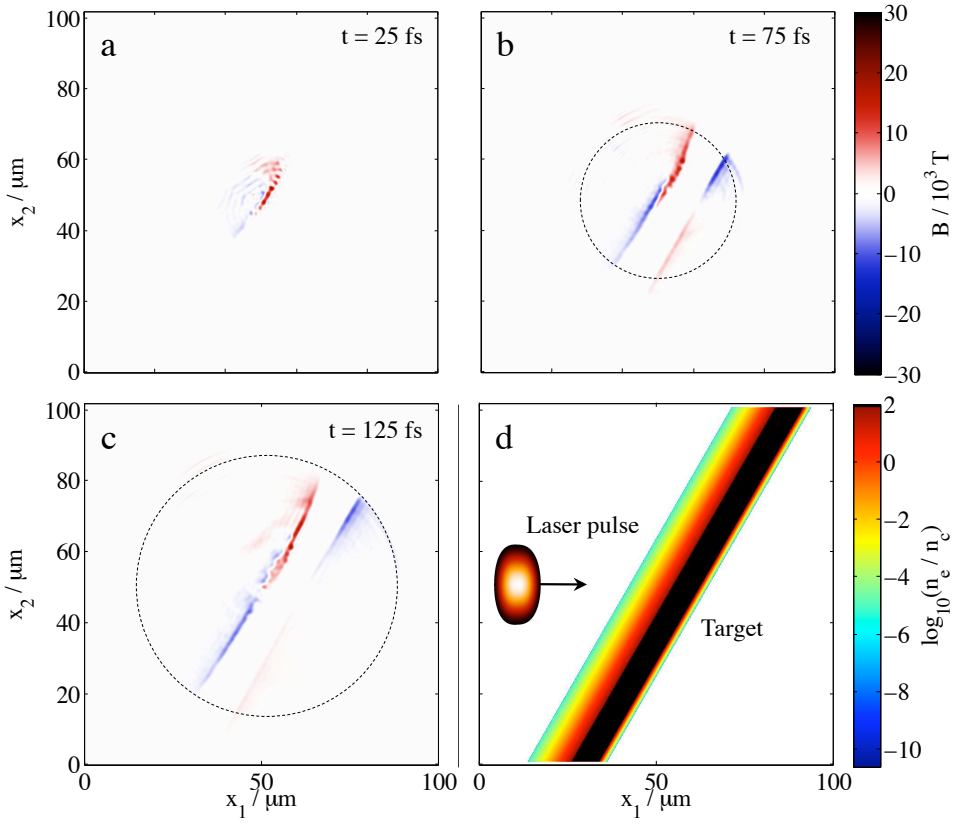

Figure 3.9: (a-c) Magnetic field component in the x_3 direction in Tesla (Fourier filtered to remove the laser field) at different times, where $t = 0$ is when the peak of the pulse is incident on the target surface, and (d) initial electron density profile with initial pulse envelope superimposed.

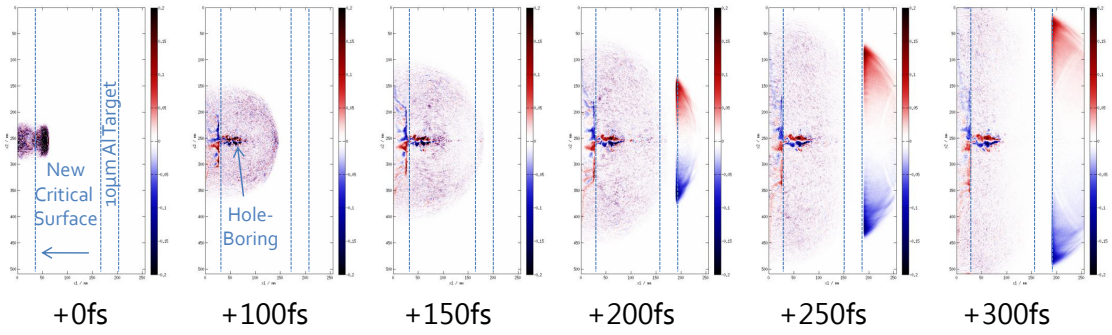

Figure 3.10: Simulations of low-contrast interactions taken on a 10 μm Al target with a 100 μm-scale pre-plasma.

plasma. The simulation indicated that as the laser passed the critical surface of the pre-plasma, it undergoes hole-boring [80] and generates a radially-expanding electron current (Figure 3.10). Due to the amount of pre-plasma, this electron current could not develop a large magnetic field on the front surface as the return current in the plasma cancels it out. This leads to a weak front surface magnetic field early in time, as observed experimentally in Figure 3.6. Once the electron current reached the rear of the target, it begins to spread along the rear surface, creating an expanding field similar to that seen in the high-contrast simulations. This delayed rear field expansion would explain the defocusing observed later in time in Figure 3.6.

In this 2D geometry, the electric field is in the simulation plane, normal to the target, and the magnetic field is normal to the simulation plane. For the relativistic electrons moving in the plane of the simulation, these fields exert forces with comparable strength [81]. Hence, due to the geometry, deflections to a probing electron beam normal to the target, as in the experiment, would be expected to be primarily due to the magnetic field [82]. In addition, an electron traveling from the laser focus along the target surface experiences cancellation of the sheath electric force and Lorentz force due to the magnetic field ($\mathbf{F} = -e\mathbf{E} - e\mathbf{v} \times \mathbf{B} \simeq 0$) and can propagate freely.

For a simple model of the generation mechanism, consider a circular loop at radius r about the $\hat{\mathbf{z}}$ axis, normal to the surface near the laser focus, at a distance z_0 from the surface. Assuming azimuthal symmetry about the focal spot, and negligible displacement current normal to the surface, Ampére-Maxwell in integral form will yield:

$$B_\theta(r, z, t) \simeq \frac{1}{c^2 r} \frac{\partial}{\partial t} \int_0^r E_z(r', z, t) r' dr' \tag{3.3}$$

Extending the surface to become a Gaussian 'pillbox' with the second circular surface at $z = 0$, just outside the solid surface where $E_z \simeq 0$, and assuming E_r is negligible,

Gauss's law and the continuity equation can be combined to relate the azimuthal magnetic field B_θ to the *radial* fast current j_r as:

$$B_\theta(r,z,t) \simeq -\mu_0 \int_z^\infty j_r(r,z',t)dz' \tag{3.4}$$

Hence in the 2D slab geometry of the simulation, j_r (and therefore B_θ) is approximately constant with r until the electrons are slowed to sub-relativistic speeds, whereas in 3D the j_r (B_θ) would be expected to fall off as $1/r$.

For relativistic electrons generated with a number density $n \sim n_c/4$ in a sheath of thickness $L \sim \lambda_0$, the peak magnitude of the magnetic field generated would be:

$$|B| \sim \frac{\mu_0 c|e|n_c\lambda_0}{4} \sim 10^4\,[T] \tag{3.5}$$

Such a field cannot indefinitely grow in radius. The maximum field extent at stagnation r_S can be estimated by equating the integrated electromagnetic field energy (falling off as $1/r$) with laser pulse energy U_p having some absorption fraction f (ignoring other dissipative mechanisms and ion motion). Hence, assuming a field of the form $B = B_0 r_0/r_S$ outside radius r_0, the energy absorbed into hot electrons and transferred to the magnetic field is of the order:

$$fU_p \approx \frac{2\pi r_0^2 \lambda_0 B_0^2}{\mu_0} \ln\left(\frac{r_S}{r_0}\right) \tag{3.6}$$

Therefore, the maximum radius is:

$$r_S \approx r_0 \exp\left(\frac{2fU_p}{\pi^3 m_e c^2 n_c r_0^2 \lambda_0}\right) \tag{3.7}$$

For $U_p = 1$ J, $f = 0.2$ and $r_0 = 5\ \mu m$, this gives $r_S \sim 500\ \mu m$, where the field will have dropped to $B \sim 10^2\ T$.

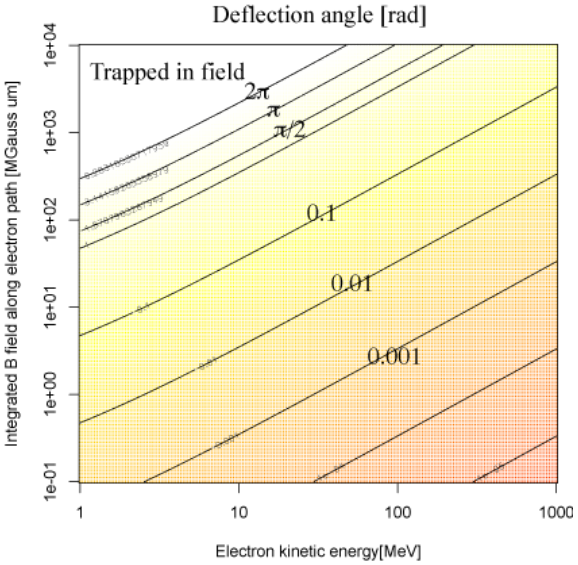

Figure 3.11: Deflection angle of electrons as a function of electron energy and field strength. For angles above 2π, the electron is trapped in a cyclotron orbit in the field.

This is in reasonable agreement with experimental observations as the deflection of electrons at early times is $> 60\ mrad$, which for a 50 MeV electron yields an integrated field strength of $\sim 10^4\ T \cdot \mu m$, as shown in Figure 3.8 and given by:

$$\int_L \mathbf{B} \times \mathrm{d}\ell = \frac{m_e c\,\theta}{e}\sqrt{\left(\frac{m_e c^2 + E_{e^-}}{m_e c^2}\right) + 1} \tag{3.8}$$

Assuming a sheath of thickness of $\sim 1\ \mu m$, this level of deflection infers magnetic field strengths of order $\sim 10^4\ T$ as shown in Figure 3.11.

To understand the observed electron profiles, a second-order, time-centered electromagnetic particle tracking code was employed. Based on experimental parameters, a flat electron spectrum from 20-120 MeV was modeled with 10^5 particles projected 50 mm with a transverse emittance of $\epsilon_\perp = 53\pi\ mm\,mrad$ in a Gaussian distribution. Figures 3.12(b-d) show simulated electron profiles having passed through a 1 μm thick

azimuthal magnetic field structure of the form:

$$B(r,t) = \begin{cases} B_0 & r < r_0 \\ B_0 r_0 / r & r_0 \leq r \leq r_S(t) \\ 0 & r > r_S(t) \end{cases} \tag{3.9}$$

where $r_0 = 5\mu m$, $r_S(t) = ct$, and $B_0 = 3.8 \times 10^4\ T$ (corresponding to the PIC simulation output where $f \sim 0.1$). In Figure 3.12(d), the magnetic field is defocusing and in Figure 3.12(b,c) the magnetic field is focusing. Simulations with both rear and front magnetic fields indicate that they tend to cancel, due to the small scattering angles involved, and hence the resulting deflection of the probe electrons is consistent with a single field corresponding to summation of the front and rear fields.

At early times (small r_S), the electron profile has a void for all magnetic field structures, due to the high field strength causing overfocusing of the electron beam in the focusing cases. For later times (large r_S) as the field strength falls off at the periphery, the difference between focusing and defocusing structures becomes apparent. Although the observed electron profiles in Figure 3.12(a) are reminiscent of the defocusing structure, the 10 μm thickness of the target and the short pulse duration make it very unlikely that the rear sheath is stronger than the front – a conclusion that is also supported by particle-in-cell simulations. In Figure 3.12(b) the focusing case has also been performed with an azimuthal perturbation to the field structure (a sinusoidal perturbation, including a radial component to satisfy $\nabla \cdot \mathbf{B} = 0$). This could arise due to filamentation of the current sheet [59], for example. This asymmetry suppresses the focusing of the probe beam and results in a dip in the profile similar to the defocusing case for the relevant timeframe.

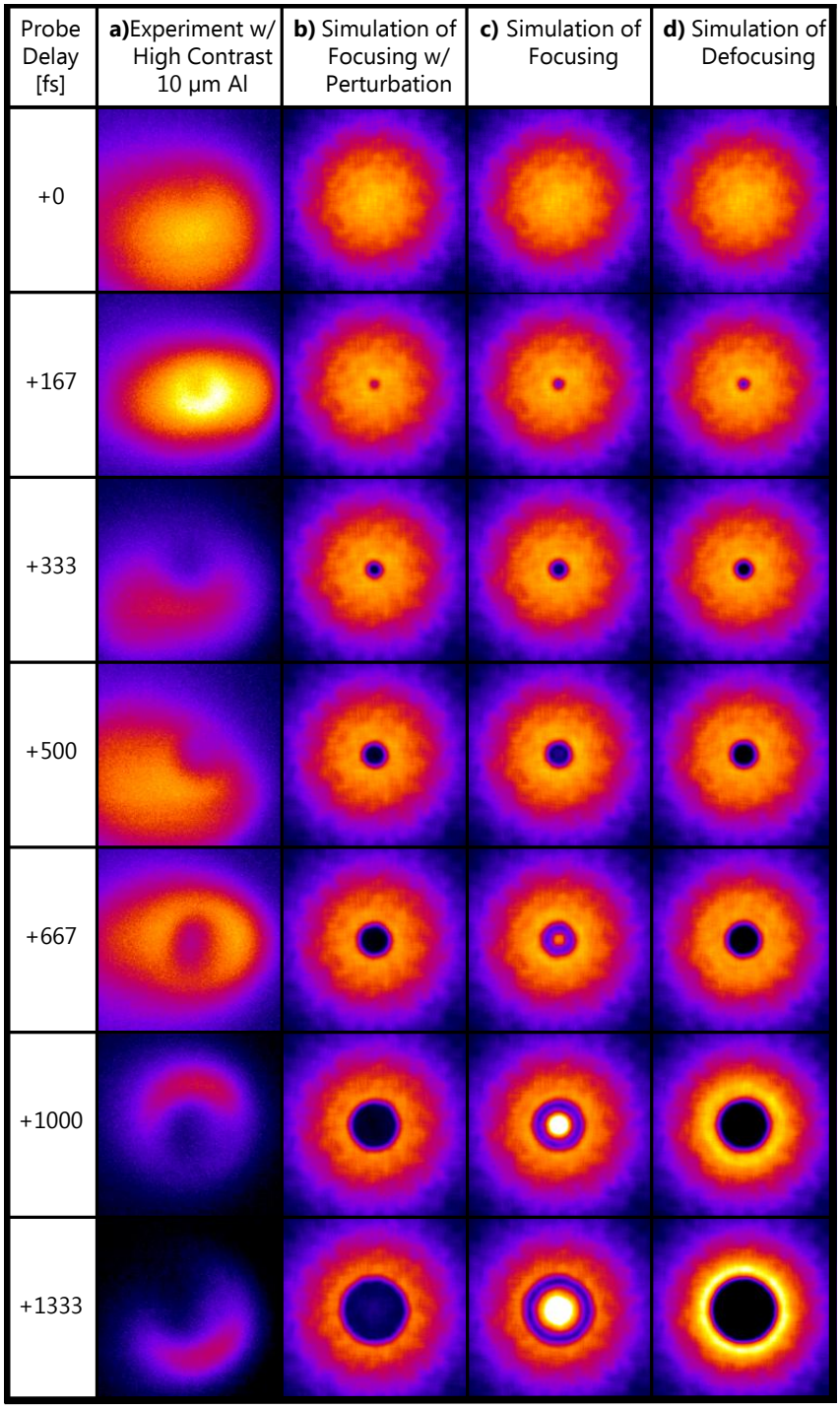

Figure 3.12: (Column a) Measured radiographs taken from laser shots with high contrast and 10 μm Al at delay timings from 0 to +1333 fs. (Columns b-d) Simulated radiographs for each respective delay with defocusing with azimuthal perturbation (b), focusing (c), and defocusing (d). (The color and length scales are the same in each column.) Note that the electron beam profile is elliptical before interacting with the target and the simulated profiles assume radial symmetry for simplicity.

3.5 Conclusions

In conclusion, electron beams from LWFA can be used as an ultrafast probe of rapidly evolving field structures in laser-plasma interactions. These beams have the advantages of being tunable in energy, having ultra-short duration, and being easily synchronized. In these experiments, the electron spectrum was very broad, which led to some loss of spatial resolution. However, significantly more monochromatic electron beams are achievable from LWFA and could be used in future work for more accurate results. In summary, a LWFA electron probe beam was used to measure fs scale relativistically expanding sheath fields in a laser-solid interaction that extend to diameters of $\sim 1\ mm$ and have peak fields of order $\sim 10^4\ T$.

CHAPTER IV

Bremsstrahlung & Secondary Particle Generation

4.1 Introduction

This chapter will focus on the stochastic, higher-energy processes generated by bremsstrahlung, most of which are multi-step. The fundamental, primary step is the creation of high-energy ($> MeV$) bremsstrahlung photons, in this case by the interaction of LWFA electron beams with high Z converter targets.

Depending on the energy of the photon, many different production processes are possible. For $E_{h\nu} \geq 1.022\ MeV$, the creation of $e^- e^+$ pairs becomes feasible. For photons of $5\ MeV < E_{h\nu} < 50\ MeV$, there is also a strong probability of (γ, n) neutron ejection, especially for higher Z targets. Finally, for $E_{h\nu} > 140\ MeV$, there is a small, but finite, probabilty of "exotic" particle production, such as π mesons and $\mu^- \mu^+$ lepton pairs.

4.2 Bremsstrahlung Photons

The interaction of a high-energy electron beam with any material will produce a broad energy spread of photons up to the maximum electron energy via the process of bremsstrahlung [83]. Depending on the input electron beam (energy, divergence) and converter target (Z, geometry) parameters, the generated photons will exhibit

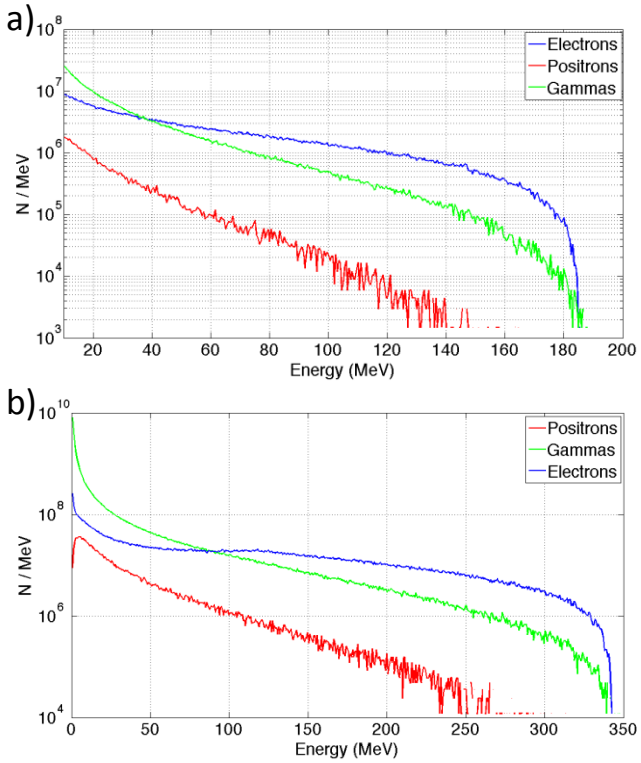

Figure 4.1: Simulated bremsstrahlung spectra from FLUKA for a flat-top spectra electron beam with (a) 60 pC charge up to 200 MeV and (b) 500 pC charge up to 350 MeV interacting with a 2.8 mm Ta converter. Reproduced courtesy of Gianluca Sarri, Queen's University of Belfast.

characteristic distributions with respect to flux, energy, and divergence. For the majority of experiments, higher flux is desired, so the Z is maximized and the thickness is matched to the radiation length of the material so as to minimize reabsorption and scattering of the generated photons.

For an ultra-relativistic electron interacting with a nucleus, experiencing a Coulomb deflection such that $E, E' \ll Mc^2$, where M is the rest mass of the nucleus and E, E' are the electron energies before and after the collision, the differential cross section for the fraction of photons radiated per unit energy interval (units of area/energy) under the Born approximation is [84]:

$$\frac{d\sigma}{d(\hbar\omega)} \simeq \frac{Z^2 e^6}{12\hbar\pi^3\epsilon_0^3 M^2 c^3}\left(1 - \frac{\hbar\omega}{E} + \frac{3}{4}\frac{(\hbar\omega)^2}{E^2}\right)\left[\ln\left(\frac{2E\,(E-\hbar\omega)}{Mc^2\hbar\omega}\right) - \frac{1}{2}\right]\frac{1}{\hbar\omega} \tag{4.1}$$

for $\hbar\omega/E < 1$. This has a characteristic $1/\hbar\omega$ fall off for low photon energies and a cut-off close to the initial electron energy. For low energy photons, the doubly differential cross section for the fraction of photons radiated per unit energy interval per unit solid angle is:

$$\frac{d^2\sigma}{d(\hbar\omega)d\Omega} = \frac{3\gamma^2}{2\pi}\frac{1+\gamma^4\theta^4}{(1+\gamma^2\theta^2)^4}\frac{d\sigma}{d(\hbar\omega)} \tag{4.2}$$

where θ is the emission angle. The emission is confined to a cone of angle $\theta_c \sim 1/\gamma$ *radians*.

To estimate the bremsstrahlung photons and the consequent pair production, a number of Monte-Carlo simulations using FLUKA and MCNP were perfomed as shown in Figures 4.1 and 4.2. These simulations indicate that a significant population of low-energy photons are produced with large divergence. This is shown in Figure 4.2, where the on-axis portion is relatively flat-top extending to the maximum electron energy (350 MeV). The 6 MeV portion of the photon spectrum, useful for active interrogation, is 99% contained in a 14° on-axis cone as shown in Figure 4.2(f). It

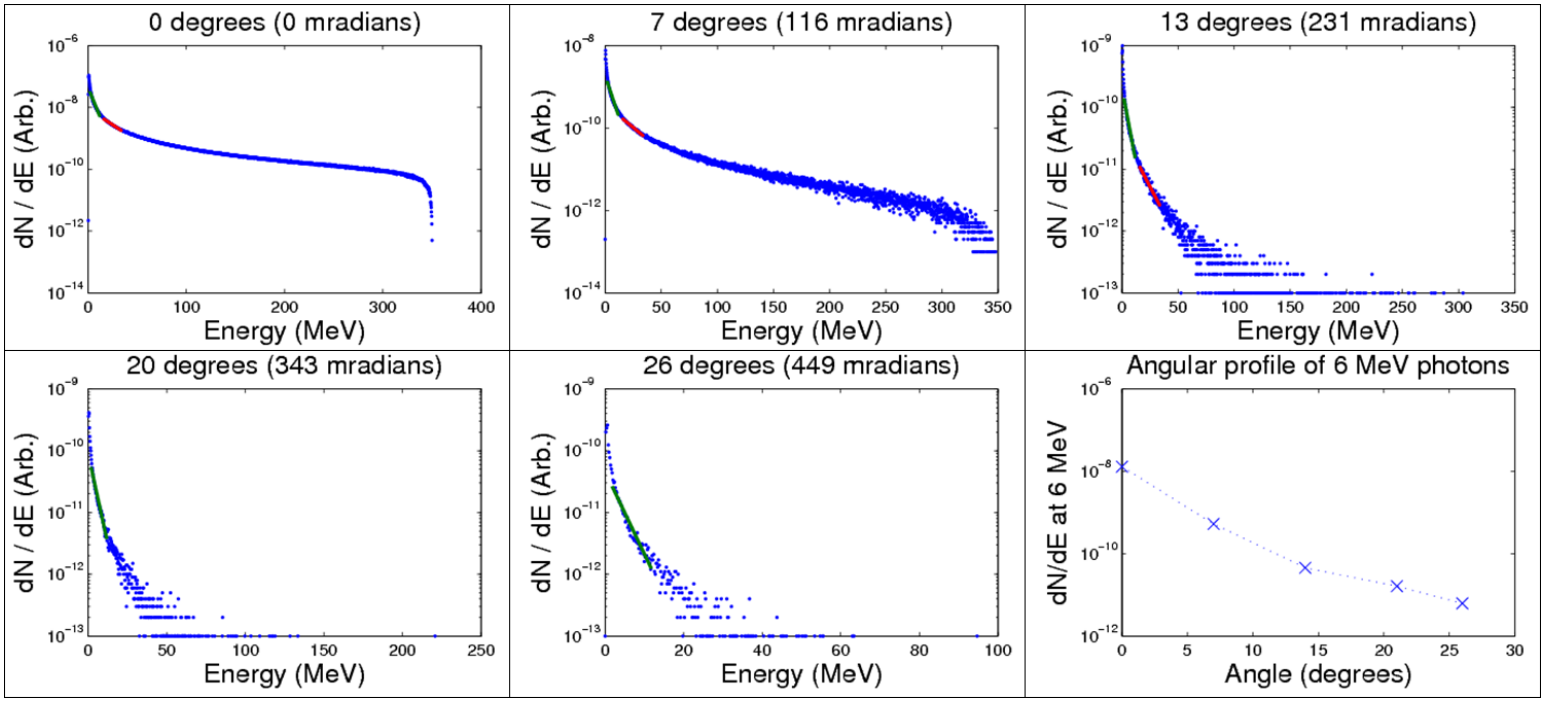

Figure 4.2: Simulated bremsstrahlung spectra from MCNP at various angles for a flat-top spectra electron beam up to 350 MeV interacting with a 4 mm Pb converter. Reproduced courtesy of Calvin Zulick, University of Michigan.

would follow that higher energy photons fall into an even smaller cone angle.

4.2.1 Photon Energy Measurement

Due to the short-pulse and high-energy nature of LWFA bremsstrahlung, traditional single-photon detectors such as HPGe semiconductor detectors are unable to spectrally resolve these photons. The simplest, yet crudest, method to resolve the energy spectrum is to introduce progressively thicker high-Z filters in the beam to absorb/attenuate the beam while sampling the filtered beam with numerous NaI or BGO scintillators. However, this requires detailed Monte-Carlo modeling efforts to deconvolve the spectrum [85] and leads to significantly reduced energy resolution due to the low number of sampling scintillators and filter sets.

On the other hand, a technique employing Compton-scattering can yield the incident photon energy spectrum quite accurately, but requires a larger flux to become practical for shot-to-shot measurements. This technique involves a low Z converter in which the photon Compton-scatters off an electron, imparting most of its momentum to the electron. In Compton scattering, for an electron initially at rest the final energy of the electron, E_{e^-}, depends on the scattered angle and is given by:

$$E_{e^-} = \left(1 - \left[\frac{h\nu}{m_e c^2}\left(1 - \cos\theta\right) + 1\right]^{-1}\right) h\nu \tag{4.3}$$

where θ is the angle between the momentum of the *incident* photon (with energy $h\nu$) and the *scattered* photon. Therefore, for $h\nu \gg m_e c^2$ and backward scattering ($\theta = \pi$), the forward scattered electron (with energy E_{e^-}) will have energy:

$$E_{e^-} = h\nu - \frac{m_e c^2}{2} \tag{4.4}$$

which is very close to the original photon energy.

This conversion is preserved by lower-Z materials as the higher-Z tend to broaden

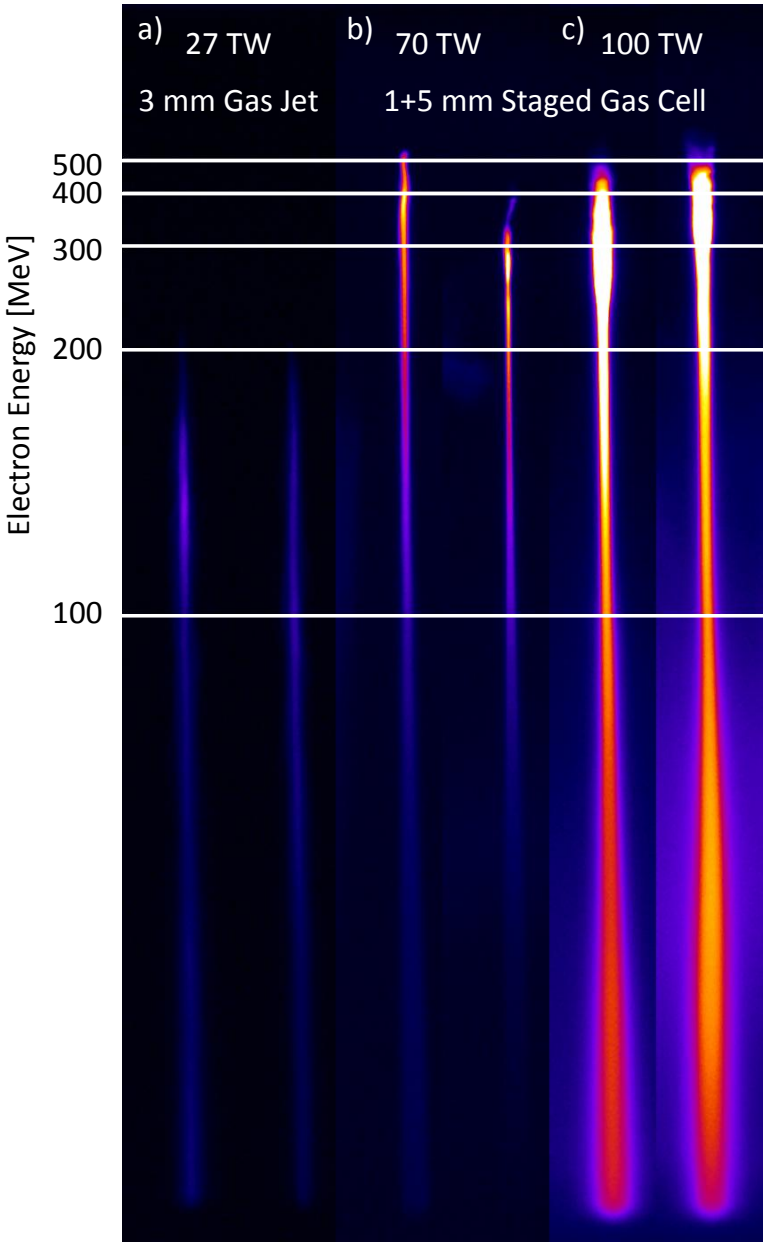

Figure 4.3: Typical electron spectra used in (a) the Compton spectrometer experiment with 27 TW laser power and a 3 mm gas jet, (b) the autoradiography experiment with 70 TW and (c) the activation experiments with 100 TW and a 1+5 mm staged gas cell (7 mm total plasma length including 1 mm inner separator). Note that the color scale is the same for all spectra and that the energy peaks of (c) saturated the 12-bit CCD camera.

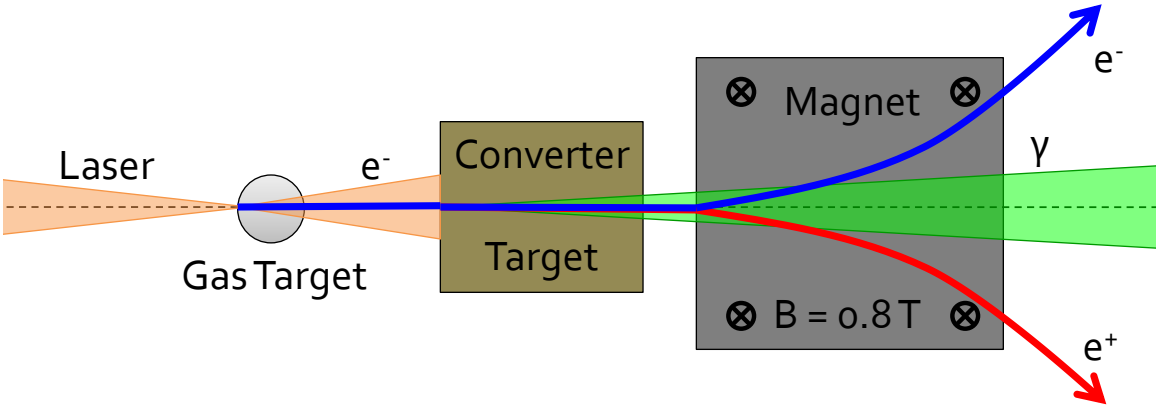

Figure 4.4: Simplified experimental geometry for bremsstrahlung photon generation and pair production.

the photon energy by electromagnetic cascading and scattering, which in turn broadens the energies of the forward-scattered electrons. If only the electrons in the propagation direction are collected by means of a collimator, then they can be spectrally resolved with a dipole magnet and scintillator, yielding an electron spectrum which can be easily deconvolved to yield the input photon spectrum. However, the downside is that the conversion efficiency for forward-scattered electrons is $\sim 10^{-4}$ electrons/photon/radiation length for hydrogen (the lowest Z material) and scales as Z^2/A. Another downside arises with the properties of low Z materials (specifically, gaseous H_2/He at room temperature and flammable Li in moist air), as the converter must be a pipe filled with high pressure H_2/He or a sealed block of elemental Li to minimize Z. Regardless of the converter configuration, the total converter length must allow the forward-scattered electrons to escape the converter before they noticeably scatter and lose energy, meaning the secondary converter must be relatively thin in terms of the total number of radiation lengths.

The preliminary bremsstrahlung experiment was performed on the HERCULES laser system with <30 TW of laser power in an $f/20$ focusing geometry with a 3 mm gas jet using 2.5% N_2 in He. This configuration produced broad energy electron

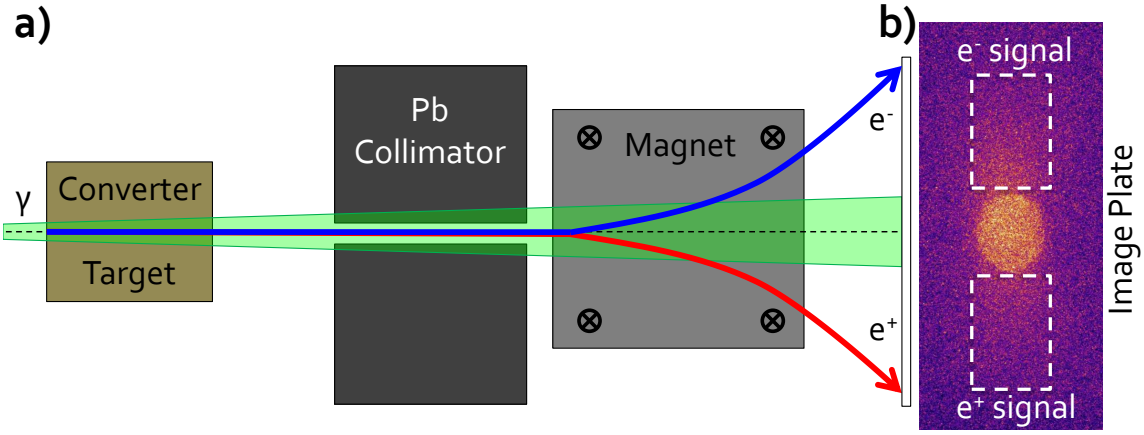

Figure 4.5: (a) Compton-scattering spectrometer geometry. Note that the Pb collimator blocks the off-axis charged particles, but can cause contaminant signal as a converter. (b) Raw image plate signal with outlined regions-of-interest. The signal in the center is from the on-axis photon beam.

beams up to 200 MeV with nearly 60 pC of total charge as shown in Figure 4.3(a). The converter targets included Cu, Sn, Ta, and Pb from 0.5 to 8 mm in length. These converters were installed 1 cm behind the gas jet to allow the main spectrometer magnet measure both electrons and positrons. The simplifed bremsstrahlung generation geometry is shown in Figure 4.4. After the primary e^-/e^+ were removed with the primary spectrometer magnet, the photon beam propagated 40 cm before passing through the 4 cm LiF converter to generate secondary e^-/e^+. These secondary e^-/e^+ then propagated another 1 m before encountering a 5 cm thick Pb collimator with a Ø15 mm aperture. Those that passed through the aperture were immediately swept by a 5 cm long, 0.3 T magnet onto an image plate 20 cm away. The spectrometer geometry and a typical image plate are shown in Figure 4.5.

Due to bremsstrahlung photons scattering onto the image plate, the e^-/e^+ signal was background corrected using the shielded portions parallel to the magnet gap direction on the image plate. The extracted e^-/e^+ signal is shown in Figure 4.7(a). Also, since the e^+ signal is the result of pair production, this must be subtracted from the e^- signal to yield the Compton scattered contribution. Considering the

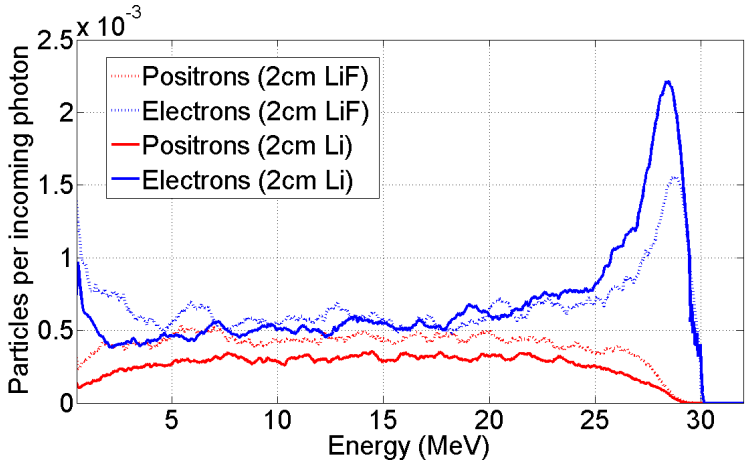

Figure 4.6: Simulated spectra of secondary electrons (red) and positrons (green) emitted on-axis from 30 MeV mono-energetic photons interacting with 2 *cm* lithium (solid) and 2 *cm* LiF (dashed) converter target. Reproduced courtesy of Gianluca Sarri, Queen's University of Belfast.

response of the converter material (Figure 4.6), the incident photon spectra can be deconvolved from the Compton scattered electrons. The extracted photon spectrum from a 60 pC, 200 MeV electron beam impacting a 2.8 mm Ta primary converter is shown in Figure 4.7(b).

After this diagnostic was successfully fielded with LiF on HERCULES, the next attempt using H_2 was peformed on the ASTRA-GEMINI laser system with 200 TW of laser power in an $f/20$ focusing geometry with a 15 mm gas jet using 3% N_2 in He. In this configuration, broad energy electron beams up to 1.2 GeV (typically 800 MeV) were produced with nearly 500 pC of total charge and interacted with converters composed of up to 5 cm of Pb. However, due to the limiting geometry (2 $mrad$ acceptance angle) and lowered conversion efficency ($>$ 10% compared to LiF) of the H_2-filled tube, no conclusive results were observed. A follow-up run on ASTRA-GEMINI using Li/LiF produced similar results to HERCULES and is shown in Section 5.2.2.

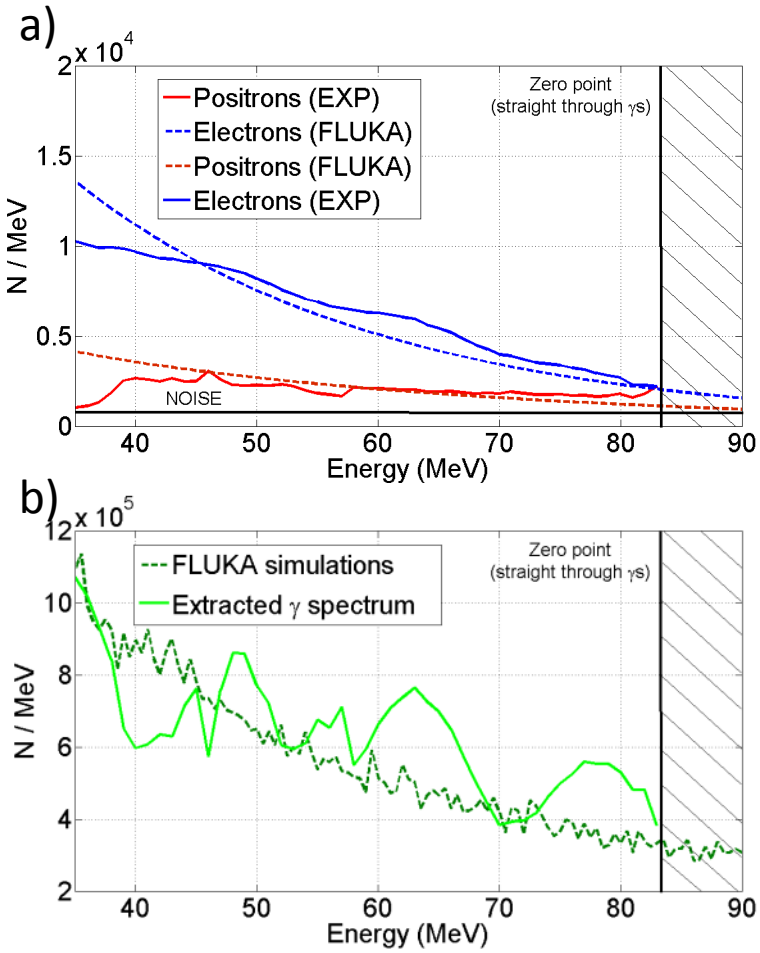

Figure 4.7: (a) Measured (solid) and simulated (dashed) spectra for secondary electrons/positrons from Compton scattering through 4 *cm* LiF. (b) Extracted (light green) and simulated (dark green) photon spectra based on electron/positron energies. Reproduced courtesy of Gianluca Sarri, Queen's University of Belfast.

4.2.2 Flux Measurement

There are numerous methods for measuring the instantaneous flux of bremsstrahlung photons. However, all of them are highly dependent on the spectral sensitivity of the detector. Above $E_{h\nu} \geq 1\ MeV$, the cross-section for Compton scattering/pair production becomes dominant, making it difficult to determine the photon flux at a certain energy via direct photon absorption. Therefore, we employed high-energy threshold reactions to characterize $> 10\ MeV$ photon flux. Another consideration is how the radiation is measured (coincidence, integration on IP, HPGe detector, etc.). This section will detail three methods of high-energy threshold reactions: prompt activation, ^{238}U photofission, and autoradiography (covered in more detail inSection 4.2.3).

If the photon has enough energy to dislodge a neutron or proton from the nucleus, the remaining isotope may be radioactive. For (γ, n) reactions, the resultant nuclei become proton-rich and typically undergo β^+ decay, emitting a e^+ which quickly annihilates into two 511 keV photons. In low-Z nuclei, the β^+ decay process occurs rapidly (half-lives can be as short as a few *seconds*). Since this radioactivity is short-lived, it can easily be integrated in single-shot or low-repetition rate ($< 0.02\ Hz$) experiments [86].

One significant advantage of the (γ, n) reaction is the coincidence of the 511 keV photons, this allows for a highly selective detector that can distinguish β^+ decays from background radiation using a coincidence unit. For these experiments, we used a matched pair of NaI scintillators that were Ø75 $mm \times 75\ mm$. These were gated with timing single-channel analyzers (timing SCAs) to produce logic pulses for 450 ± 100 keV of deposited energy in each scintillator. When both scintillators produced a logic pulse within 100 ns of one another, a co-incidence unit sent a pulse to a digital counter which recorded the coincident signal as function of time and displayed the activity using LABVIEW software.

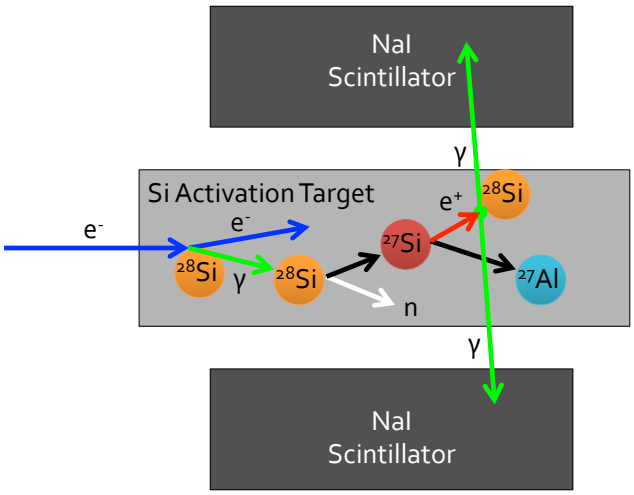

Figure 4.8: Nuclear reaction diagram for ^{28}Si activation. Bremsstrahlung photons dislodge neutrons from ^{28}Si to give ^{27}Si which undergoes β^+ decay (half-life of 4.15 s) and emits a e^+ which quickly annihilates with a nearby e^- to give two 511 keV photons.

To maximize the prompt activity, silicon was chosen due to its short β^+ half-life (4.15 s), high-energy (> 10 MeV) threshold for (γ, n), and high material purity (99.999%). Other materials (Cu, SiO_2, Al, and $CaCO_3$) were used to compare activity rates and thresholds. The calculated, normalized activity rates for most of these materials irradiated by 10^6 photons of 20 MeV energy are shown in Figure 4.9a. Since the cross-section for most of these reactions is relatively similiar ($\sim$ *millibarns*) between different materials, the peak activity is largely correlated to the shorter half-life materials as they decay more rapidly.

To characterize the flux from a 400 MeV broad spectrum electron beam (see Figure 4.3c), a 1×1 cm^2 area by 10 cm long silicon bar was placed on axis with the beam at 1.2 m from the gas cell. No upstream converter was used in order to localize the photon transport to within the Si rod; however, the electron beam did pass through a 0.6 mm Be window which was 10 cm in front of the Si rod, inducing some scattering and bremsstrahlung. To avoid collecting shot noise and nuclear fluorescence from the interaction, we gated the counter for 100 ms after

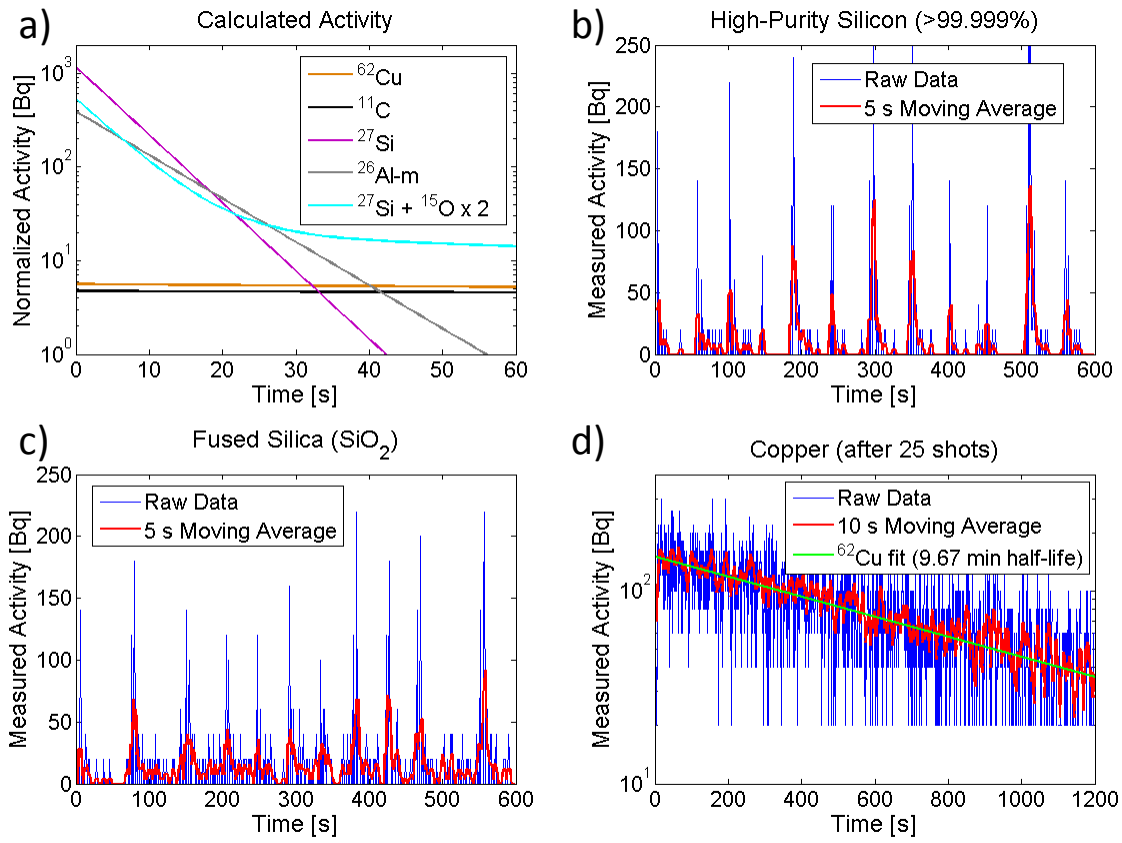

Figure 4.9: (a) Calculated activities for various materials irradiated by 10^6 photons of 20 MeV energy normalized according to abundance and density. (b) & (c) Experimental (blue) and averaged (red) activity traces from multiple shots on (b) high-purity Si and (c) fused silica (SiO_2). (d) Experimental activity (blue), averaged (red), and expected (green) traces of 25 shots accumulation on Cu.

the shot occured. However, the counting electronics were not heavily shielded and exhibit some electronic noise (spurious counts) after shots, forcing us to ignore the first few *seconds* after the interaction during analysis. The pixellated scintillator, placed behind the activation sample and 50 mm Pb shielding, was used to align the rod on axis with the beam.

Over the course of 20 shots, the measured activation on Si varied with the pointing and charge of the beam as shown Figure 4.9(b). Overall, the measured activity had a half-life of 4.06 ± 0.67 s and an initial activation of 648 ± 320 *decays* as estimated by fitting individual curves. The low number of measured decays was likely due to the scatter of the beam before entering the sample and the inefficient bremsstrahlung conversion within the relatively low-Z sample. However, given the 0.12% probability of a photon inducing a reaction in 100 mm rod (peak cross-section of 12 *millibarn* at 20 MeV), the estimated photon flux above 15 MeV is of order of 5×10^5 $photons/cm^2$.

Alternatively, fused silica (SiO_2) and copper rods of $\emptyset 12.7mm \times 100mm$ size were used to demonstrate different aspects of activation. An activity trace of electron beams entering fused silica is shown in Figure 4.9(c). Activation of oxygen (122 s half-life) in the fused silica sample establishes a low-level background between the short-lived silicon peaks. To investigate longer half-life materials, 25 shots were taken on a Cu sample (^{62}Cu half-life is 9.67 min). The Cu activity clearly follows the expected exponential decay as shown in Figure 4.9(d). Assuming each shot contributed roughly the same signal and taking into account the time between shots, a simple rate equation can model the build-up of activity until shots cease. By fitting the decay curve of Cu to yield the initial activity after shots and in conjuction with this simple model, a estimate of the activations for a single-shot can be estimated as 4200 $decays/shot$, corresponding to a flux of 3×10^6 $photons/shot$ above 10 MeV given the 0.2% probability of interaction (over 100 mm of Cu with 70 *millibarn* at 17 MeV).

Another method of creating radioactive isotopes is through the process of photo-

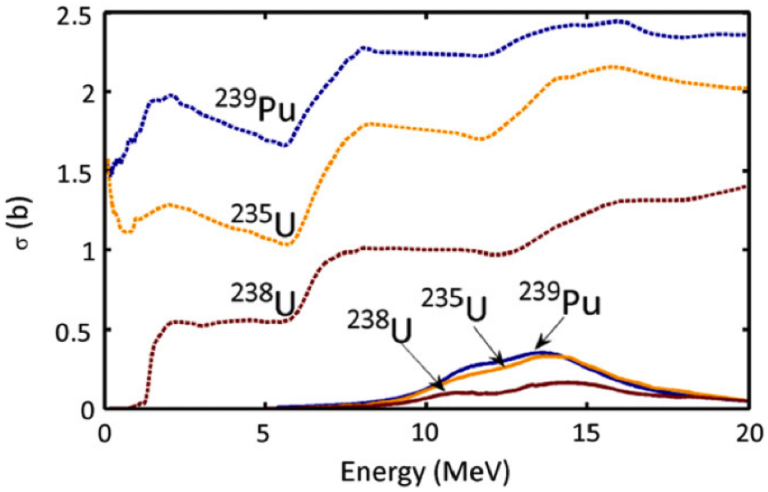

Figure 4.10: Reaction cross sections in *barns* for neutron-induced (dashed) and photon-induced (solid) fission as a function of incident particle energy for various special nuclear materials (SNMs).

fission [87, 88]. When certain nuclei absorb high-energy photons, they can be excited into a giant dipole resonant state and consequently undergo fission [89]. Some of these fission products are radioactive and emit characteristic γ-rays. Using a HPGe detector to peform nuclear spectroscopy on the sample, these fission products can be measured and used to estimate the incident photon flux. Another application of this process is the active interrogation of special nuclear materials (SNMs) for homeland security. The fission cross-section for neutrons and photons interacting with various SNMs is shown in Figure 4.10.

For experiments with HERCULES, we used depleted uranium (DU), which contains more ^{238}U than natural uranium, for our photofission samples. The first sample was a 3.2 mm thick metallic piece of DU. The second sample was an uranium oxide (UO_x) powder containing DU which could be packed into various-size containers. The fission fragments primarily studied were ^{134}I (847, 884 keV), ^{138}Cs (1436 keV), and ^{134}Sr (1384 keV) due to their medium-lived half-lives (52.5 min, 33.4 min, and 2.61 hr, respectively).

The electron beam used for photofission was generated with a 1+5 mm staged

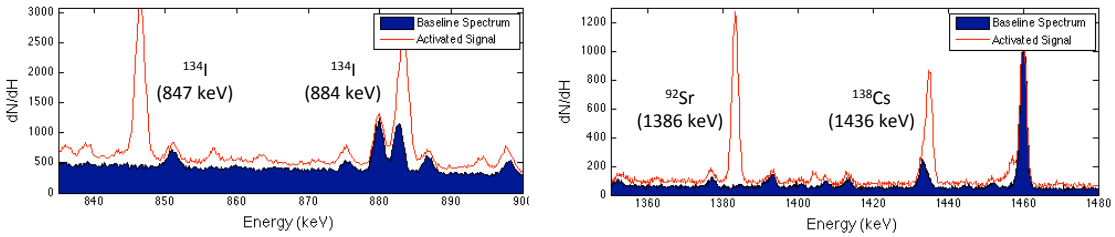

Figure 4.11: γ-ray spectra integrated over 3 *hours* from activated ^{238}U showing the fission fragment decay peaks clearly above background. Reproduced courtesy of Anthony Raymond, University of Michigan.

gas cell, producing electron beams with spectra of up to 500 MeV and charge of 100 pC, similar to spectra shown in Figure 4.3(b). To optimize the electron-to-photon conversion, we placed 4 mm of Pb ($d \sim L_{rad} \simeq 5mm$ for Pb) 5 cm behind the gas cell. The DU foil sample was directly attached to rear of the coverter.

Over the course of an hour, the sample was activated with 50 shots. The results are shown in Figure 4.11. From the measured 3000 *decays*, the number of fissions per shot can be calculated using the 2% branching ratio of fission fragments, 0.1% inherent detector efficency, 1% geometrical detector efficiency, and a simple rate equation (assuming each shot deposited identical signal). This calculation yields $3(\pm 2) \times 10^7$ $fissions/shot$, corresponding to a flux of $\sim 3 \times 10^8$ $photons/shot$ above 10 MeV given the 10% probability of interaction (3.2 mm thick with cross-section of 0.18 $barn$). This agrees well with the simulations shown in Figure 4.1(b), which indicates 10^8 $photons/MeV$ from 10-20 MeV. Moreover, it is a factor of 100 $\times$ improvement in photo-fission yield using LWFA from previous results [87, 88], presumably due to increased injected charge and higher energy electrons leading to an increased flux of 10-20 MeV photons which induce photofission. Also, the higher photon number compared to the short-lived (γ, n) activation is likely due to proximity of the ^{238}U to the electron source (120 cm versus 5 cm), allowing it to more consistently collect electrons which are more divergent or miss the target due to shot-to-shot pointing issues.

4.2.3 Spatial Measurements

There are also numerous methods (IPs, scintillator screens/arrays, CCDs, etc.) for measuring the spatial distribution of bremsstrahlung photons. However, all of them are highly dependent on the collection efficiency of the detector. Around $E_{h\nu} \simeq 1\ MeV$, the cross-section for Compton scattering/pair production interaction levels is relatively low for most materials, making it difficult to entirely absorb and directly determine the photon flux at a certain energy. Therefore, we employed large volume detectors or higher-energy reactions to characterize $> 10\ MeV$ photon flux.

In theory, image plates could be used for spatial detection; however, due to their thin detection layer, only photons up to 100 keV can be completely absorbed in a single IP. Given this low absorption probability for high-energy and high absorption for low-energy photons, it is considerably more difficult to determine the high-energy contribution to the spatial distribution of the beam . Thus, even with relatively thick, high-Z shielding, the radiation transport in the shielding will severely degrade the detection of the high-energy photon distribution without performing Monte-Carlo modeling. This method is also limited to single-shot due to the IP readout process.

Using a larger detector volume, more of the photon energy can be absorbed, resulting in more efficient detection. This was accomplished with a pixellated BGO scintillator composed of a 25×25 array of $1 \times 1 \times 50\ mm^3$ macropixels or "voxels", each separated by a thin (100 μm) coating of titanium dioxide for optical isolation. The scintillator array was read out by the Andor iKon-L fiber-coupled CCD attached to the open-end of the scintillator. Example images are shown in Figure 4.12 with and without an activation rod on axis. This allows for shot-to-shot spatial measurements of the high-energy portion of beam, enabling fine alignment of activation samples that must be placed directly on axis with the electron/photon beam. This is particularly important as the electron beam does not always follow the laser alignment axis due to deflections in the plasma. The alignment of a 100 mm Cu rod is shown in Figure

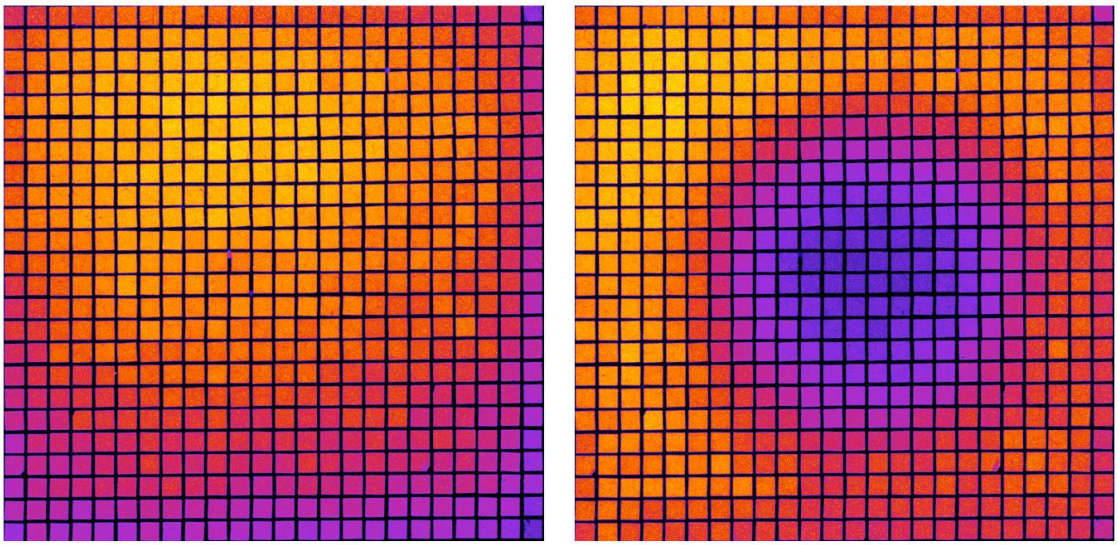

Figure 4.12: Pixellated scintillator images of the photons from the activation experiment without (left) and with (right) the Ø12.7 mm × 100 mm long Cu rod. Note that each macropixel or "voxel" of the scintillator is 1×1 mm^2. The detector was shielded with 50 mm of Pb.

4.12(b).

Special precautions must be taken when the electron beam is not deflected away from the camera. This situation requires additional shielding since electrons (charged particles) create much more scintillation light than photons. Typically 50 mm of Pb ($d \sim 10L_{rad}$) was used to shield the camera from direct electron interactions.

Besides measuring the exponential decay of the activation signal, the spatial distribution of activation can be measured by placing a spatially sensitive, integrating detector (such as imaging plate, film, CCD, etc.) on the sample after the shot in a process known as autoradiography. In our configuration, one of the two escaping 511 keV photons was recorded spatially on the image plate and over the course of numerous decays produced an image of the activation spatial distribution. The sample must be activated for a few minutes in order to be transferred and subsequently read-out as the image plates must be installed after the shot to prevent background. Copper and carbon targets were chosen for their moderate half-lives of 9.67 and 20.33 *minutes*

(see Figure 4.9(a)), respectively, and their different (γ, n) activation energy thresholds (10 and 20 MeV, respectively). The separate energy bins enables a spectrally notched gamma-ray spectrometer to spatially measure photons above threshold energy with essentially zero background from the low-energy portion of the spectum. For photon spectra extending to significantly higher energies (as in our experiment), the ability to measure differences across these spectral bins becomes marginal. However, for photon spectra in this range, the ability to measure these two spectral components accurately is useful for characterizing exponential tails of low energy spectra [90, 91] and the peak photon energy of broad spectra beams.

For the experiment, we placed various samples of copper and graphite on-axis with the 500 MeV peak, 180 pC average charge electron beam (Figure 4.3(b)) in place of the silicon sample as described in the previous section. The stack consisted of 4 cm Cu, 3.2 mm Cu, and 15 mm C in order of increasing distance from the gas target where the 4 cm Cu acted as the primary converter. The activation plates were integrated for 20 shots and were read out by separately image plates for 1 hour (collecting 98% and 88% of the signal for Cu and C, respectively). The spatial profiles of the electron beam impacting the 4 cm Cu, 3.2 mm Cu, and 15 mm C are shown in Figure 4.13(a-c), respectively. Taking a lineout across each signal (Figure 4.13(d-f)), the divergence of the beam on 4 cm and 3.2 mm Cu was measured to be roughly 10 $mrad$ full-width-at-half-maximum (FWHM). Since 511 keV photons are the primary contributors to the signal, the image plate signal can also be integrated to estimate the total photon flux. While typically used only for spatial characterization, autoradiography can also double as a flux measurement if carefully analyzed. For the 3.2 mm Cu, average activations were 2×10^4 activations/shot, implying a 10 MeV flux of 2×10^7 photons/cm^2 given approximately 0.1% probability of capture in the 1 cm^2 area and 3.2 mm thickness.

One important consideration is the thickness of the sample. Thicker samples

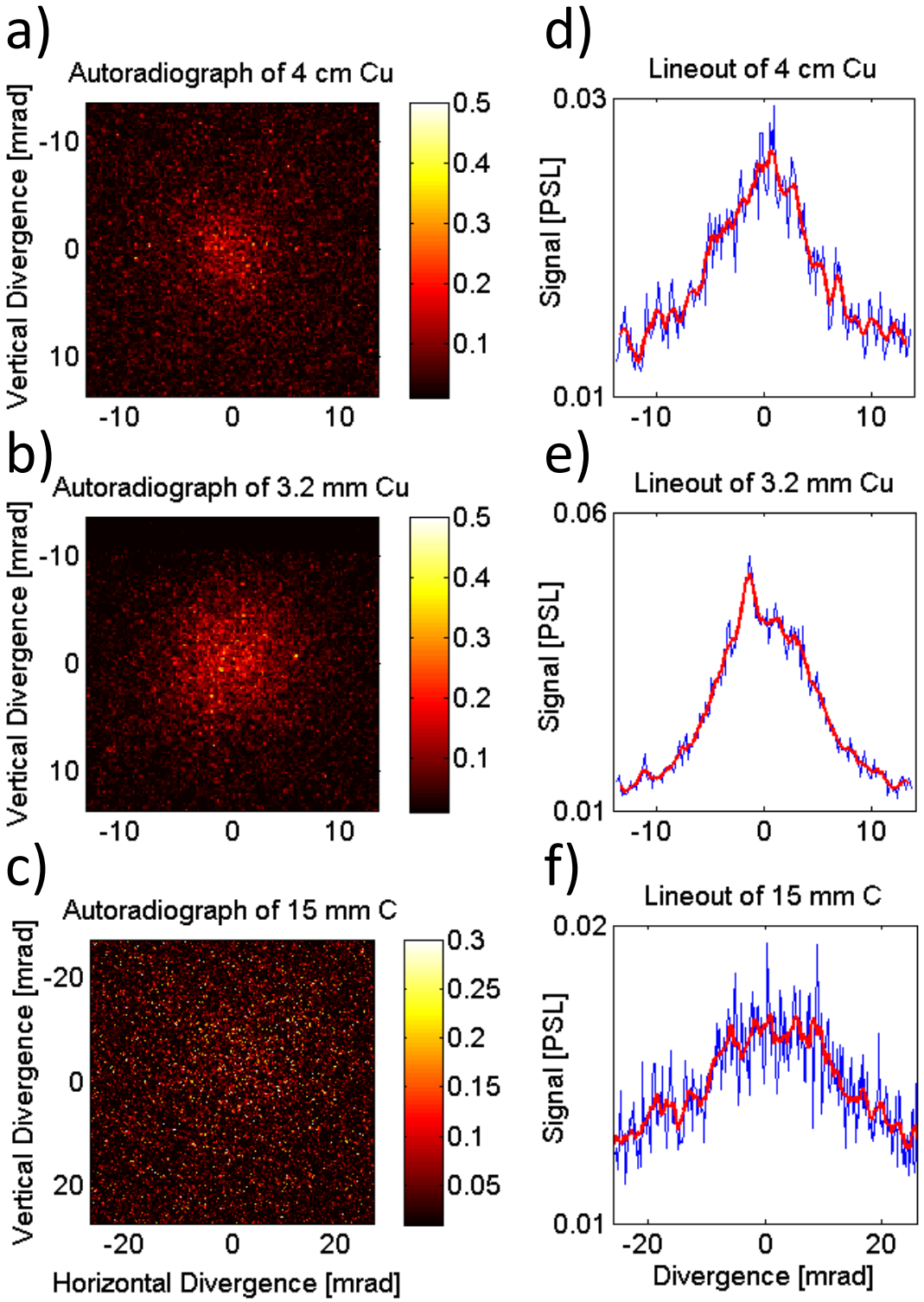

Figure 4.13: Autoradiographs of 20 shots for (a) 4 *cm* of Cu, (b) 3.2 *mm* of Cu, and (c) 15 *mm* of C in units of photostimulated luminescence (PSL). (d-f) Horizontal line-outs taken across each respective image. Note that (a) & (b) are on the same scale.

undergo more activations, but the detector collects scattered photons and secondary particles from deep in the sample and photons travelling greater distances before exiting the sample, thereby increasing the background. This effect was observed between the 4 cm and 3.2 mm samples of Cu.

4.3 Positrons

Positrons are the most common form of anti-matter, produced naturally through β^+ radioactive decay. There are two primary methods to generate positrons with lasers: through nuclear activation to produce β^+ emitters (covered in Sections 4.2.2 and 4.2.3) and through e^-/e^+ pair production. For high-energy electron beams interacting with converter targets, there are two possible mechanisms to generate e^-e^+ pairs: the single-step Trident process and the two-step Bethe-Heitler process.

The Trident process has the electron directly interacting with the nuclear field, interacting with a "virtual" photon that is immediately transformed into a e^-e^+ pair.

$$e^- + Z \rightarrow e^- + Z + e^- + e^+ \tag{4.5}$$

For $d/L_{rad} \gg 10^{-2}$, the Bethe-Heitler process [83] will dominate as the production of photons exponentially increases with the converter thickness. These photons can subsequently interact with the nuclear field to induce e^-e^+ pair production.

$$e^- + Z \rightarrow e^- + Z + \gamma \tag{4.6a}$$

$$\gamma + Z \rightarrow Z + e^- + e^+ \tag{4.6b}$$

Positron production using lasers has been explored previously using SM-LWFA with low power ($\sim TW$)[92, 93] and hot electron generation in solid targets [94, 95, 96]. However, in both scenarios, the positron beams were relatively low-energy ($E_{e^+} < 20$

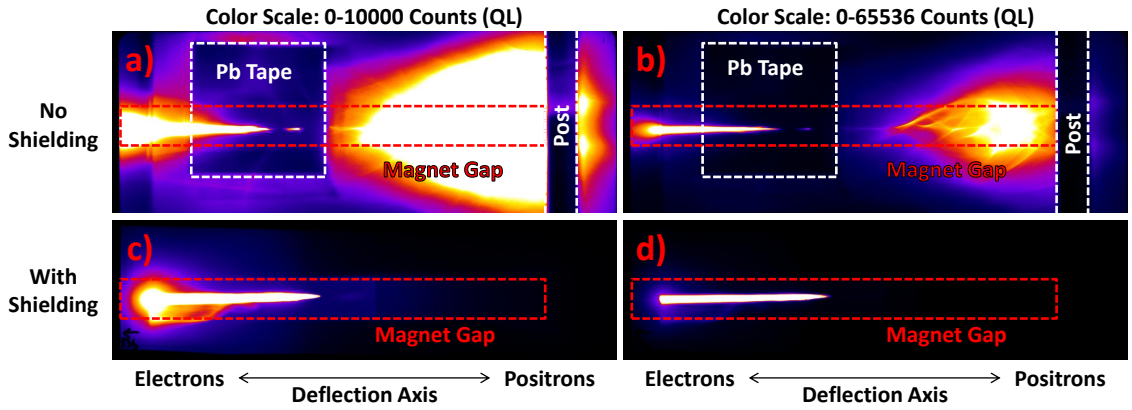

Figure 4.14: Image plate directly installed behind the primary magnetic spectrometer before (a)&(b) and after (c)&(d) plastic shielding was installed in front and in the side-cusps of the magnet.

MeV, $\gamma_{e^+} < 40$) and high-divergence ($\theta_{e^+} > 100\ mrad$) due to the low energy and high-divergence of the electron beams creating them.

It must be noted that positrons have been routinely generated with LWFA electrons interacting with solid targets or in beam dumps. However, since these experiments/configurations were not looking for positrons or had poor resolution, the positrons had gone unmeasured. On HERCULES, the measurement of positrons was initially hindered by background low-energy electrons from LWFA passing through cusps of the primary spectrometer magnet as shown in Figure 4.14(a)&(b). This was remedied by installing low-Z plastic (HDPE and Teflon) around the magnet to form a collimator, removing the positron background as shown in Figure 4.14(c)&(d).

4.3.1 Experimental Setup

The basic experimental geometry for measuring positrons is shown in Figure 4.4. LWFA electrons initially pass through a converter target to create bremsstrahlung photons (Section 4.2) which then create e^-e^+ pairs through the Bethe-Heitler process. The e^-/e^+ beams exit the converter and are separated by a magnetic spectrometer before measured by a IP or LANEX. Due the divergence scaling ($\theta_{e^-/e^+} \propto 1/\gamma_{e^-/e^+}$),

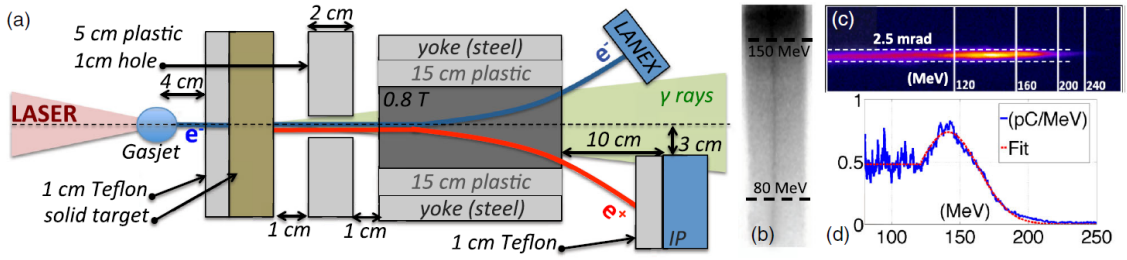

Figure 4.15: (a) Top view of the experimental setup used on HERCULES. The magnet is rotated by 90° for the sake of illustration. (b) Typical positron signal as recorded by the image plate for 4.2 mm of Ta. The dark region on the upper part is predominantly exposed by bremsstrahlung escaping the solid target. (c) Typical signal of the electron beam as recorded on the LANEX screen, without a solid target for a ten-shot series. The dashed white lines depict a full width at total maximum of 2.5 mrad (corresponding FWHM of 1.4 mrad). (d) Extracted spectrum and relative best fit used as an input for FLUKA simulations.

the high-energy portion of the positron beams has a similiar divergence to the incident electron beam and will pass through the collimator. To prevent divergent, low-energy e^-/e^+ from creating background on the detector, *cm*-thick plastic collimators were placed at the entrance of the magnets. However, divergent bremsstrahlung readily passes through this plastic and creates a low-level background on the detectors that falls off axially (Section 4.2.3).

The initial positron experiments took place on HERCULES in conjunction with the characterization of the Compton scattering photon spectrometer (Section 4.2.1). As such, the LWFA parameters were identical to those described in Section 4.2.1, using broadband electron beams with 50 pC of charge and up to 200 MeV energy (shown in Figure 4.15(c)&(d). The experimental setup on HERCULES is shown in Figure 4.15(a).

A raw IP of positron signal from a 4.2 mm Ta converter is shown in Figure 4.15(b) with the contaminant bremsstrahlung signal close to the axis. The extracted spectra from various converters are shown in Figure 4.16. For the low-Z materials, the noise was a significant fraction of the signal and had to be carefully subtracted to isolate the desired signal. For higher Z, the noise was roughly the same level, but the larger

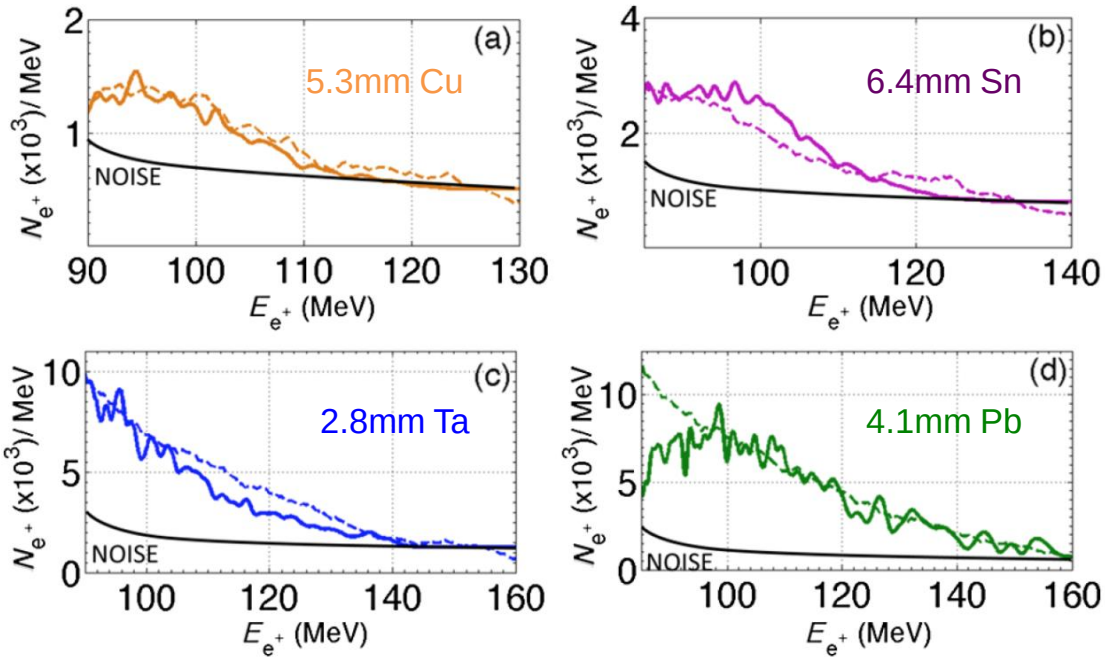

Figure 4.16: Extracted experimental (solid) and simulated (dashed) positron spectra from (a) 5.3 mm Cu, (b) 6.4 mm Sn, (c) 2.8 mm Ta, and (d) 4.1 mm Pb using 50 pC electron bunches on HERCULES.

signal was clearly identifiable from the background as shown in 4.15(b).

Due to the limited power and experimental time available on HERCULES, a follow-up positron experimental campaign was held at ASTRA-GEMINI using its North beam with 250 TW. This additional power helped two-fold by increasing both the electron beam energy and charge to ~ 1.2 GeV and ~ 0.5 nC, respectively, using ionization injection in gas jets. The experimental setup on ASTRA-GEMINI is shown in Figure 4.17. These orders of magnitude improvement allowed us to measure the positron spectra directly on a LANEX screen shot-to-shot, greatly expanding the available experimental parameter space in terms of the converter.

4.3.2 Converter Z Dependence

For the Bethe-Heitler process ($d \gg 0.01 L_{rad}$), increasing the Z of the converter material has a two-fold effect. First, the incident electrons convert more efficiently to

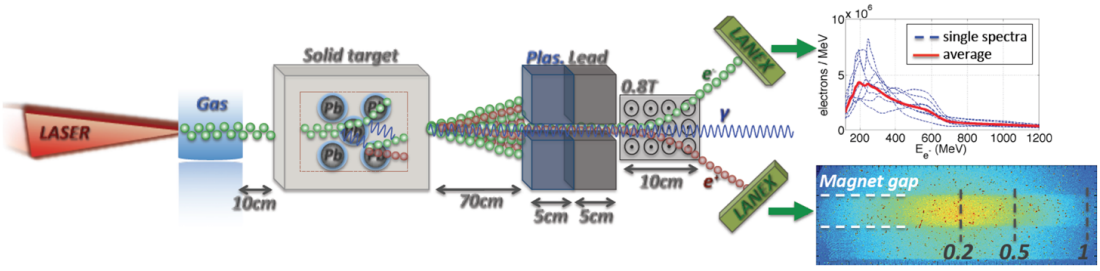

Figure 4.17: Experimental geometry used for neutral beam production on ASTRA-GEMINI. Extracted electron spectra are shown in the upper right, while the raw image of the positron signal is shown in the lower right.

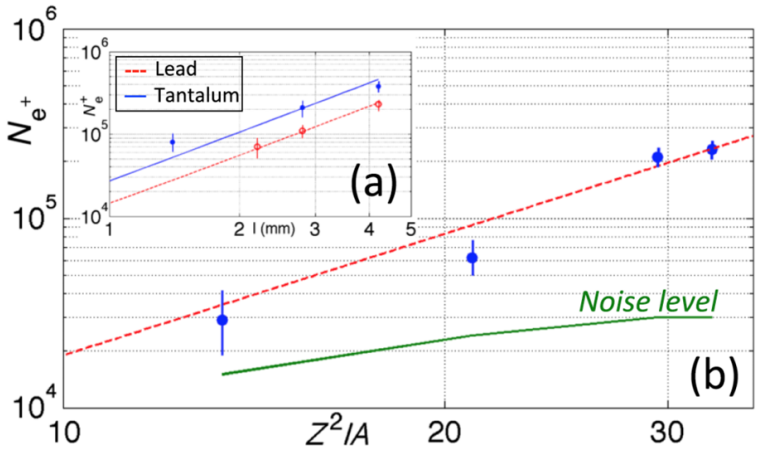

Figure 4.18: Positron production scaling at 100 MeV over (a) thickness (for $d < L_{rad}$) and (b) Z^2/A using the HERCULES laser.

bremsstrahlung photons, and second, the photons convert more efficiently into pairs. Since both processes scale roughly as Z^2, the overall scaling goes as:

$$N_{e^+} \propto \left(\frac{Z^2}{A}\right)^2 \tag{4.7}$$

where N_{e^+} is the consequent positron number. The experimental Z dependence from HERCULES is shown in Figure 4.18(b). While it is not proper to fit a fourth-order polynomial to only four points, a quadratic fit over Z^2/A closely follows the expected scaling.

This scaling largely prevents low-Z materials from consideration in experiments as

there is roughly 10^8 difference in efficiency between the lowest-Z (elemental hydrogen) and highest-Z (natural uranium) elements, density aside. However, between high Z elements, the effect of Z^4 provides slight gains (e.g. a 59% increased yield for Pb ($Z = 82$) over Ta ($Z = 73$) at a given density) compared to density effects (Ta is 47% denser than Pb). Therefore, high-Z materials were most employed and their thicknesses were used to vary the conversion efficiency as detailed in the next section.

4.3.3 Converter Thickness Dependence

Increasing the thickness of the converter has the primary effect of converting more incident electrons into bremsstrahlung photons and scattering the beam as it propagates further into the converter. The number of electrons exiting the converter is given by:

$$N_{e^-} \simeq N_{e^-}(0)\, e^{-d/L_{rad}} \tag{4.8}$$

where $N_{e^-}(0)$ is the initial number of electrons entering the converter, d is the converter thickness, and L_{rad} is the radiation length for electrons in the converter material ($L_{rad} = 0.5\ cm$ for Pb). This scaling is shown in Figures 4.18 (a) & 4.19(middle) along with the experimental and simulation results.

As the electron beam converts into bremsstrahlung propagating through the converter, the rate of pair production quickly increases before trailing off as the drive electron beam is depleted. The number of positrons (and pair produced electrons) exiting the converter is given by:

$$N_{e^+} \simeq N_{e^+}(0) \left(\frac{d}{L_{rad}}\right)^{\alpha} e^{-d/L_{rad}} \tag{4.9}$$

where $N_{e^+}(0)$ is the maximum number of positrons for a given material, d is the converter thickness, L_{rad} is the the radiation length for positrons in the converter material, and α is a scale factor (in the ASTRA-GEMINI experiment, $\alpha \simeq 1.8$). This

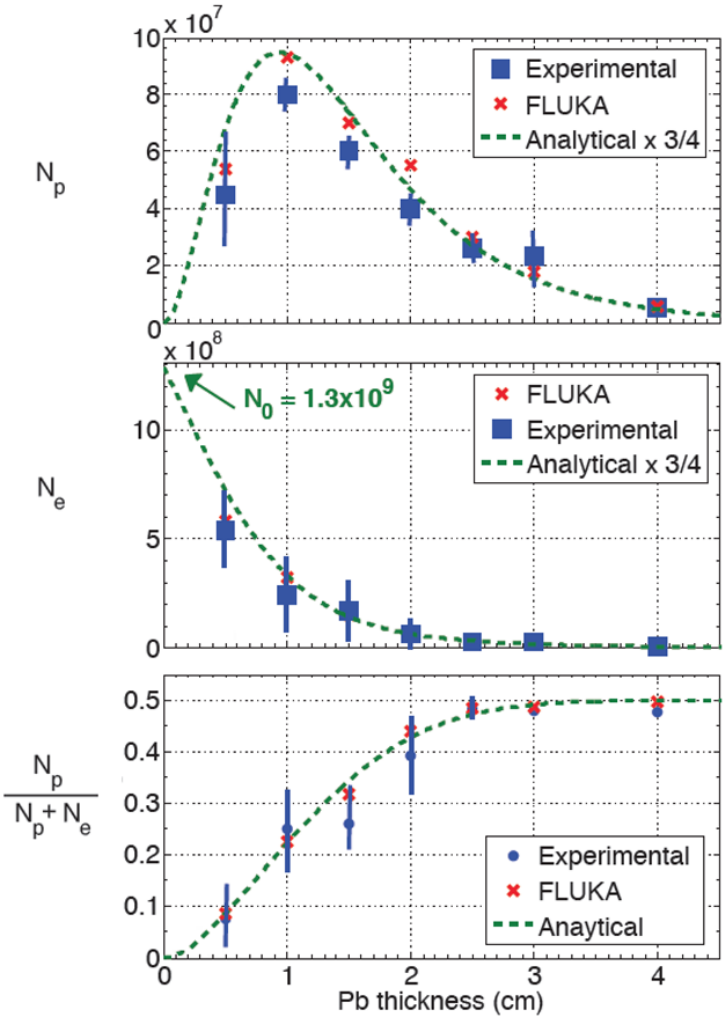

Figure 4.19: Positron (top) and electron (middle) production scaling over thickness for $E > 120\ MeV$ using the ASTRA-GEMINI laser. (bottom) the fraction of positrons in the total number of leptons in the beam. $N_{e^-}(0)$ is given by the initial electron beam charge (300 pC).

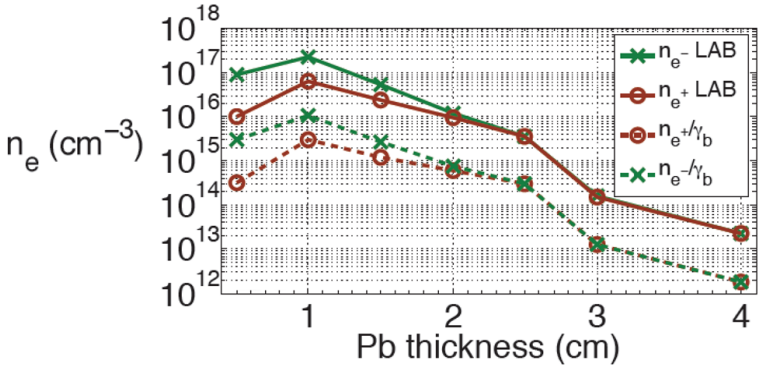

Figure 4.20: Density of relativistic electrons (green crosses) and positrons (red empty circles) as a function of the thickness d of the converter using ASTRA-GEMINI. The solid lines represent the density in the laboratory reference frame whereas dashed lines represent the beam proper density. A neutral electron-positron beam is obtained for $d = 2.5\ cm$.

scaling is shown in Figure 4.19(top) along with the experimental and simulation results. From the 1 GeV incident electron beam, the maximum observed positron energy is 600 MeV, occurring at $d \simeq L_{rad}$. However, the production of high-energy positrons is maximized at $d \simeq 2L_{rad}$. For thicker targets, the maximum energy gradually decreases as should be expected due to increased probability of energy loss during the propagation of the generated positrons through the rest of the converter. For a similar reason, a thicker converter allows a lower number of electrons and positrons to escape it.

When $d \simeq 5L_{rad}$, the percentage of positrons in the beam approaches 50% as shown in the bottom of Figure 4.19. This implies that the net current in the beam will drop to near zero, establishing a neutral beam. Since the conversion process introduces minimal longitudinal spread for highest energy particles ($E_{e^-/e^+} > 10$ MeV) due to relativistic effects, the resultant high-energy portion of the neutral beam will preserve the features of the incident electron beam which exits the plasma with $< 30\ fs$ duration and a $\sim \mu m$ source size (initially occupying $\sim 10\ \mu m^3$ volume). The transverse spread of the beam is increased through scattering to roughly a 200 μm

width. Using this volume ($\sim 2000\ \mu m^3$) and the number of particles ($N_{e^-/e^+} \simeq 10^9$), the density of the beam (in the laboratory frame of reference) can be estimated to be $n_{e^-/e^+} \approx 10^{15}\ cm^{-3}$, as shown in Figure 4.20. However, because the beam is relativistic, the relativistic density (in the beam frame of reference) is found by dividing by the bulk Lorentz factor of the beam (assuming $\gamma_{e^-/e^+} \approx 15$ in this case, similar to that shown in Figure 4.1). This results in a relativistic density of $n_{e^-/e^+,\gamma} \approx 10^{14}\ cm^{-3}$ for the neutral beam as shown in 4.20. For collective, plasma effects to dominate the beam dynamics, the collisionless skin depth ($\delta_e \approx c/\omega_{\gamma,pe}$, where $\omega_{\gamma,pe}$ is the relativistically corrected plasma frequency) must be less than the beam size.

4.4 Neutrons

Pulsed sources of neutrons are important for a variety of applications, especially active interrogation of special nuclear materials (SNMs). For a given energy, neutrons have a higher cross section for inducing a fission than photons for certain SNMs as shown in Figure 4.10. If the neutron generation time is known, then a detector can be gated to look for prompt or residual radiation from an induced fission, indicating a SNM is present. A compact, pulsed source of neutrons would be ideal for such an application and LWFA may provide the necessary mechanism for such a solution.

When the aforementioned bremsstrahlung photons possess enough energy to overcome the binding energy of the nucleus, a neutron can be freed in the following reaction:

$$\gamma + {}^{N}Z \rightarrow n^0 + {}^{N-1}Z \tag{4.10}$$

For lower Z materials, the energy required to free a neutron is quite variable, ranging from 1-21 MeV, but leveling off to roughly 7-9 MeV as Z increases. This is shown in Figure 4.21 [97]. From conservation of momentum, the neutron gets most

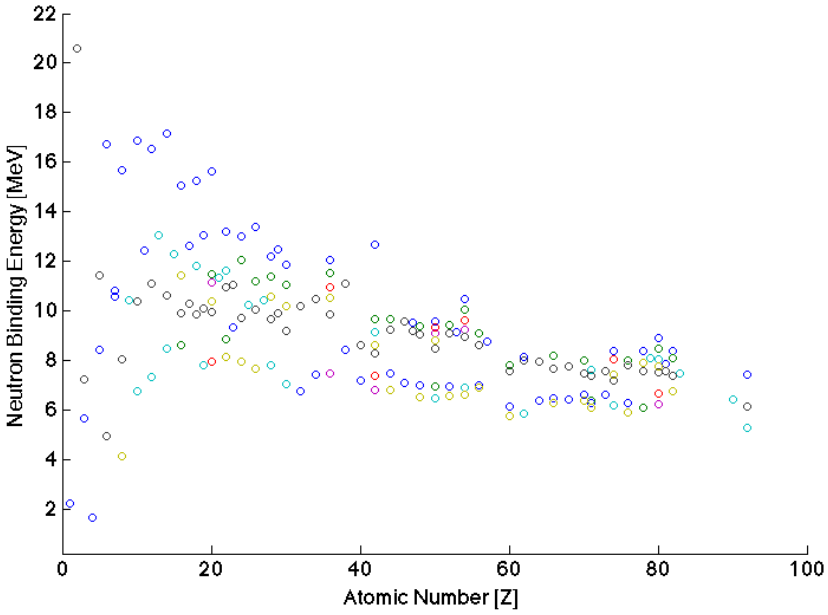

Figure 4.21: Minimum energy required to eject a neutron for a given stable isotope as a function of Z.

of the remaining energy from the inelastic collision since it is much lighter than the remaining nucleus. As such, the neutron is ejected in an anisotropic distribution following the direction of incident photon.

4.4.1 Energy Measurement

When a photon has enough energy to eject a neutron from the nucleus, the remaining energy is transferred to the nucleus and the exiting neutron. Since neutrons are a small fraction of the mass of a typical nucleus, most of the remaining energy (after overcoming the neutron binding energy) is given to the neutron by conservation of momentum. By measuring the neutron energy, the incident photon energy can be estimated knowing the binding energy for the reaction and the neutron/nucleus mass ratio. This extends the usefulness of the 511 keV signal from photoactivation, as neutron spectra can reveal higher peak energies.

For this experiment, the ASTRA-GEMINI laser generated a 1 GeV electron beam

with a broad spectra containing 300 pC of charge. The beam was passed through a 3 cm thick Pb converter before the electrons/positrons were separated by a spectrometer magnet. After 4.2 m, the remaining photons interacted with a $\varnothing 1.27\ cm \times 20\ cm$ long Al rod surrounded by a high-density polyethylene (HDPE) holder. Neutrons were detected by 3 sets of 6 energy-sensitive bubble detectors (see Section 2.6.5) with separate energy thresholds of 0.01, 0.1, 0.6, 1.0, 2.5, and 10.0 MeV. These were placed adjacent to the Al rod within the HDPE holder. Since the beam had greatly diverged after 4.2 m of propagation, the probability of the beam also interacting with the HDPE holder must be considered. The relative reaction probabilities between the Al and HDPE are shown in Figure 4.22, which indicates that the carbon in the HDPE can make a considerable number of neutrons at higher photon energies. However, because the (γ, n) energy threshold of Al is much lower and its cross-section is relatively higher, neutrons from carbon will not contribute as much to the high energy bins, adding signal to the lower energy bins. The normalized cross sections are shown in Figure 4.22. Assuming the neutrons are predominantly generated in Al due to its significantly higher cross-section probability, measured neutrons infer that the incident photon energy is at least 15 MeV greater than the resultant neutron energy.

After a shot series, the bubble detectors were removed and counted for the number of "bubbles" or expansions in the superheated emulsion caused by a capture of a neutron. The neutron spectra can be constructed by deconvolving the bubbles from detectors with different energy thresholds (see Section 2.6.5). However, for this case, we are primarily interested in only the high-energy portion of the spectra ($> 1\ MeV$) since the highest energy bins are more clearly resolved (the highest-energy signal is directly proportional to its neutron flux). There were three different conditions tested. First, for a background, we did not use a converter target (no bremsstrahlung) and deflected the electrons with a magnet. Next, we installed a 5 cm Pb converter to

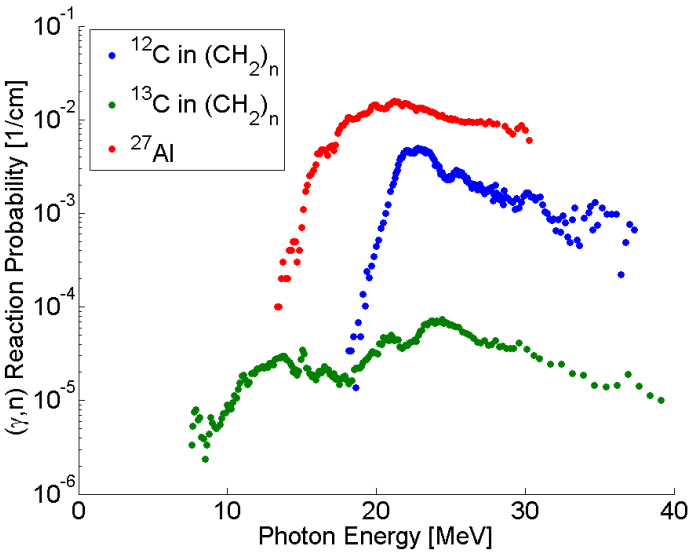

Figure 4.22: (γ, n) reaction probabilities per unit length based on cross-sections taken from EXFOR [cite EXFOR]. The carbon values are normalized to reflect abundance in high-density polyethylene (HDPE) with chemical formula $(CH_2)_n$.

generate bremsstrahlung photons but magnetically deflected the e^-/e^+. Finally, we removed both the converter and magnet to allow the electrons to propagate to the target and create bremsstrahlung closer to (or inside of) the detector. The average neutron fluence for each one of these cases is shown in Figure 4.23 after spectral deconvolution. It should be noted that the lower energy bins have consider error bars (the high-energy signal is subtracted from the low-energy signal).

For the case with only bremsstrahlung photons entering the detectors, we measured 5×10^6 $neutrons/shot$ above 2.5 MeV (corresponding to 18+ MeV $photons/shot$) and 5×10^5 $neutrons/shot$ above 10 MeV (corresponding to 25+ MeV $photons/shot$). Since the beam was only partially sampled due to the divergence and propagation distance, the actual number of neutrons is likely much higher.

4.4.2 Divergence Measurement

Due to conservation of momentum, the (γ, n) neutrons will receive a kick in the direction of the incident photon. This anisotropy results in an effective "beam" of

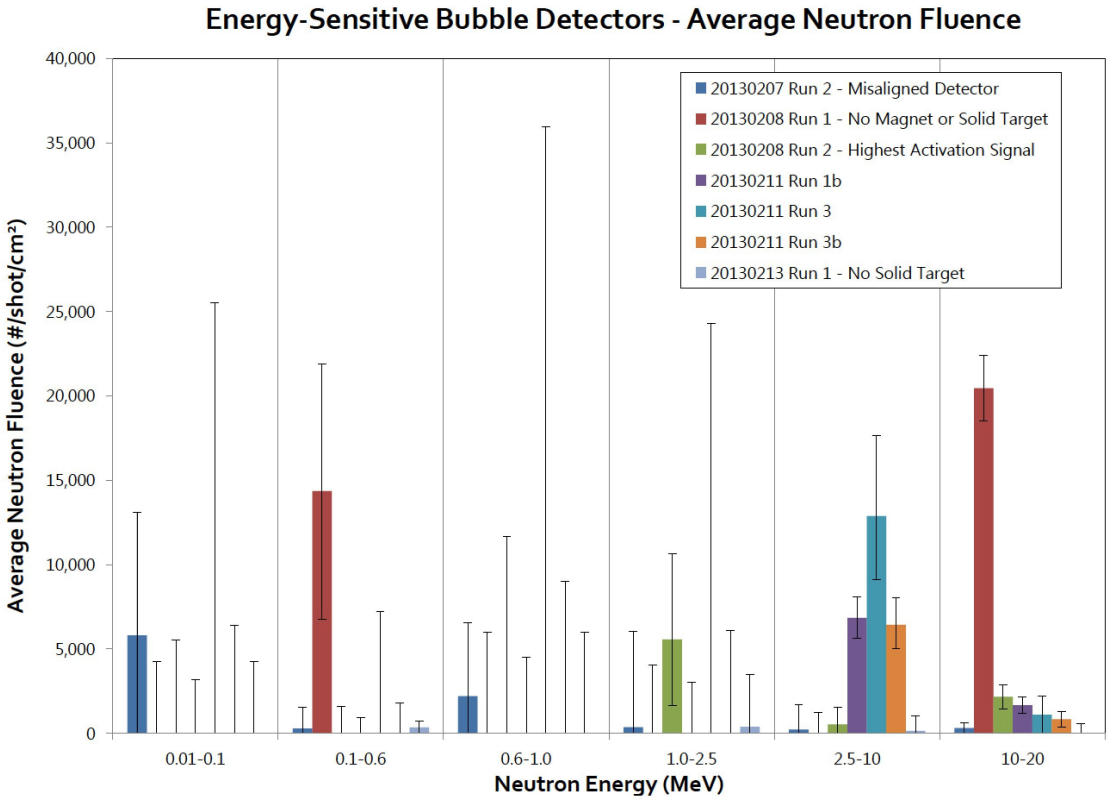

Figure 4.23: Average neutron fluence from energy-sensitive bubble detectors used on the pion detector at ASTRA-GEMINI. Neutron measurements from (light blue) background (no converter, spectrometer magnet installed), (purple, blue, orange) photon beam (5 *cm* Pb converter, spectrometer magnet installed), and (red) electron beam (no converter, no magnet). Note the large error bars for low energy neutrons due to the deconvolution.

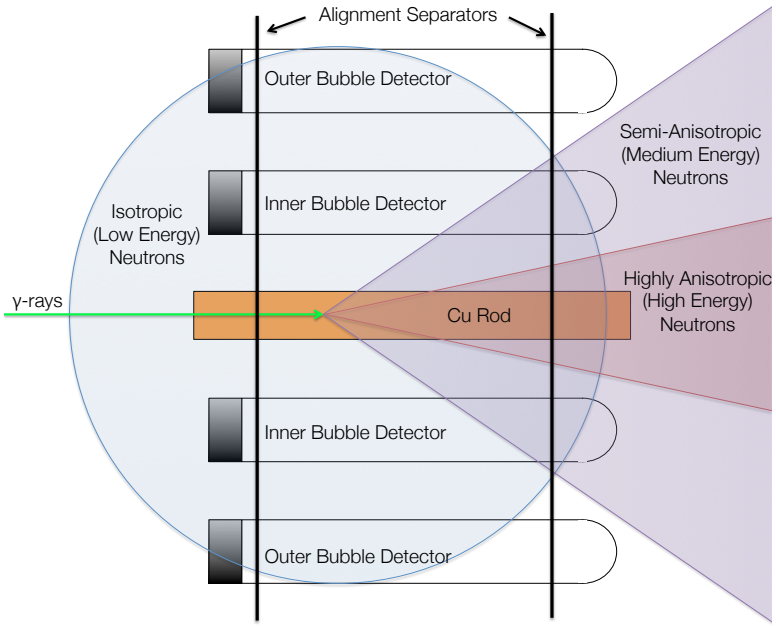

Figure 4.24: Diagram for measuring (γ, n) neutron divergence on ASTRA-GEMINI.

neutrons with a given divergence. To measure the divergence of (γ, n) neutrons generated with ASTRA-GEMINI, we arranged the energy-sensitive bubble detectors into an array parallel to a $\emptyset 12.7mm \times 100mm$ Cu rod placed on axis with the bremsstrahlung photon source. A 50 mm thick plastic wall surrounded the entire array to shield the bubble detectors from external or reflected neutrons.

In the array, the bubble detectors in the inner ring subtend 30° around the axis, while the outer ring subtends 15° (twice the distance to the axis). From this geometry, a purely isotropic source would distribute approximately twice the signal on the inner ring, whereas an anisotropic, beamed source would be contained in the inner ring alone, as shown in Figure 4.24. In terms of neutron energy, it follows that the higher energy would be more beamed due to the larger momentum transfer.

For this experiment, we used the 500 MeV, 50 pC electron beams from the NLTS experiment at ASTRA-GEMINI (described in Section 5.2) to generate bremsstrahlung photons after travelling through $\sim$ 15 of various low-Z materials (1 cm plastic, 4

cm Li, 10 cm Si). These photons then passed through the Ø12.7mm×100mm Cu rod at the center of the array to generate (γ, n) neutrons. After a series of 10-20 shots, the bubble detectors in the array were removed and counted. For the < 10 MeV neutrons, the ratio was approximately 4.75 inner/outer ratio, implying the beam was directional in a forward cone of roughly 80°. For > 10 MeV neutrons, the signal is entirely contained in the inner ring of detectors, placing the upper limit of the divergence at 32° based on the geometry. For one series in particular, this was evident as 1.7 $bubbles/shot$ (corresponding to 4.1×10^6 $neutrons/shot$ assuming 200 cm^2 area) between 10-20 MeV were counted in the inner ring, while none were seen on the outer track over 10 shots.

4.5 Other Particles

Although positrons are antimatter they are produced naturally via β^+ decay. Similarly, neutrons - which are naturally bound to the nucleus - can be ejected via nuclear fusion, spontaneous fission, etc. As such, both neutrons and positrons can be created with terrestrial, non-accelerator sources. However, "exotic" particles requiring more rest mass (> 100 MeV/c^2) than is typically available from natural radioactive processes (decay, fusion, fission) must be created using high-energy particles either from a cosmic source or an accelerator. Moreover, unlike the relatively stable half-lives of positrons ($> 10^{46}$ s) and neutrons (881 s), all of these higher-energy particles have half-lives of 2 μs or less, making synchronization crucial for potential applications and controlled measurement.

For the sake of conciseness, the only two particles discussed here are pions and muons since their low rest masses (140 MeV and 106 MeV, respectively) can be readily generated with HERCULES and ASTRA-GEMINI electron energies.

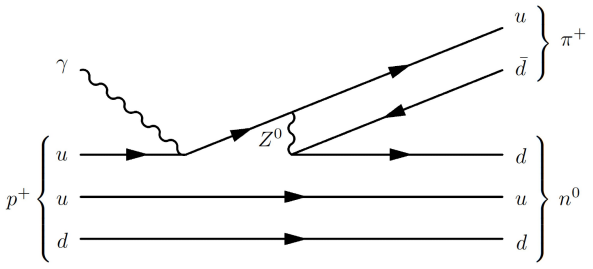

Figure 4.25: Feynman diagram of photoproduction of a π^+ via transformation of a proton within a nucleus. Note the creation of a $d\bar{d}$ quark pair which allows the d quark to supplant the u quark and form a neutron.

4.5.1 Pions

Pions are the lightest meson (a particle consisting of a quark and an antiquark) and are a key decay product in high-energy particle physics. Despite their larger rest mass than a muon, they require less energy to produce with bremsstrahlung since a (virtual) quark-antiquark pair ($> 10\ MeV$) in a nucleus is easier to produce than a muon-antimuon pair ($> 212\ MeV$). However, these quark-antiquark pairs must be created with enough energy to overcome the necessary binding energy of the quarks in neutron/proton with which it is interacting so that it can transfer quarks and form a pion (Figure 4.25). This process also leads to neutron/proton transformation inside the nucleus, which forms a different element than the original.

In certain cases, the new element is an radioactive isotope, which can be readily measured and identified *ex situ* with a HPGe detector. This is quite useful for the detection of pions since they are difficult to measure directly and have a extremely short life time ($\sim 26\ ns$) before preferentially ($> 99.98\%$) decaying into longer-lived (but just as difficult to directly detect) muons (Figure 4.26). However, due to the inherently low production cross-sections (10-100 μb) for pions, care must be taken to account for other primary and secondary processes such as (γ, n) and (n, p), which

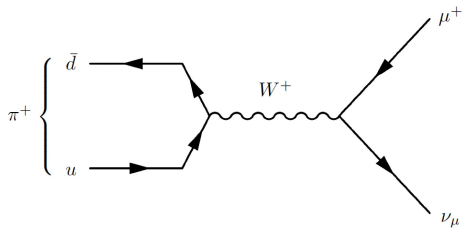

Figure 4.26: Feynman diagram of the decay of a π^+ into a μ^+ via the weak nuclear force with a 99.998% probability.

can result in the same isotope as (γ, π^+), but which have much higher cross sections. Increasing on the length of interaction can cause a significant production of the identifying isotope from secondary processes as the primary process yield increases. To minimize these secondary processes, previous experiments on pion production at sychrotron sources used a thin (100 μm) activation target. However, due to the much lower average flux on current LWFA compared to conventional accelerators, one must sacrifice accuracy for yield to get significant activation.

On the ASTRA-GEMINI experiment, we set out to detect π^+ via the $^{27}\mathrm{Al}(\gamma, \pi^+)^{27}\mathrm{Mg}$ reaction. In this case, the pion "detector" consisted simply of aluminum posts which were placed co-axially with the photon beam. The aluminum posts were built into a plastic block to moderate and attenuate external (γ, n) neutrons from the surrounding shielding and were straddled by energy-sensitive ($10\ keV - 20\ MeV$) neutron bubble detectors. The total length of the Ø12 mm rods was 200 mm, consisting of 4×50 mm rods so as to fit within the HPGe detector housing. At both ends of the plastic block, an imaging plate was mounted to the block to determine the alignment of the rods with respect to the incident photon beam (Figure 4.27). After a sequence of shots, the rods were analyzed in the HPGe detector.

For most runs, the bubble detector spectrum showed a suprathermal distribution above 1 MeV. This is likely due to the plastic shielding attenuating the low energy neutrons before they interact with a bubble detector (Section 4.4.1). The bubble

Figure 4.27: Photographs of the top and side of the pion detector setup used on the ASTRA-GEMINI experiment. The bulk of the bubble detector gel is inside the block and the rod is protected on the sides from contaminant (γ, n) neutrons.

detector spectral deconvolution typically yielded a flux of 1×10^4 $neutrons/cm^2/shot$ above 1 MeV with about a quarter of those above 10 MeV (Section 4.4.1). Given the total pion detector area of 500 cm^2, this gives roughly 5×10^6 $neutrons/shot$ above 1 MeV. Also, this does not take into account the number of (γ, n) neutrons from the surroundings of the pion detector.

Another method considered to measure the neutron flux inside the Al rod besides the bubble detectors was to measure the activation from the $^{27}\mathrm{Al}(\gamma, n)^{26}\mathrm{Al}$ reaction since ^{26}Al is a β^+ emitter with a half-life of 7.17×10^5 $years$. This technique gives a clearly identifiable 511 keV anniliation peak on the HPGe detector while measuring ^{27}Mg decay products. However, due to small contaminants in the Al (even on the order of parts per million) with shorter-lived half-lives (Zn, Cu, Fe, etc.), the origin of the 511 keV signal cannot be determined and this cannot be employed.

From a theoretical standpoint, given the bremsstrahlung photon spectrum from a 1 GeV, 300 pC flat-spectra electron beam interacting with 2 cm of Pb, the number of $^{27}\mathrm{Al}(\gamma, n)^{26}\mathrm{Al}$ activations would be 5×10^7 $neutrons/shot$ (Figure 4.28). However, this assumes primary interactions only with flat cross-sections from [97], neglecting any cascading effects which may be significant since the cross-section is peaked at

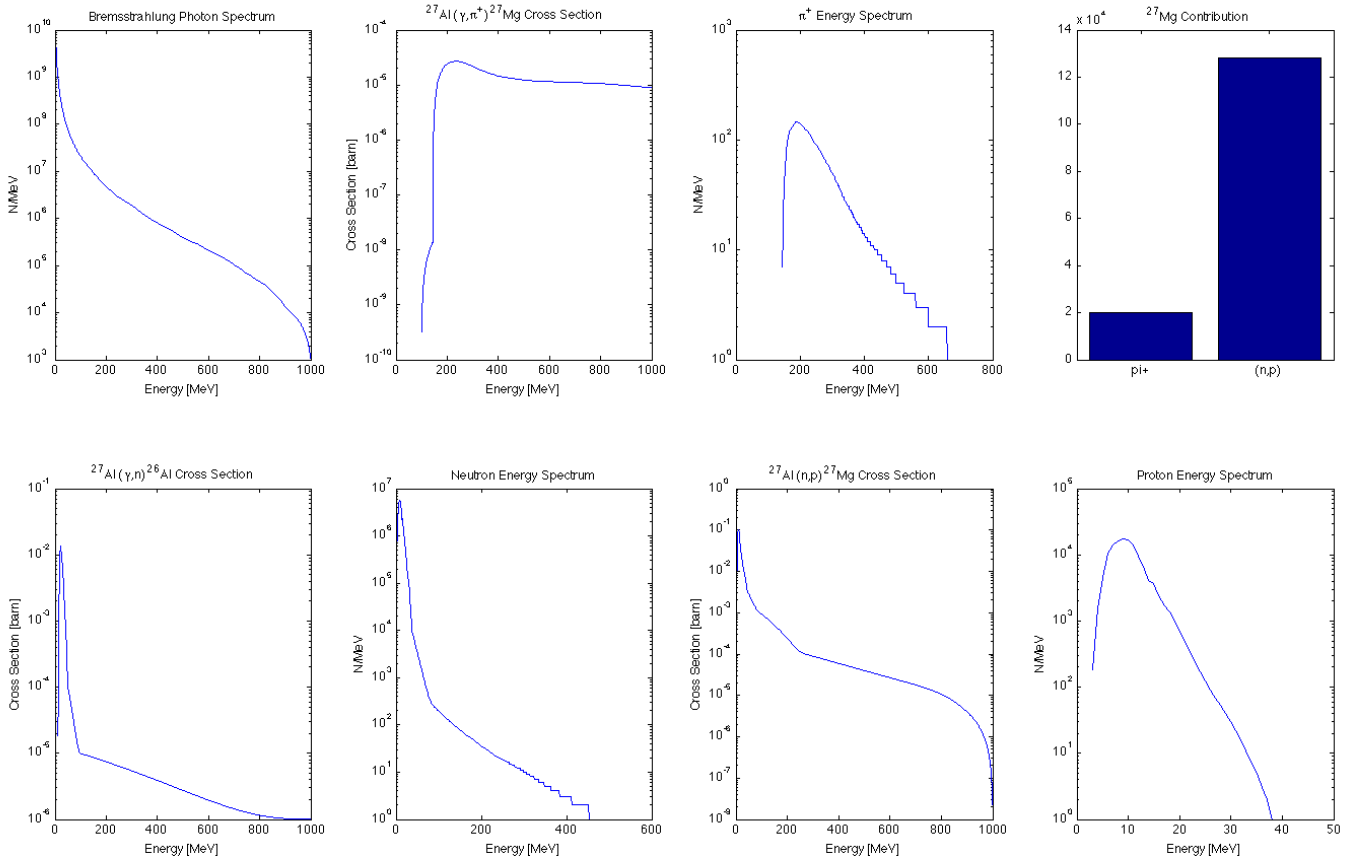

Figure 4.28: Comparison of the expected ^{27}Mg contributions from (γ, π^+) and $(\gamma, n) + (n, p)$ with ASTRA-GEMINI parameters.

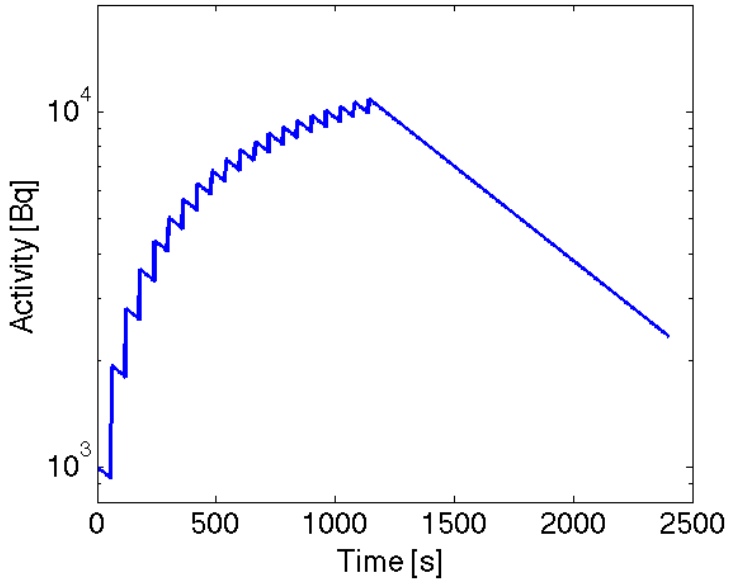

Figure 4.29: Calculated build-up and consequent decay of ^{27}Mg activity in a sample due to 1000 *activations/shot* over 20 *shots* at 1 *shot/minute*. Note that the sample was loaded into the HPGe detector approximately 15 *min* after the last shot, such that the integrated signal had significantly decayed to the activity level compared to only 3 *shots*.

lower photon energies.

Regardless, the number of neutrons does not bode well for the pion measurement, as we saw only 50 *counts* from 843 *keV* (the primary decay gamma of ^{27}Mg) and more than 84% of this is expected from (n, p) rather than (γ, π^+) based on the 1 *GeV* photon spectrum. Using the more realistic < 800 *MeV* photon spectrum skews this ratio even more in favor of (n, p) to 95%. Given the low level of ^{27}Mg, accurately determining the level of pion production with any statistical significance compared to (n, p) would require a detailed Monte-Carlo treatment with the full detector/shielding geometry, out of the scope of this thesis.

However, assuming each shot created the same number of activations, a simple rate equation model can be used to estimate the number of pions created per shot as shown in Figure 4.29. The measured activity is back-extrapolated knowing the amount of time that the sample decayed after the final shot (15 *min*) and the number of shots

taken over a given time (20 *shots* at 1 $shot/min$). Therefore, measuring 50 *counts* on the 10% inherently efficient HPGe detector collecting ∼50% of the total solid angle infers that 1000 $activations/shot$ were generated. Since 95% of these activations are from (n, p), the estimated pion number is 50 $pions/shot$.

4.5.2 Muons

The lightest and longest lived of these other particles is the muon. Although its mass is 106 MeV, it must be created in $\mu^+\mu^-$ pairs in order to conserve lepton number for a direct generation process (they are a key decay product of other, higher rest mass particles, such as $\pi^+/\pi^-, \tau^+/\tau^-$, etc.). Therefore, the required energy is 212 MeV, higher than for pions but still quite achievable with LWFA. Unlike the indirectly measured pions, however, muons must be directly measured since there are no transmuted source nuclei involved which can be distinctly measured. This makes the process of measuring muons quite difficult due to their low production with respect to electrons/protons and their intermediate mass, leading to low stopping power. This difficulty is observed with large particle collider detectors, where the outer detector shell is made primarily to track and absorb some of the muons' energy before they typically escape. One potential method of measurement is to use a Thomson parabola spectrometer, which separates particles with parallel electric and magnetic fields according to their charge-to-mass (q/m) ratio. Thomson parabola spectrometers are frequently employed in laser-solid experiments to measure ion spectrum and can be readily adapted for a muon detection experiment. Muons have a ratio of 106 MeV/e, whereas electrons are 0.511 MeV/e and protons are 938 MeV/e. This means that the parabolic trace of the μ^+ trace should be quite distinct from e^+ and p^+, whereas the μ^- trace should be distinct from e^- (antiprotons are too massive ($\sim GeV/c^2$) to be created with LWFA energies in this thesis).

Since muons have a long lived lifetime ($\sim$ 2.2 μs), an intermediate mass, and

are leptons, they have a variety of potential applications in particle physics, nuclear fusion, and active interrogation. Next generation particle colliders require leptons (fundamental particles including electrons, muons, taus and neutrinos) rather than hadrons (composite particles of quarks, such as protons, neutrons, pions, etc.) to determine finer aspects of the Higgs boson. To generate Higgs bosons with sufficent energies, linear accelerators (ILC, CLIC) would need to be on the order of 10s of km to meet the $\sim TeV$ energy requirement, costing on the order of \$10 *billion* US dollars. On the other hand, muons, which are $200\times$ heavier than electrons, can be accelerated in current circular accelerators since bremsstrahlung loses scale as m^{-4}, meaning that a muon loses 10^9 less energy to bremsstrahlung than electrons/positrons. Although muons are most routinely produced from proton-produced pions which quickly decay, the primary issue with muon colliders is the issue of muon cooling, which is required to re-collimate and bunch the exiting muons into a usable beam. This process is studied on larger accelerator facilities, but LWFA potentially allows for more compact experiments to study muon cooling [98].

One speculative use of muons is in nuclear fusion. Since a μ^- is a lepton with the same charge as an e^-, it can form exotic atoms (specifically termed a *muonic atom*) with nuclei during its short lifetime. Due to the much higher mass of the muon, the atomic radius of *muonic atom* is significantly reduced, lowering the Coulomb barrier required for another nuclei to fuse with the nuclei of the *muonic atom*. The μ^- is typically ejected and can go on to fuse multiple nuclei before it decays or becomes attached to a fusion product (α-particles for D-T reaction or ^{3}He or ^{3}T nuclei for D-D reaction). This process is known as muon-catalyzed fusion (termed μCF) and was reseached extensively in the 1980s. However, the required accelerator technology available at the time limited the ability to easily intoduce muons in large fusion experiments and test *in-situ* in hybrid schemes. With the upcoming NIF-ARC beamline, it is conceivable that LWFA could be implemented to generate a muon

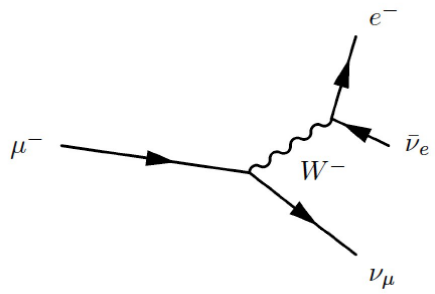

Figure 4.30: Feynmann diagram of the decay of a μ^- into a e^- and appropriate neutrinos via the weak nuclear force.

source for a hybrid ICF-μCF approach or as a muon backlighter of the fuel assembly.

Lastly, muons, with their low stopping power in materials, are potentially useful for active interrogation of special nuclear materials (SNMs). This method is currently employed using cosmic-ray generated muons to interrograte shipping containers and other structures. However, the ability to use a compact, pulsed source of muons could lead to other interrogation applications which may require the detector to be placed parallel to the ground rather than the perpendicular case for using cosmic ray sources.

Since the charged pions preferentially decay into a muon of the same charge for 99.998% of transactions (Figure 4.26), the detection of charged pions (Section 4.5.1) is a effective measurement of muons. Therefore, for nearly every measured pion, there is a muon produced. From the pion measurements in the previous section, the number of muons per shot in ASTRA-GEMINI could be inferred to be 50 $muons/shot$.

Another indirect measurement of muons could be based on their long-lived ($2.2\mu s$) decay into electrons (Figure 4.30). Since most electrons and photons are absorbed or scattered away within $\sim 100\ ns$ of the bremsstrahlung generation process, the slower muons will likely survive and decay afterwards, having not escaped the generation area. This implies that a gated scintillator could be used to observe the decaying muons.

4.6 Conclusions

An extensive collection of bremsstrahlung and secondary particle generation data has been presented using LWFA electrons as the driver. Although many of these results have been previously demonstrated on conventional RF accerators, there are a number of firsts using LWFA shown in this chapter: the first measured few-second radioisotopes using LWFA, the largest photo-fission yields of ^{238}U per unit of laser energy, the first high-energy ($> 100\ MeV$) laser-produced positrons, the first directional neutron source using LWFA, and the first measured production of pions (and inferred muons) using lasers. These results demonstrate the upcoming capabilities of LWFA sources compared to mature RF technology.

CHAPTER V

Non-Linear Thomson Scattering

5.1 Introduction

The culmination of the research presented in this thesis is the experimental work towards non-linear Thomson scattering (NLTS) using LWFA. The research in Chapter III provided a good understanding of pump-probe experiments with LWFA, whereas the research in Chapter IV provided a suite of diagnostics necessary to measure the high-energy photons generated by NLTS.

Experimentally realizing NLTS is not trivial, requiring both a ultra-relativistic, high-energy electron beam *and* a high-intensity laser system [99, 100, 101]. The E144 experiment in the mid-1990s [102, 103, 104] used the 46 GeV electrons from the 2 km SLAC accelerator but were limited by linear ($a_0 \ll 1$) laser scattering pulses available. In the time since E144, all-optical schemes of LTS for compact sources of tunable high-energy photon beams have become a growing interest[105, 106, 107]. The first demonstration of LTS with LWFA used a plasma mirror to back-reflect the LWFA laser pulse ($a_0 \approx 1$) back onto the electron bunch [108]. This technique avoids much of the hassle of spatio-temporal alignment since the laser is co-propagating with the electrons, but the plasma mirror introduces bremsstrahlung as a considerable fraction of the signal. Another experiment used a small portion of the LWFA beam focused with a long-focal length lens to scatter off an electron beam to generate $\sim MeV$

photons with $a_0 < 1$ [109, 110]. Both of these LWFA results use broad electron energies such that the consequent photon spectrum is also broad. Most importantly, all of these experiments did not enter the non-linear scattering regime, falling short of demonstrating any nQED effects [111, 112, 113].

This chapter will summarize the two experimental attempts at NLTS using the HERCULES and ASTRA-GEMINI lasers, the preliminary results, and simulations of the interaction probability.

5.2 Experimental Attempts

To achieve NLTS, both a high energy electron beam (200 MeV) from LWFA and a second high-intensity laser pulse ($a_0 \gg 1$) are required, demanding a 100 TW-class laser system. As such, experimental campaigns were designed for the HERCULES and ASTRA-GEMINI systems and are detailed in this section.

5.2.1 HERCULES Experiment

For the HERCULES NLTS experiment, the compressed beam was split with a thin beamsplitter (to minimize B-integral) into two arms: the transmitted beam to drive electron beams via LWFA, and the reflected for scattering off the electrons (Figure 5.1). The LWFA pulses contained 50 TW and were focused via $f/20$ optics to an $a_0 \simeq 3$ above a 3 mm long gas jet, generating $\sim 10^8$ electrons at ~ 200 MeV energy. The second scattering pulse contains 140 TW and was focused via $f/2$ optics to a peak $a_0 \simeq 10$ near the exit of the gas jet. The $f/2$ optic had an $f/15$ hole for the $f/20$ (and electron beam) to pass through in a counterpropagating geometry (180°). The two focusing axes were spatially overlapped prior to - and checked in between - laser shots to within ~ 12 μm accuracy using optical scattering off a 80 $lines/mm$ mesh. Relative timing between the arms was found within ~ 100 fs via optical breakdown as described in Section 2.5.2.

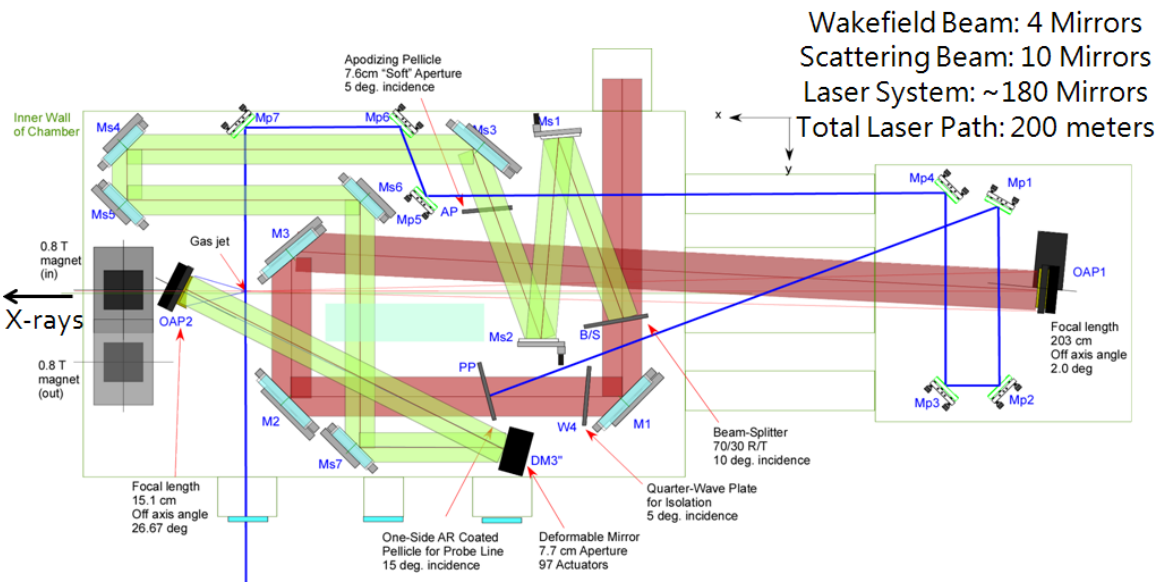

Figure 5.1: Optical layout of the NLTS experiment on HERCULES.

The primary detector was a Compton scattering photon spectrometer, as described in Section 4.2.1. However, since this style of detector requires a large flux of photons to make up for the conversion losses to electrons, and has a slow readout (approximately ~ 30 *min* cycle time required to vent chamber, read & replace IP, and check alignment), it set a mimimum threshold of detection and limited the experimental parameter space to scan.

The laser pointing fluctuation on HERCULES was ~ 5 μrad with the local air conditioning turned off and ~ 15 μrad with the air conditioning turned on. During experiments, the air conditioning was cycled to minimize vibrations during shots.

For other gas jet experiments, the LWFA beam was typically focused 1 *mm* above the nozzle. However, to prevent the counterpropagating $f/2$ from grazing and damaging the nozzle, the height above the nozzle was adjusted to 2.5 *mm*. At this height, the transverse gradients of the gas flow were more exaggerated, leading the laser to "skip" off the gradient and direct the electrons away from the nozzle. Consequently, the electron beam pointing was constantly measured and found to be deflected $5-10$ *mrad* up vertically. The alignment of the Compton scattering spectrometer and $f/2$

focus were adjusted accordingly. However, the electron spectra showed that the beam frequently clipped on the hole of the $f/2$ OAP, creating on-axis bremsstrahlung that generated a background signal on the Compton spectrometer. Unfortunately, this signal was higher than any seen from two-beam overlap.

After this HERCULES attempt, a set of simulations (shown in Section 5.3) were performed to identify potential improvements to the experiment. These simulations showed that electron beam stability and detector dynamic range needed to be improved, leading to the development of gas cells (Section 2.4.2) and robust, single-shot detectors (Section 4.2). These improvements were applied to the subsequent ASTRA-GEMINI attempt, detailed in the next section.

5.2.2 ASTRA-GEMINI Experiment

For the ASTRA-GEMINI NLTS experiment, the South beam ($f/20$ OAP) was used to drive electron beams via LWFA, and the North beam ($f/2$ OAP) was used for scattering off the electrons. The geometry of focusing was nearly identical to that used on 2.3 in the previous section, with the overall layout shown in Figure 5.2. The LWFA pulses contained 250 TW and were focused via $f/20$ optics to an $a_0 \simeq 5$ into a $1 + 18$ mm gas cell, generating $\sim 3 \times 10^8$ electrons at ~ 500 MeV energy. The second scattering pulse contains 250 TW and was focused via $f/2$ optics to a peak $a_0 \simeq 20$ near the exit of the gas cell. The $f/2$ optic had an $f/17$ hole for the $f/20$ (and electron beam) to pass through in a counterpropagating geometry (180°). The two focusing axes were spatially overlapped prior to - and checked in between - laser shots to within ~ 10 μm accuracy using optical backlighting of a 25 μm wire. Relative timing between the arms was found within ~ 200 fs via spectral interferometry as described in Section 2.5.2.

Again, the primary detector was a Compton scattering photon spectrometer, as described in Section 4.2.1. However, a variety of other shot-to-shot diagnostics were

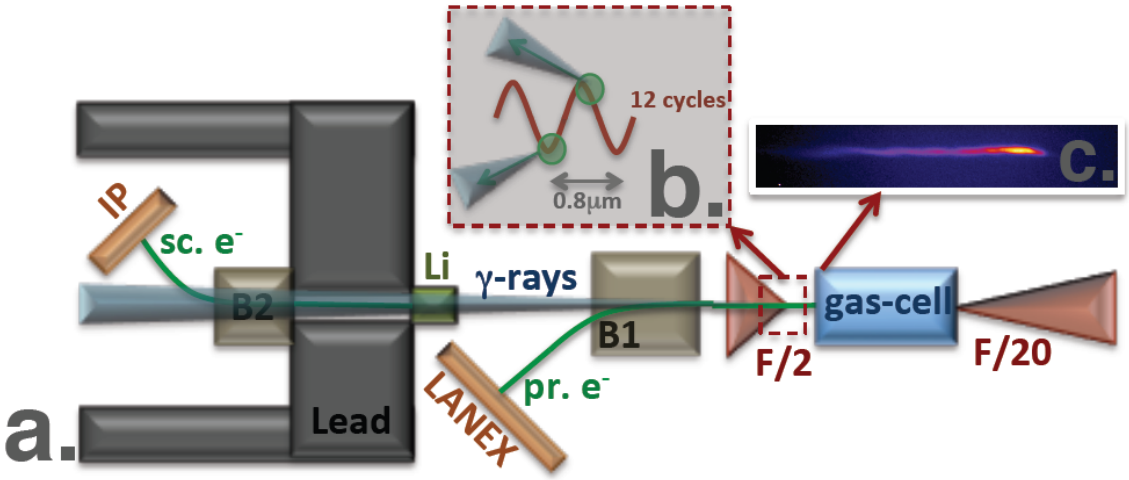

Figure 5.2: (a) Optical layout of the NLTS experiment on ASTRA-GEMINI. (b) The $f/2$ laser focus represented as a wiggler of 12 cycles with $\lambda_u = \lambda_L/2 = 400\ nm$. (c) Typical electron spectrum generated by the $f/20$ passing through the $1+18\ mm$ gas cell.

used, including: the pixellated scintillator array, the prompt β^+ activation detector, and a gated Cherenkov detector.

Over the course of the experiment, the electron spectrometer showed large betatron and pointing oscillations in the electron beam, which was speculated to be due to the focal spot asymmetry (shown in Figure 2.6). As such, an apodizer was installed in the South beam after amplification to reduce the beam to effectively $f/27$, thereby improving the focal symmetry and consequently the pointing stability.

To improve the chances of spatial overlap, an optional diffuser was placed in the North beam before it went to the $f/2$. This reduced the peak a_0 from 20 to 10 around the focal spot of Ø5 μm, but added a larger plateau of Ø100 μm diameter with $a_0 \geq 1$ and Ø50 μm diameter with $a_0 \geq 2$.

Despite the limited experimental time available, a large parameter space covering $200 \times 200 \times 400\ \mu m^3$ of overlap volume (vertical, horizontal, and time dimensions, respectively) was explored by tiliting the $f/2$ and varying a delay stage. Although the data from the shot-to-shot diagnostics were inconclusive, the Compton spectrometer

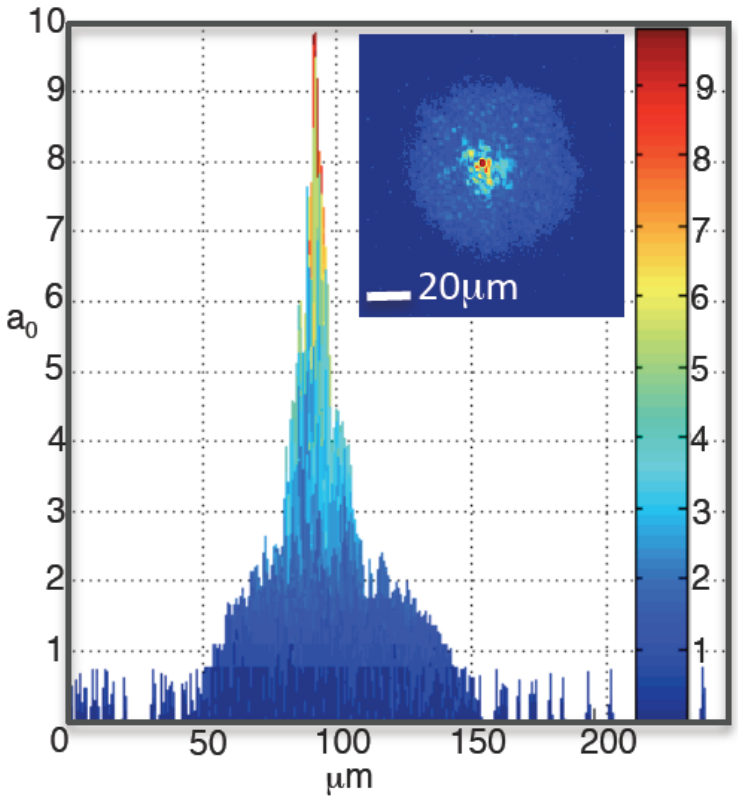

Figure 5.3: a_0 lineout of the $f/2$ focal spot (inset) on ASTRA-GEMINI with the diffuser installed. Note the Ø100 μm diameter plateau of $a_0 \geq 1$ and Ø50 μm diameter plateau of $a_0 \geq 2$.

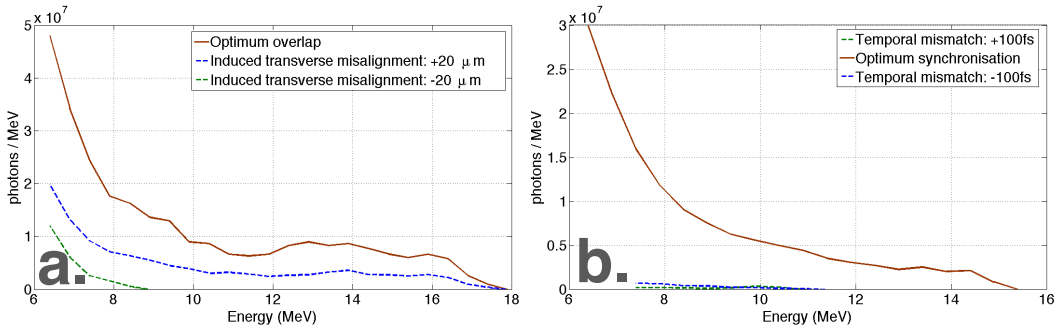

Figure 5.4: Compton scattering spectrometer data showing spatial (a) and temporal (b) misalignment effects on the photon spectra and flux. Reproduced courtesy of Gianluca Sarri.

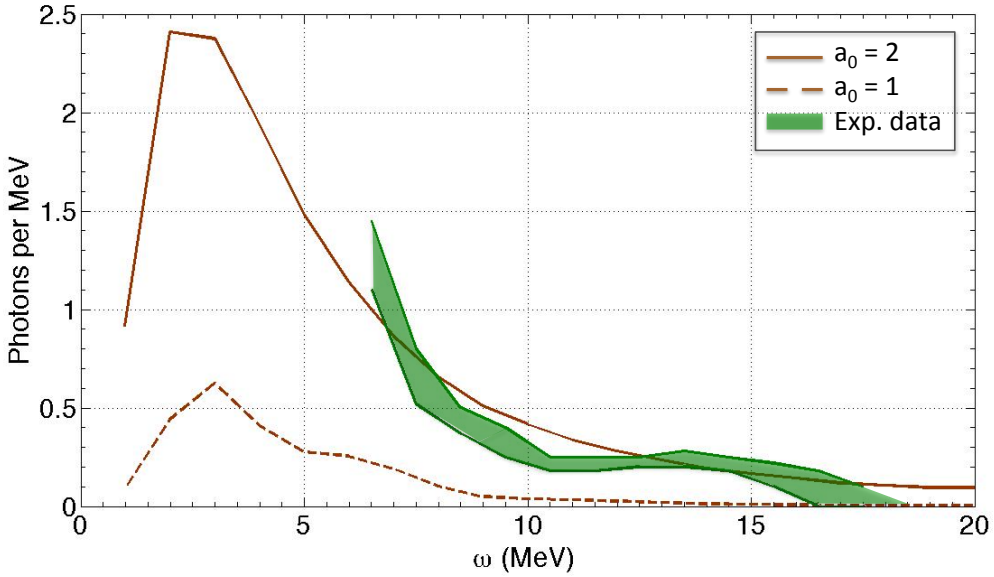

Figure 5.5: Compton scattering spectrometer data showing simulated photon spectra for overlap with $a_0 = 2$ (line) and $a_0 = 1$ (dashed), and extracted experimental data (green shaded region). Reproduced courtesy of Gianluca Sarri.

signal was found to have spatial (Figure 5.4(a)) and temporal (Figure 5.4(b)) dependance. With more detailed analysis/modeling which factors in the electron beam energy and photon conversion efficiency, the spectral shape was observed to follow a non-linear generation mechanism ($a_0 > 1$) as shown in Figure 5.5. Due to the electron energies involved ($E_{e^-} \leq 500\ MeV$), a linear $4\gamma^2$ upshift would only yield a 6 MeV photon, implying either that the measured photons above 6 MeV came from either bremsstrahlung or a non-linear process. In this case, bremsstrahlung can be systematically ruled out by varying the spatial/temporal overlap, leaving NLTS as the most likely cause.

5.3 Monte-Carlo Simulation of Beam Overlap

Unfortunately, due to pointing fluctuations from vibrations, temperature gradients, beam instabilites, etc., the overlap probability can be significantly decreased, causing the resulting photon yield to drop. To study these effects, a MATLAB code

that uses Monte Carlo methods was developed to simulate the effects of optical support vibrations and air currents perturbations and compute the consequences in terms of photon yield. We then used this code to study the influence of several parameters in the experiment, such as spatial separation and timing difference between the two beams.

Several pertubations to the laser path can cause a beam deflection (Fig. 2.11). A gradient of pressure, temperature or humidity can create a refractive index gradient that deflects light. Mirrors held by springs can relax over time and cause the beam to drift. Vibrations around the lab can cause the optical tables to oscillate, moving the mirrors and deflecting the beams. There are 180 mirrors in the HERCULES laser, and the optical path is 200 m long, so this even a small movement in a single mirror can have a large effect. Finally, laser-plasma instabilities can cause the direction of the electron beam to deviate from the initial laser axis on a shot-to-shot basis.

5.3.1 Perturbation Scan

Figure 5.6 shows the variation of the photon yield with the air current perturbations and the vibrations, computed by direct product of the laser and electron beams distribution (red) and Monte Carlo (blue). The error bars correspond to error estimates with 95% confidence, that is, $2\sigma/\sqrt{N}$, where σ is the standard deviation of the results and N the number of samples. Full numerical results (number of photons and error estimates) are shown in Appendix B. As expected, the perturbations increase the deviation of the beams, causing the number of photons to decrease.

5.3.2 Spatial-Temporal Separation Scan

Figure 5.7 shows the effect of a separation between the beams in the presence of vibrations. The separation is the distance over which the electron beam diverges before being hit by the focused laser. No separation means that the laser focus hits

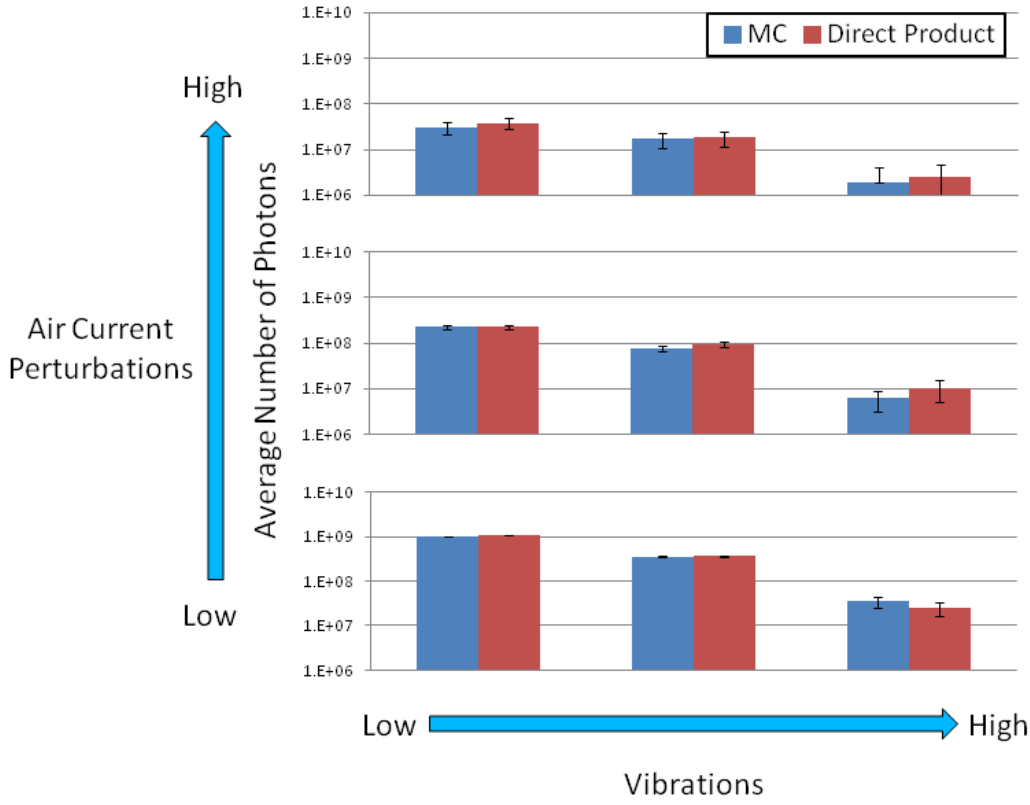

Figure 5.6: Influence of vibration and air gradient strengths on photon yield.

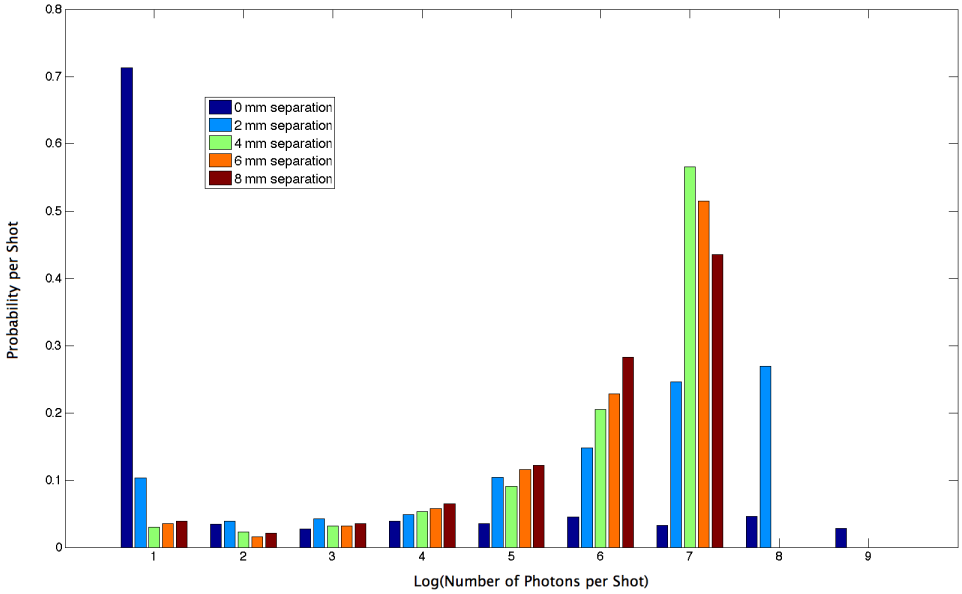

Figure 5.7: Photon yield probability as a function of electron beam and laser focus separation. (Dictated by the electron beam size at overlap)

the electron beam at the point were it is the most concentrated. We can see that with no separation at all, most shots give a very small number of photons, because the beams rarely overlap. When they do overlap, they produce the maximum amount of signal due to the concentrated electron beam. Separation increases the probability that the beams overlap and produce photons, but the average yield is reduced as the electron beam diverges.

Figure 5.8 shows the effect of changes in the laser timing. This is similar to the previous section, except that in this case, the laser is diverging, not the electron beam. The effect is quite similar: the probabilities of very small yields and very high yield are reduced, while the probability of getting an intermediate photon yield is increased.

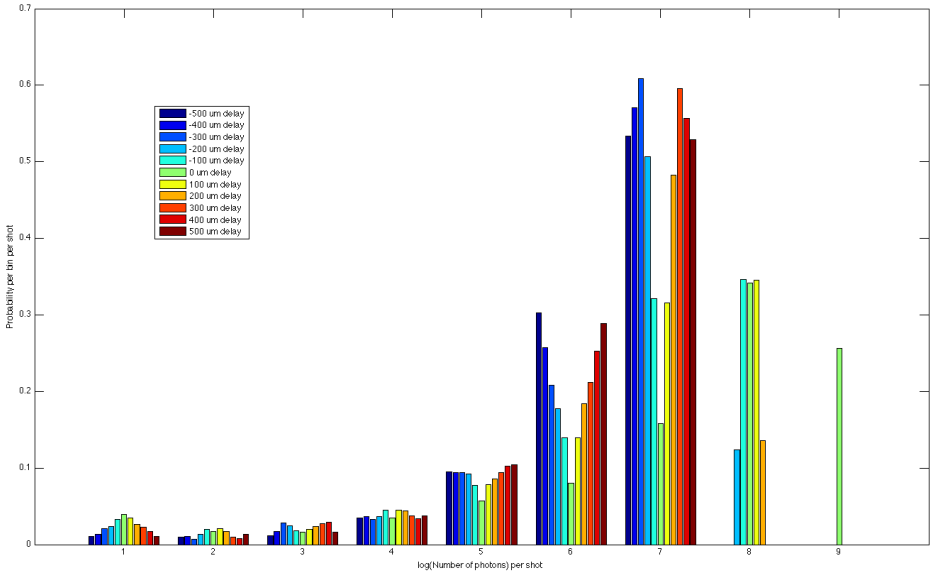

Figure 5.8: Photon yield probability as a function of overlap timing. (Dictated by the laser intensity at overlap)

5.3.3 Electron Beam Pointing Scan

Figure 5.9 shows the effect of an additional pointing instability in the electron beam. We previously assumed that the deflection of the electron beam is just 10 times that of the laser beam, but in fact there can be a significant fluctuation around that position. That was simulated with a normally distributed random variable around the initial laser pointing direction. Increasing the electron beam pointing instability only slightly reduces the photon yield since the electron beam divergence is similar to the additional fluctation even with an extra 12 $mrad$ pointing instability.

Figure 5.10 shows the effect of offset between the two beams. We previously assumed that the beams have the same axis which they are normally distributed around. Introducing even a slight offset ($\sim$ 50 μm) between the beam axes reduces the photon yield and detection probability considerably. This is most likely the case in the HERCULES experiment since the overlap diagnostic is only accurate to $\sim$ 12 μm and the beam drifts in between alignment and shots.

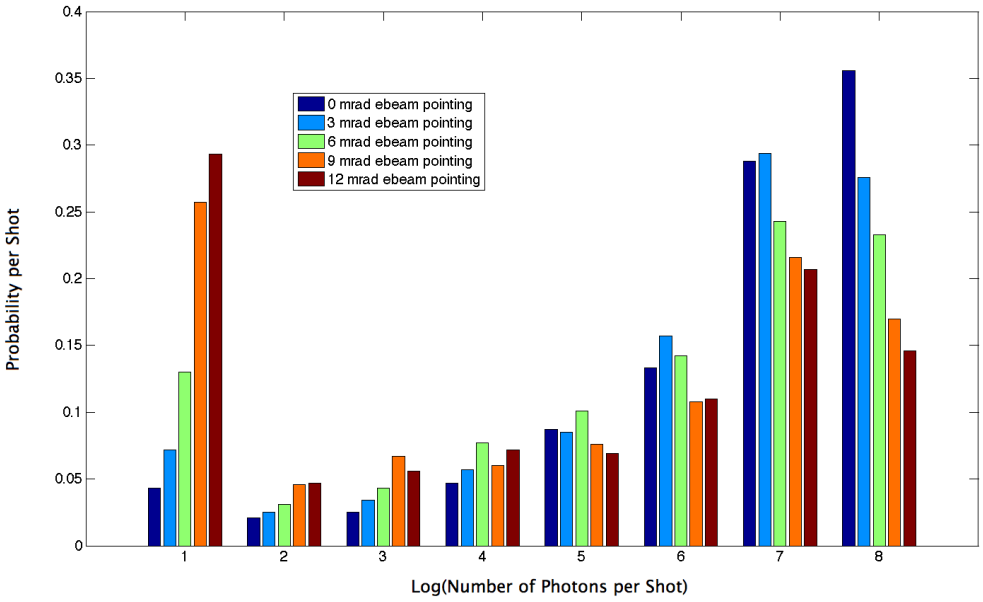

Figure 5.9: Photon yield probability as a function of additional electron beam pointing instability.

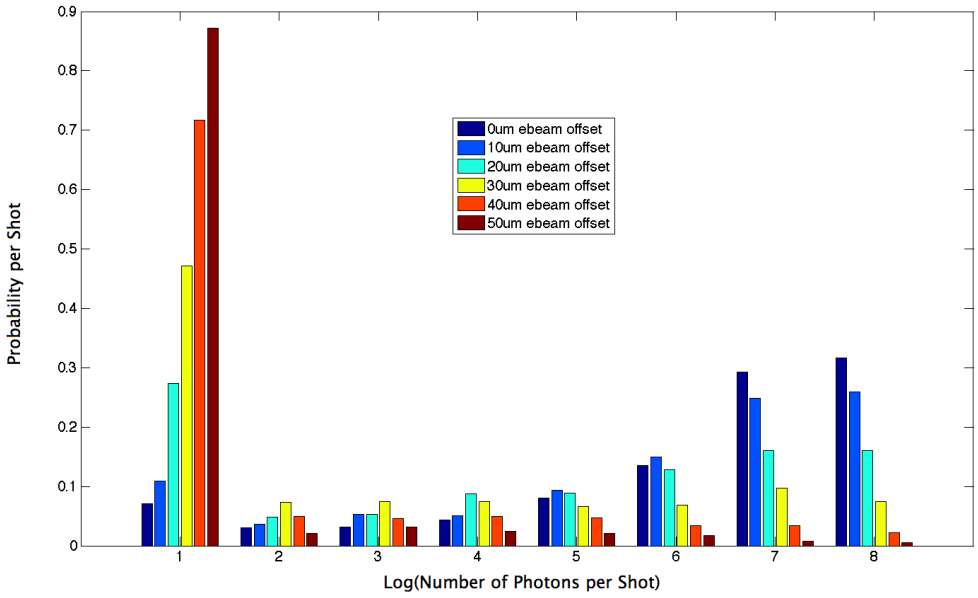

Figure 5.10: Photon yield probability as a function of axis offset.

5.3.4 Code Summary

As expected, the code showed that increased air currents perturbations and vibrations reduce the photon yield. Although the constants and distributions used for these perturbations were based on basic assumptions, the code was able to re-create pointing fluctuations similar to those observed experimentally. More detailed knowledge of the parameters of the experiment and implemention in the code would allow a more precise computation of the fluctuations and their effect on the experiment.

The code was used to study the influence of several parameters in presence of perturbations. It was shown that a greater seperation between the laser focus and electron beam source decreases the average photon yield but increases the probability that the beams actually overlap. A variation in the laser timing has a similar effect. Additional electron beam pointing marginally decreases the yield, whereas offseting the electron beam greatly decreases the photon yield.

In particular, minimizing the electron beam offset and detection threshold were investigated for the subsequent round of NLTS experiments at ASTRA-GEMINI (Section 5.2.2).

5.4 Conclusions

After two experimental attempts using the HERCULES and ASTRA-GEMINI lasers, much work still needs to be done to conclusively demonstrate NLTS. These two experiments, as well as the Monte-Carlo simulations, have helped identify many areas of improvement for future experiments.

CHAPTER VI

Conclusions

6.1 Summary

This thesis presents experimental data generated using laser wakefield accelerators to pump or probe a secondary process. The intial set of experiments demonstrated the first sub-*ps* measurements of the evolution of magnetic fields in laser-plasma interactions using LWFA generated electron beams [114]. We observed an expansion of the magnetic field along the surface at nearly the speed of light to $\sim mm$ in diameter, inferring that the laser-produced hot electrons that emanate along the surface generate the field, measured on the order of 10^4 T. As the laser contrast is reduced, the ratio of field strength on the front and rear of the target will dynamically shift to being dominated by the rear surface fields as the front surface pre-plasma cancels the field from expanding due to available return current, whereas the front surface dominates for high-contrast interactions.

The second group of experiments investigated bremsstrahlung generation using LWFA electron beams for diagnostic development, nuclear reactions, and secondary particle generation. We measured the bremsstrahlung beam flux to contain upwards of 10^{10} $photons$ with $> MeV$ energies using a single-shot Compton-scattering spectrometer and (γ, n) activation/autoradiography techniques. With these photons, we measured the largest photofission yield, $\sim 10^7$ $fissions/J$, of depleted uranium per

unit of energy using lasers. Furthermore, the shortest-lived ($t_{1/2} < 5\ s$) radioisotopes generated with lasers were measured using these photons to activate silicon and glass (SiO_2) targets [115]. Coupled with spatial measurements of the beam using a pixellated BGO scintillator and autoradiography of carbon and copper activation targets, the brightness of the LWFA bremsstrahlung source is on the order of 10^{19} $photons/s/mm^2/mrad^2/0.1\%BW$ at 10 MeV, based on measurements of 10^8 $photons$ at 10 MeV with 10 $mrad$ divergence and assuming 100 fs duration and 0.01 mm^2 area.

In addition to the photons beams, secondary particles were measured, including the first highly-relativistic positron beams [116, 117, 118], directional neutrons, and pions generated using LWFA electron beams. By increasing the converter target thickness and Z, the number of positrons was observed to increase to a maximum at a thickness of $2L_{rad}$, consistent with the Bethe-Heitler process of electrons converting into photons which consequently produce e^-/e^+ pairs. Increasing the converter thickness to $5L_{rad}$, the incident electron beam almost entirely depletes into photons and e^-/e^+ pairs such that the resultant electron/positron beam is neutral and highly relativistic, having a density of $n_{e^-/e^+} \approx 10^{15}\ cm^{-3}$ in the beam frame of reference. Besides measuring the radioisotopes resulting from (γ, n) reactions, the spatial and spectral distributions of (γ, n) neutrons were also measured with bubble detectors, with 10^5 $neutrons/J$ above 10 MeV contained in a 32° cone. Lastly, for high-energy electron energies ($> 230\ MeV$), a small number (50 ± 30) of pions were measured indirectly using (γ, π^+) activation of aluminum.

The final set of experiments explored using LWFA electrons interacted with ultra-high-intensity laser pulses ($a_0 \gg 1$) to perform non-linear Thomson scattering. By scattering a laser pulse of $a_0 \simeq 2$ off electrons of 500 MeV energy, photons above 15 MeV were generated and measured with the aforementioned Compton scattering diagnostic. The beam had a brightness of 10^{21} $photons/s/mm^2/mrad^2/0.1\%\,BW$ at

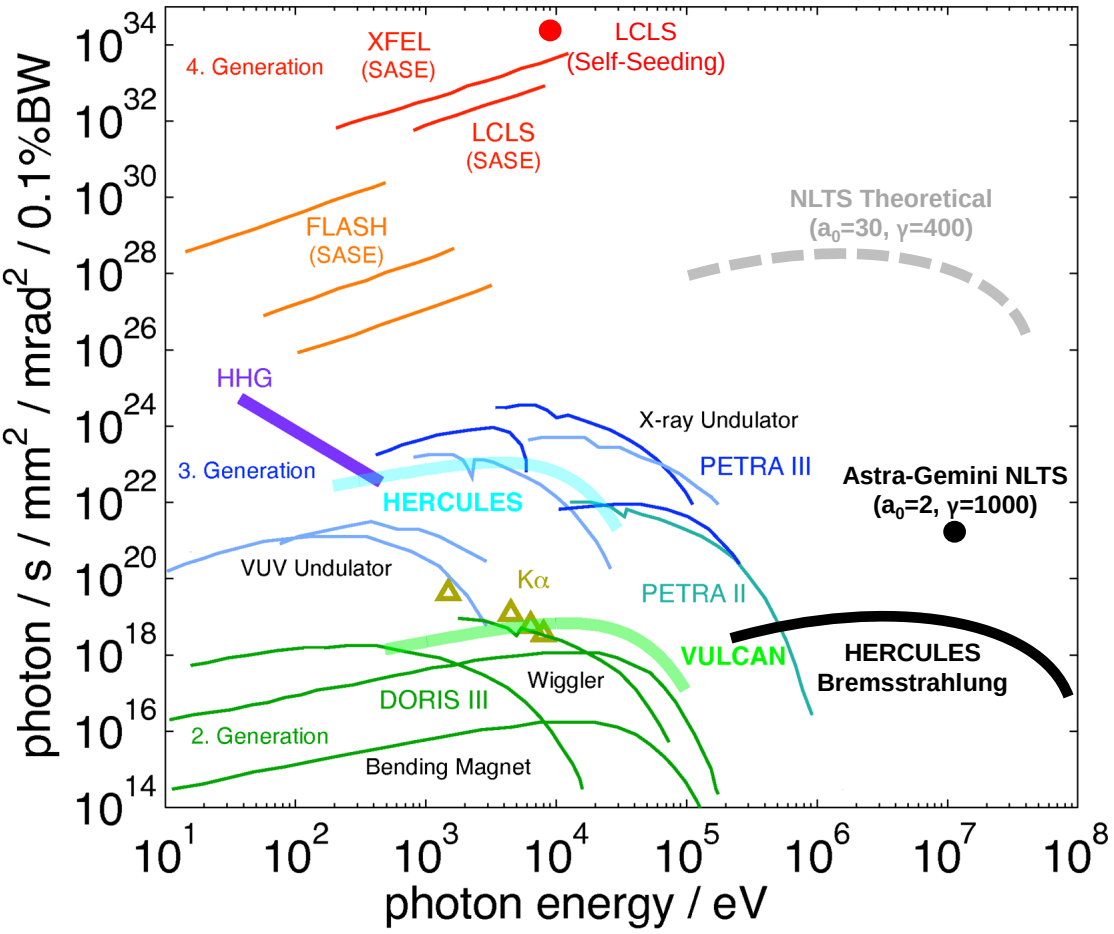

Figure 6.1: Peak brightnesses of various light sources. Work presented in this thesis is shaded black. Previous betatron measurements from HERCULES are shaded light blue. Theoretical NLTS estimates for HERCULES-like parameters are shaded grey. Reproduced courtesy of Stefan Kneip.

10 MeV, based on measurements of 10^8 *photons* at 10 MeV with 2 $mrad$ divergence and assuming 40 fs duration and 30 μm diameter. When the spatial or temporal alignment was changed by 30 μm or 100 fs, the signal dropped off above 10 MeV, indicating that the process was indeed non-linear in nature.

6.2 Challenges

To improve most LWFA probing experiments in this thesis, the electron beam can be made significantly more mono-energetic using controlled injection [119], thereby decreasing both its temporal and spectral distribution. This typically comes at the cost of increased complexity (using staging or second laser) and lowered beam charge. For LWFA pumping applications, more charge is typically required to increase efficiency. For example, the activation experiments require only moderate electron energies (5-25 MeV) since most reactions and do not benefit much from the higher energy electrons. As such, continuous ionization injection could be used to generate broad energy electrons throughout the acceleration process, maximizing available charge. Another possibility would be to split the pulse into a pulse train or use higher-repetition rate lasers in higher density plasma to generate more electrons with lower energies.

As indicated in Section 5.3, the electron beam shot-to-shot pointing stability is particularly critical for the realization of NLTS. The development of staged gas cells (Section 2.4.2) has improved the pointing, but has introduced its own challenges in terms of balancing the density in the separate stages. Another difficulty for NLTS is shot-to-shot detection of the photon beam, through which some of the work presented in this thesis was motivated. Although bremsstrahlung can be used to characterize these diagnostics, the photon flux from NLTS can be lower than from bremsstrahlung, making diagnostics difficult to implement even though the peak brightness of a NLTS source could be orders of magnitude higher than bremsstrahlung.

6.3 Future Work

While LWFA has become a very successful technique for accelerating electrons to multi-GeV energies since first demonstrated 10 years ago [10, 11, 12], its distinct

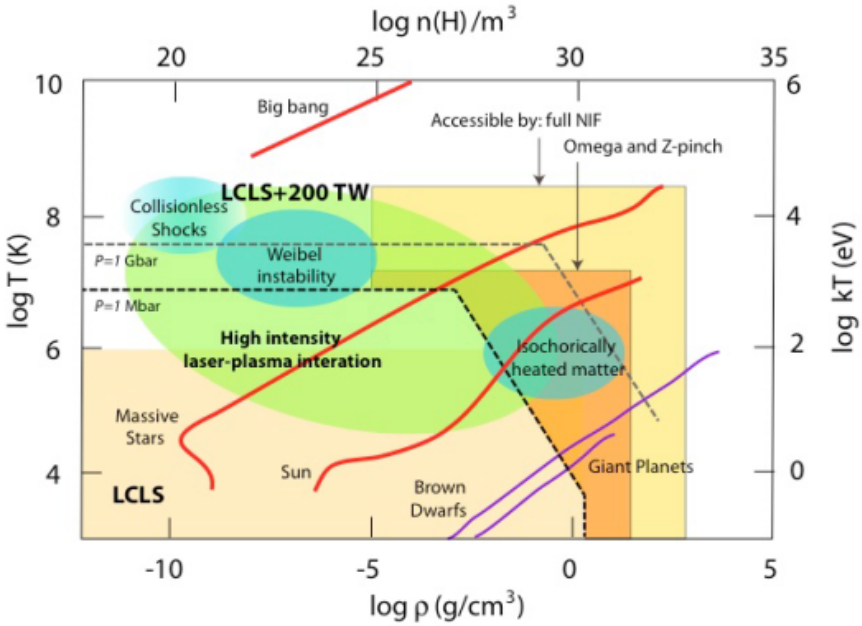

Figure 6.2: Temperature-density phase space accessible to LCLS and LWFA with the 200 TW laser at MEC (green area).

advantages compared to conventional accelerators are a large acceleration gradient of (>100 GeV/m) [13, 8], ultrashort duration ($\sim fs$) [73, 15], and inherent synchronization with the laser driver (and its triggering electronics). Another advantage of LWFA is the natural generation of betatron X-rays from transverse electron motion in the acceleration process [18]. For these reasons, LWFA systems are of interest for ultrafast pump-probe experiments in compact, flexible geometries. Exactly such a system would help SLAC expand the pump-probe capabilities of its Matter at Extreme Conditions (MEC) instrument of the Linac Coherent Light Source (LCLS) facility as LWFA would provide the flexability to quickly reconfigure experiments around the LCLS beamline.

This combination of LCLS with LWFA would allow for the exploration of a large range of high-energy-density (HED) conditions as shown in Figure 6.2. The complementary X-ray spectra (narrowband LCLS, broadband betatron) provide a unique platform for ultrafast X-ray pump/X-ray probe or X-ray pump/electron probe studies

of matter in extreme conditions. Notably, the ability to study isochorically heated matter, plasma instabilities, and shockwave phenomena with the ultrafast pump-probe capabilities of both the LCLS beam and LWFA radiation (electrons or betatron) is of particular interest to the HED community. Another possibility would be to directly measure the ultrashort duration of the LWFA electron bunch and demonstrate its inherent fs synchronicity for the first time. Furthermore, the combination of LWFA with LCLS would enable the study the propagation of anti-matter plasmas and formation of collisionless shocks, key topics of research in laboratory astrophysics. Such research could ultimately help determine the physical properties of matter at HED conditions, thus validating and improving modeling capabilities for fusion plasmas.

The two long-pulse lasers (ns) at MEC can perform pump-probe experiments on laser-shock compressed matter in conjuction with the LWFA electron beam and betatron source, analogous to the experiments in Chapter III. Irradiating a thin (μm) foil target from one or both sides with the ns pump beams would compress and shock the target while the electron beam or betatron X-rays probe the field or density structure of the target, respectively. The transmitted radiation can then be imaged to observe transitions in the laser-plasma interaction such as changes in the field magnitude or absorption spectrum as shown in Figure 6.3. By adjusting the temporal delay between the pulses, the field dynamics can be clearly resolved as the fs LWFA radiation essentially can take a snap-shot of the much longer ns interaction. These measurements would help clarify how the formation of pre-plasma on either one or both sides of the target changes the net field deflection of probe electrons.

Ultimately, integrating LWFA experiments with the LCLS X-ray beam would enable true fs-scale pump-probe experiments. Since both systems generate fs-scale radiation, there is a variety of experimental configurations possible as either can be used as a pump or a probe for the other. One potential experiment could be to

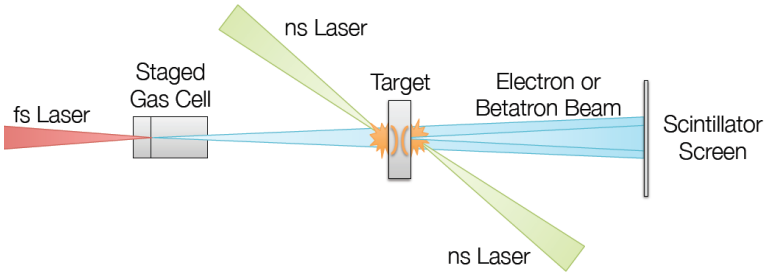

Figure 6.3: Experimental setup for back-lighting laser-pumped targets with LWFA electrons or betatron X-rays.

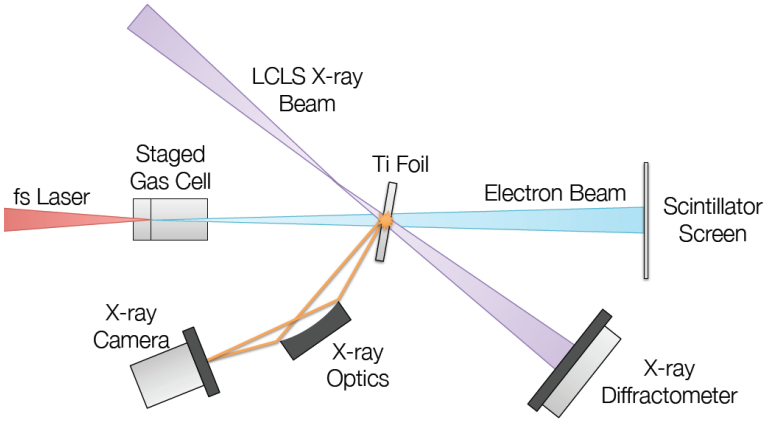

Figure 6.4: Experimental setup for measuring LWFA electron bunch duration using LCLS X-ray cross-correlation.

measure opacities and continuum lowering of warm dense matter (WDM) using the betatron X-rays as a pump and the LCLS X-rays as a probe. The broadband betatron X-rays could quickly photo-ionize and heat a thin foil target isochorically (without significantly changing the volume) into a WDM state, while the monochromatic LCLS X-rays would diffract off the target onto a detector screen. This X-ray diffraction would indicate the density and temperature conditions in the WDM and the X-ray absorption would provide detailed opacity measurements at those conditions.

While simulations and experimental evidence indicate that the LWFA electron bunch can be as low as 1 fs [15], the LWFA electron bunch has not been directly measured to date. Using the < 5 fs LCLS X-ray beam, the duration of LWFA electron

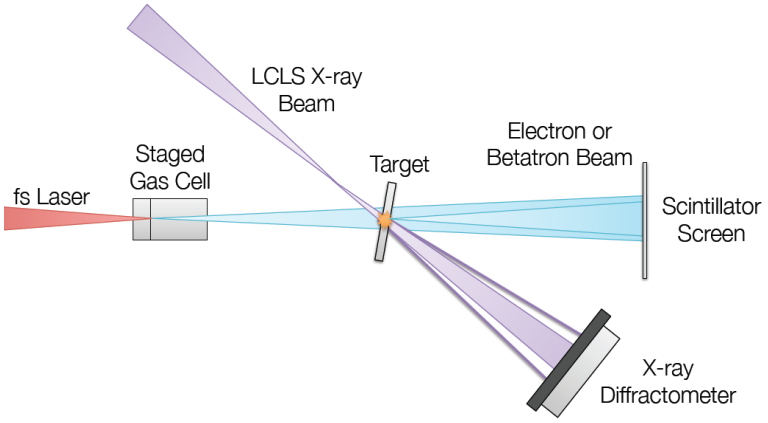

Figure 6.5: Experimental setup for combining LWFA electrons/betatron and LCLS X-rays in pump-probe.

bunches (and its subsequent betatron) could be measured with a cross-correlation experiment. LCLS X-rays focused on a thin titanium foil would create hollow K-shell titanium atoms that would emit a signature X-ray if temporally overlapped with the energetic LWFA electron beam as shown in Figure 6.4. By imaging these characteristic X-rays emitted from the titanium foil, the temporal overlap can be calculated from the spatial extent of the characteristic X-ray radiation and by knowing the angle between the two beams.

Once the cross-correlation between the two beams is performed, measuring the ultrafast dynamics of relativistic particles or X-rays interacting with materials would be feasible. Such experiments will enable direct experimental measurement of transition times and cross-sections for material processes on the fs-scale. Furthermore, transient high-strength electric and magnetic fields generated by relativistic LWFA electrons impacting the surface of a target will be measured with LCLS X-rays or a secondary electron beam to understand the evolution of rapidly heated plasmas. A generalized pump-probe experimental setup is shown in Figure 6.5.

Finally, the ability to compactly generate high-density, relativistic lepton jets using LWFA would allow the LCLS X-rays to pump or probe these exotic states

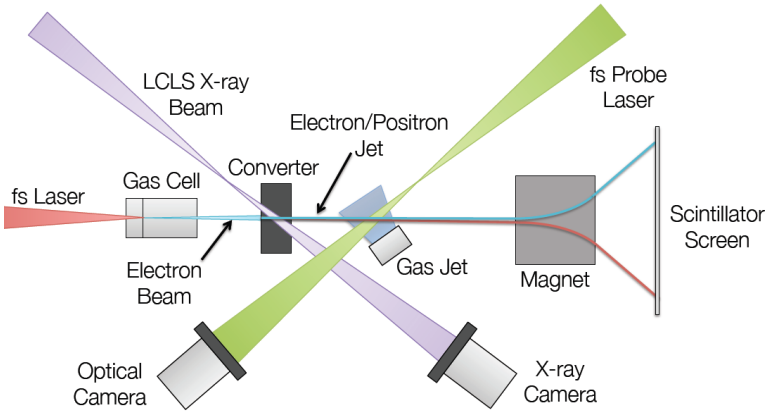

Figure 6.6: Experimental setup for measuring electron/positron jet filamentation in plasma.

of matter relevant to astrophysics. The lepton jets would be created by passing the LWFA electron beam through a thick (cm) high-Z converter target to create bremsstrahlung photons that subsequently undergo pair production to generate electrons and positrons (as detailed in Section 4.3). By increasing the thickness of the converter, the exiting electron/positron beam composition can be turned from purely electrons (with no converter) to practically charge neutral after approximately 5 radiation lengths (roughly 2.5 cm of Pb, scaling as A/Z^2) [118]. By propagating the exiting beam through another plasma (generated by another laser focused on a second gas jet/cell), the current filamentation instability can be studied in detail by backlighting the beam-plasma interaction with another short-pulse laser as shown in Figure 6.6. The LCLS X-ray beam can also directly probe the converter with the LCLS X-ray beam to observe the radiation transport of electrons and positrons through the high-Z material.

This will provide relativistic electrons and their subsequent betatron X-ray radiation for use in conjunction with the LCLS X-ray beam and other pump lasers. Using LWFA radiation to probe materials shocked and/or heated by these long-pulse pump lasers would develop deeper understanding of laser-matter interactions relevant to inertial confinement fusion (ICF), including the study of shockwave propagation

and hot electron transport. The opacity and continuum lowering of materials at WDM conditions could be measured in fine detail using the narrowband LCLS X-ray beam to probe materials irradiated by relativistic electrons or broadband betatron X-rays generated from LWFA. This could extend our understanding of HED opacities relevant to fusion plasmas.

Since compact pump-probe applications are one of the most desired abilities of LWFA, the direct measurement of the LWFA electron bunch duration using X-ray cross-correlation with the LCLS X-ray beam would be the first to measure the shot-to-shot duration of the LWFA electrons. As betatron radiation is created by the electron bunch inside the wakefield, this experiment would also effectively measure the betatron duration, an important aspect for its application at MEC. Lastly, this experiment could directly measure cross-sections of inner-shell X-ray transitions within various materials such as titanium or gold, the understanding of which is important for modeling materials relevant to fusion.

Finally, creating electron-positron jets with LWFA electrons would allow for the novel study of astrophysical phenomena with the high-brightness LCLS X-ray beam (see Figure 6.1). Due to the scalability of laboratory astrophysics, the compact nature of LWFA may allow for the study of galactic-scale electron-positron jets and gamma-ray bursts in a table-top platform. Propagating LWFA electron-positron jets through a secondary plasma will create similar conditions to those found in these astrophysical phenomena and enables controlled study of jet filamentation in the plasma, thought to be driven by turbulent electromagnetic fields seeded by current instabilities.

APPENDICES

APPENDIX A

List of Constants

Symbol	Description	Quantity
e	Charge of an Electron	$1.6 \times 10^{-19}\ C$
m_e	Mass of an Electron	$9.11 \times 10^{-31}\ kg$
m_p	Mass of an Proton/Neutron	$1.67 \times 10^{-27}\ kg$
c	Speed of Light in Vacuum	$2.998 \times 10^{8}\ m \cdot s$
ϵ_0	Permittivity of Free Space	$8.85 \times 10^{-12}\ F \cdot m^{-1}$
μ_0	Permeability of Free Space	$4\pi \times 10^{-7}\ H \cdot m^{-1}$
h	Planck's Constant	$6.63 \times 10^{-34}\ J \cdot s$

Table A.1: Table of fundamental constants.

APPENDIX B

Monte-Carlo Algorithm for NLTS

B.1 Introduction

NLTS experiments require the precise overlap of an intense laser pulse and an electron beam to produce a high-energy, high-brillance photon beam. Unfortunately, due to pointing fluctuations from vibrations, temperature gradients, beam instabilites, etc. (Figure 2.11), the overlap probability is significantly decreased, causing the resulting photon yield to drop. To study these effects, a MATLAB code that uses Monte Carlo methods was developed to simulate the effects of optical support vibrations and air currents perturbations and compute the consequences in terms of photon yield. The code was used to study the influence of several parameters in the NLTS experiment, such as spatial separation and timing difference between the two beams.

B.2 Perturbation Generation

Vibrations around the lab can cause the optical tables to oscillate, moving the mirrors and deflecting the beams. There are approximately 180 mirrors in the HERCULES laser, and the optical path is long (200 m), so even a small movement can have

a large effect. Many events in and around the lab can cause the tables to vibrate: a car in the street, construction projects, someone walking nearby, air conditioning fans, seismic vibration of the earth, leaning on a table, etc. When a table oscillates, the mirrors on top of it start moving, deflecting the beam. These perturbations are simulated by sampling several variables:

- At one given instant, the number of vibration sources around the lab is sampled from a Poisson distribution of mean 5, using a table lookup method.
- The frequency of each vibration is sampled from a truncated normal distribution of mean 150 Hz and standard deviation 150 Hz, using acceptance-rejection method.
- The amplitude of each vibration is sampled from an exponential distribution, using inverse transform method. $A = -A_0 \log(\xi)$, where ξ is a random number between 0 and 1 (resulting from MATLAB's `rand(1)`) and A_0 is a constant ($A_0 = 10^{-6}\ m$).
- Depending on the configuration of the lab, not all mirrors are affected by a given vibration. To reflect this, a binary decides if a mirror is hit by a vibration (with probability of 0.3) or not.
- The mirrors do not necessarily move together. The phase difference for each mirror is sampled from a uniform distribution between 0 and 2π.

The response of a typical table to a vibration depends on the frequency with an exponential law (Fig. B.1). The compliance is the ratio between the amplitude of the ground vibration and the amplitude of the table vibration.

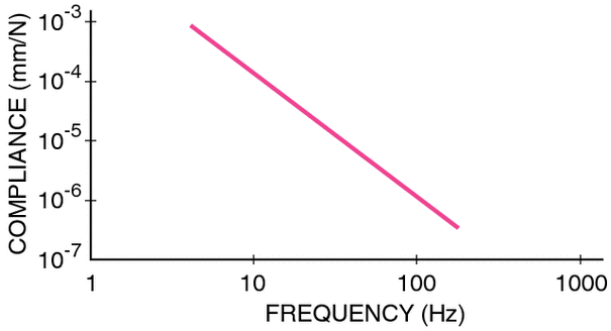

Figure B.1: Compliance curve of an ideal rigid body.

Once these values are known, the deflection of the beam on the target due to one mirror and one vibration is:

$$\delta = A \cdot \frac{R(f)}{L_{table}} \cdot \cos(\phi) \cdot L \tag{B.1}$$

where A is the amplitude of the vibration, $R(f)$ is the response of the table (depending on the frequency f), L_{table} is the length of the table, ϕ is the phase and L is the distance between the mirror and the target. The sum over all mirrors and all vibration sources provides the total deviation due to vibrations.

Gradients of pressure, temperature and humidity change the index of refraction of the air. An index gradient deflects the light, resulting in a deviation of the beam. In the code, the gradients of pressure, temperature and humidity in 5 different areas are sampled from normal distribution using the Box-Muller transform. The resulting index gradient is dn/dl. At small angles, the deviation on target is:

$$\delta = dn/dl \cdot \delta l \cdot L \tag{B.2}$$

where δl is the distance over which the gradient in present, and L is the distance to the target. The sum over all areas provides the total deviation of the beam on the target.

B.3 Beam Overlap and Photon Yield

The previous simulations provide the deflection of the laser beam. The system setup is such that the laser spot driving the electron beam moves in the same direction, but its deflection is 10 times higher due to the difference in focal lengths. Once the centers of the laser beam and electron beam are known, it is possible to compute the number of photons produced. The electron beam has an elliptical normal distribution of 2 μm FWHM on the x-axis and 1 μm on the y-axis, while uniformly diverging at 5 $mrad$ FWHM. One shot contains a total of $N_{e^-} = 10^8$ electrons. The intensity of laser beam has normal distribution of 4 μm FWHM, peaked at an a_0 of 30. When an electron hits the laser beam, it produces a_0^2 photons, where a_0^2 is the proportional to the intensity of the laser beam. Two methods can be used to compute the number of photons:

1. Both distributions are evaluated on a 100 μm $\times$ 100 μm grid, giving a matrix `ebeam` for the electron beam and `laser_a0` for the laser beam. Then the number of photons is computed in MATLAB through element multiplication: `photon = sum(sum(ebeam.*laser_a0.*laser_a0))`.

2. The second method applies Monte Carlo directly using the intensity of the laser as a cross section. N electrons are thrown to points (x, y) randomly sampled from the electron beam distribution. Each electron produces $a_0(x, y)^2$ photons. The number of photons is then multiplied by N_e/N for normalization.

Figure B.2 shows the distribution of the beam deflection due to air currents and vibrations. It looks like an ellipsis of about 30 μm diameter, which is consistent with the experimental results. The ellictical shape is due to the fact that air currents and vibrations have a larger impact on the vertical deflection than on the horizontal deflection.

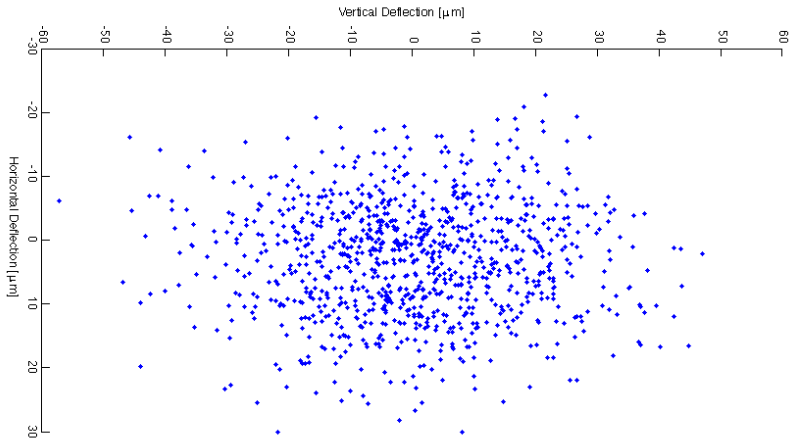

Figure B.2: Distribution of pointing from air currents and mirror vibrations.

B.4 MATLAB Code

B.4.1 Main Program

```
%computes the photon yield with all perturbations

overlap = 2;
%method to compute the photon yield
%1 -> monte-carlo
%2 -> grid

%parameters:
Lmax = 180;                  % defines maximum length [meters]
S = 1000;  % defines number of samples
output = zeros(S,1);
% creates output for number of photons generated per run

%mirrors:
N1 = 175; %one set of mirrors
N2 = 7; %mirrors in the ring amplifier
ringpos = 120;
ringdist = 0.05;
posmir2 = ringpos:ringdist:(ringpos+(7*25-1)*ringdist);
%positions of mirrors in the ring
Amp = 1e-4; %average amplitude of vibrations (arbit. unit)
N11 = 125;
posmir1 = [linspace(1,119,N11), linspace(130,179,N1-N11)];
%positions of the other mirrors.
```

```
p = 0.3;%probability that a mirror is actualy hit by a given vibration
f0 = 100; %some frequency (Hz) for the compliance curve
RTx = 1e-3; %table response on x-axis
RTy = 1e-4; %table response on y-axis

%air currents:
V = 4;     % defines number of variables per air current
N = 5;     % defines number of air currents
L = [5, 10,120,130,140]; % defines location of air currents [meters]
dl = [2,2,1,0.5,1];         % defines length of air currents [meters]
skew = 2;                   % defines x-y skew of distribution
dP = 3e-8;% defines maximum pressure gradient index (for 0.1 atm/m)
dT = 1e-8;% defines maximum temperature gradient index  (for 10 C/m)
dH = 1e-8;% defines maximum humidity gradient index (for 1% RH/m)

%laser and electron beams
a0_max = 30;
% defines maximum normalized vector potential of laser pulse
% (analogous to sqrt of intensity)
Ne = 1e8;       % defines number of electrons in beam [#]
ed = 5e-3;      % defines electron beam divergence [rad]
ep = 3e-3;      % defines electron beam shot-to-shot pointing [rad]
eoffx = 0;      % defines electron beam offset in x [microns]
eoffy = 10;      % defines electron beam offset in y [microns]

dz = 2e-3;
% defines seperation between laser focus and e beam source [meters]
z = 0e-6;        % defines amount of spatial delay [microns] (causes
%overlap in another plane along axis)
w0l = 2e-6;         % defines minimim beam waist of laser
w0e = 5e-7;          %  minimim beam waist and e beam [m]

zr = pi*w0l^2/0.8;   % defines Rayleigh length of laser pulse [microns]
wl = w0l*sqrt(1+(z/zr)^2);
% calculates laser waist as a function of delay [microns]
a0_norm = a0_max/((1+(z/zr)^2)^(1/2));
% calculates laser potential at new waist
we = w0e + ed*(dz-z)/2;
% calculates electron beam waist at new overlap plane

rl = wl/sqrt(log(2));%constant for the exponential law of the laser
%we = 6e-6;%FWHM of the electron beam (m)
re = we/sqrt(log(2));
%constant (m) in the exponential law for the electron beam
```

```
sigma_laser = ([wl, wl]*1e6).^2; % defines laser beam waist in 2D
sigma_ebeam = ([we*skew, we]*1e6).^2; % defines electron
%beam waist in 2D (with skew in X axis)

spot = zeros(1,2);%generates array for spot deflection for each sample

for s = 1:S
%deflection due due to mirrors at one instant
nvib = poisson(5); %number of vibration sources
vibs = zeros(2,nvib);

for n = 1:nvib
    vibs(1,n) = gaussian_acrej(149,149);
    %frequency of the vibration (Hz), following a normal distribution
    vibs(2,n) = -Amp*log(rand(1));
    %amplitude of the vibration
end

mdev1x = zeros(nvib,N1,2);
mdev2x = zeros(nvib,N2,2);
mdev1y = zeros(nvib,N1,2);
mdev2y = zeros(nvib,N2,2);

for n = 1:N1
    for k = 1:nvib
        if rand(1) < p
            mdev1x(k,n,1) = vibs(2,k)*RTx*exp(-vibs(1,k)/f0);
            %movement of the mirror in the x direction (m)
            mdev1x(k,n,2) = 2*pi*rand(1);
            %mdev1x(k,n,2) = 0;
            %phase of the movement at the time of the shot
            mdev1y(k,n,1) = vibs(2,k)*RTy*exp(-vibs(1,k)/f0);
            mdev1y(k,n,2) = 2*pi*rand(1);
            %mdev1y(k,n,2) = 0;
            %same thing in the y direction
        end
    end
end

%same thing for the mirrors in the ring amplifier
for n = 1:N2
    for k = 1:nvib
        if rand(1) < p
            mdev2x(k,n,1) = vibs(2,k)*RTx*exp(-vibs(1,k)/f0);
            mdev2x(k,n,2) = 2*pi*rand(1);
```

```
            mdev2y(k,n,1) = vibs(2,k)*RTy*exp(-vibs(1,k)/f0);
            mdev2y(k,n,2) = 2*pi*rand(1);
        end
    end
end

mirrordevx = 0; %total deflection on x (m)
mirrordevy = 0; %total deflection on y (m)

for n = 1:N1
    for k = 1:nvib
        mirrordevx = mirrordevx + mdev1x(k,n,1)*...
            cos(mdev1x(k,n,2))*(Lmax-posmir1(n))/1;
        %for each mirror, movement of the table times cos of the
        %phase times distance to target over size of the table
        %gives deflection on the x axis
        mirrordevy = mirrordevy + mdev1y(k,n,1)*...
            cos(mdev1y(k,n,2))*(Lmax-posmir1(n))/1;
    end
end

%same thing for mirrors in the ring
for n = 1:N2
    for k = 1:nvib
        for q = 1:25
            mirrordevx = mirrordevx + mdev2x(k,n,1)* ...
                cos(mdev2x(k,n,2))*(Lmax-posmir2((q-1)*N2+n))/1;
            mirrordevy = mirrordevy + mdev2y(k,n,1)* ...
                cos(mdev2y(k,n,2))*(Lmax-posmir2((q-1)*N2+n))/1;
        end
    end
end

%mirrordevx
%mirrordevy
%deviation due to air currents

x = zeros(N,V,2);           % generates array for sample outputs
angle = zeros(N,2);         % generates array for angle outputs

deflection = zeros(N,2);
% generates array for variance and mean for each batch

j = 1; % resets random number index
for d = 1:2 % loops over dimensions
```

```
for i = 1:N % loops over air currents
for k = 1:V % loops over variables
    x(k,i,d) = sqrt(-2*log(rand(1)))*cos(2*pi*rand(1));
    % performs Box-Muller transform to get a normal
    % distribution for the air current deviations
end
    angle(i,d) = x(1,i,d)*dP + x(2,i,d)*dT + x(3,i,d)*dH;
    % sums all air current small angle deflections
end
deflection(:,d) = (angle(:,d)).*transpose(Lmax - L).*transpose(dl);
% calculates  deviation of the center of the alignment axis
% at the end of the laser chain
end

totaldevx = mirrordevx + sum(deflection(:,1))/skew;
totaldevy = mirrordevy + sum(deflection(:,2));

spot(s,1) = totaldevx;  % saves spot deflections for X-axis
spot(s,2) = totaldevy;  % saves spot deflections for Y-axis

if overlap == 1
%computes the number of photons resuling of the interactions
%between the beams
lcenter = [0.1*totaldevx,0.1*totaldevy]; %center of the laser beam (m)
ecenter = 10*lcenter; %center of the electron beam (m)

%Fl = @(x,y)(a0_norm*exp(-((x-lcenter(1))^2+(y-lcenter(2))^2)/(rl^2)));
Fl = @(x,y)(a0_norm*exp(-(x-lcenter(1))^2/(2*wl^2)- ...
    (y-lcenter(2))^2/(2*wl^2)));
%normal law for the laser beam

Nelec = 1000;
Nphot = 0;
%Nelec electrons are sent. Their positions are normally
%  sampled around the center of the electron beam.
for n = 1:Nelec
    %theta = pi*rand(1); %random angle
    %r = normrnd(0,re); %random distance
    %x = ecenter(1) + r*cos(theta)*skew;
    %y = ecenter(2) + r*sin(theta); %position of the electron
    x = ecenter(1) + normrnd(0,skew*we);
    y = ecenter(2) + normrnd(0,we);
    Nphot = Nphot+(Fl(x,y))^2; %number of photons created by
    % one electron at this position in the laser beam
end
```

```
Nphot = Nphot*Ne/Nelec; %normalization of the number of photons
output(s,1) = Nphot;
end

if overlap == 2

mu_laser = [totaldevx*1e5 totaldevy*1e5]; % defines expectation
%of laser axis including deflection
mu_ebeam = [((totaldevx+x(1,i,d)*ep*dz)*1e6 + eoffx) ...
((totaldevy+x(1,i,d)*ep*dz)*1e6+eoffy)]; % defines expectation
%of ebeam axis including 10x greater deflection

[X1,X2] = meshgrid(linspace(-50,50,100)',linspace(-50,50,100)');
% creates 100 x 100 grid for laser/ebeam distributions
X = [X1(:) X2(:)]; % creates a set op X1,X2 points  distribution
%for 2D normal function

laser = reshape(mvnpdf(X,mu_laser,sigma_laser),100,100);
% normally distributes
%laser in 2D with defined axis and waist
laser_a0 = laser / max(max(laser))*a0_norm;
%normalized laser with updated  vector potential
ebeam = reshape(mvnpdf(X,mu_ebeam,sigma_ebeam),100,100)*Ne;
% normally distributes ebeam in 2D with
% defined axis, waist, and electron number

photon = ebeam.*laser_a0.*laser_a0;
% calculates number of photons per unit bin as
% Ne*a0^2 per bin
output(s,1) = sum(sum(photon)); % sums photons over all bins
end
end

output(isnan(output)) = 0;
m = mean(output);
sigma = std(output);
error = 2*sigma/sqrt(S);
```

B.4.2 Functions

```
function [ x ] = gaussian_acrej( m,s )
%generates gaussian random numbers with mean m and std s
%using acceptance-rejection
acc = 0;
```

```
while acc == 0
    x = (m+4*s)*rand(1);
    y = rand(1);
    if y < exp(1/2*((x-m)/s)^2)
        acc = 1;
    end
end
end

function [ k ] = poisson( l )
%generates numbers following a poisson distribution
%wth mean l using a table lookup method
x = rand(1);
k = 0;
S = exp(-l);
while S < x
    k = k+1;
    S = S+exp(-l)*(l^k)/factorial(k);
end
k = k+1;
%shift result to get values from 1 to infinity, same distribution
end
```

BIBLIOGRAPHY

BIBLIOGRAPHY

[1] T. Tajima and J. M. Dawson. Laser electron accelerator. *Physical Review Letters*, 43:267, 1979.

[2] A. G. R. Thomas, S. P. D. Mangles, Z. Najmudin, M. C. Kaluza, C. D. Murphy, and K. Krushelnick. Measurements of wave-breaking radiation from a laser-wakefield accelerator. *Physical Review Letters*, 98:054802, 2007.

[3] V. Malka, S. Fritzler, E. Lefebvre, M.-M. Aleonard, F. Burgy, J.-P. Chambaret, J.-F. Chemin, K. Krushelnick, G. Malka, S.P.D. Mangles, et al. Electron acceleration by a wake field forced by an intense ultrashort laser pulse. *Science*, 298:1596–1600, 2002.

[4] E. Esarey, R. F. Hubbard, W. P. Leemans, A. Ting, and P. Sprangle. Electron injection into plasma wakefields by colliding laser pulses. *Physical Review Letters*, 79:2682, 1997.

[5] S. P. D. Mangles, G. Genoud, M. S. Bloom, M. Burza, Z. Najmudin, A. Persson, K. Svensson, A. G. R. Thomas, and C.-G. Wahlström. Self-injection threshold in self-guided laser wakefield accelerators. *Physical Review Special Topics: Accelerators and Beams*, 15:011302, 2012.

[6] C. McGuffey, T. Matsuoka, S. Kneip, W. Schumaker, F. Dollar, C. Zulick, V. Chvykov, G. Kalintchenko, V. Yanovsky, A. Maksimchuk, et al. Experimental laser wakefield acceleration scalings exceeding 100 tw. *Physics of Plasmas*, 19:063113, 2012.

[7] A. Pukhov and J. Meyer-ter Vehn. Laser wake field acceleration: the highly non-linear broken-wave regime. *Applied Physics B*, 74:355–361, 2002.

[8] S. Kneip, S. R. Nagel, S. F. Martins, S. P. D. Mangles, C. Bellei, O. Chekhlov, R. J. Clarke, N. Delerue, E. J. Divall, G. Doucas, K. Ertel, F. Fiuza, R. Fonseca, P. Foster, S. J. Hawkes, C. J. Hooker, K. Krushelnick, W. B. Mori, C. A. J. Palmer, K. Ta Phuoc, P. P. Rajeev, J. Schreiber, M. J. V. Streeter, D. Urner, J. Vieira, L. O. Silva, and Z. Najmudin. Near-gev acceleration of electrons by a nonlinear plasma wave driven by a self-guided laser pulse. *Physical Review Letters*, 103:035002, 2009.

[9] X. Wang, R. Zgadzaj, N. Fazel, Z. Li, S. A. Yi, Xi Zhang, W. Henderson, Y.-Y. Chang, R. Korzekwa, H.-E. Tsai, et al. Quasi-monoenergetic laser-plasma acceleration of electrons to 2 gev. *Nature Communications*, 4, 2013.

[10] S. P. D. Mangles, C. D. Murphy, Z. Najmudin, A. G. R. Thomas, J. L. Collier, A. E. Dangor, E. J. Divall, P. S. Foster, J. G. Gallacher, C. J. Hooker, et al. Monoenergetic beams of relativistic electrons from intense laser–plasma interactions. *Nature*, 431:535–538, 2004.

[11] C. G. R. Geddes, C. Toth, J. Van Tilborg, E. Esarey, C. B. Schroeder, D. Bruhwiler, C. Nieter, J. Cary, and W. P. Leemans. High-quality electron beams from a laser wakefield accelerator using plasma-channel guiding. *Nature*, 431:538–541, 2004.

[12] J. Faure, Y. Glinec, A. Pukhov, S. Kiselev, S. Gordienko, E. Lefebvre, J.-P. Rousseau, F. Burgy, and V. Malka. A laser–plasma accelerator producing monoenergetic electron beams. *Nature*, 431:541–544, 2004.

[13] W. P. Leemans, B. Nagler, A. J. Gonsalves, C. Toth, K. Nakamura, C. G. R. Geddes, E. Esarey, C. B. Schroeder, and S. M. Hooker. Gev electron beams from a centimetre-scale accelerator. *Nature Physics*, 2:696–699, 2006.

[14] W. Leemans and E. Esarey. Laser-driven plasma-wave electron accelerators. *Physics Today*, 62:44–49, 2009.

[15] O. Lundh, J. Lim, C. Rechatin, L. Ammoura, A. Ben-Ismail, X. Davoine, G. Gallot, J-P. Goddet, E. Lefebvre, V. Malka, and J. Faure. Few femtosecond, few kiloampere electron bunch produced by a laser-plasma accelerator. *Nature Physics*, 7:219–222, 2011.

[16] S. Corde, K. Ta Phuoc, G. Lambert, R. Fitour, V. Malka, A. Rousse, A. Beck, and E. Lefebvre. Femtosecond x rays from laser-plasma accelerators. *Review of Modern Physics*, 85:1–48, 2013.

[17] A. Rousse, K. Ta Phuoc, R. Shah, A. Pukhov, E. Lefebvre, V. Malka, S. Kiselev, F. Burgy, J.-P. Rousseau, D. Umstadter, et al. Production of a kev x-ray beam from synchrotron radiation in relativistic laser-plasma interaction. *Physical Review Letters*, 93:135005, 2004.

[18] S. Kneip, C. McGuffey, J. L. Martins, S. F. Martins, C. Bellei, V. Chvykov, F. Dollar, R. Fonseca, C. Huntington, G. Kalintchenko, et al. Bright spatially coherent synchrotron x-rays from a table-top source. *Nature Physics*, 6:980–983, 2010.

[19] S. Cipiccia, M. R. Islam, B. Ersfeld, R. P. Shanks, E. Brunetti, G. Vieux, X. Yang, R. C. Issac, S. M. Wiggins, G. H. Welsh, et al. Gamma-rays from harmonically resonant betatron oscillations in a plasma wake. *Nature Physics*, 7:867–871, 2011.

[20] S. Kneip, C. McGuffey, J. L. Martins, M. S. Bloom, V. Chvykov, F. Dollar, R. Fonseca, S. Jolly, G. Kalintchenko, K. Krushelnick, A. Maksimchuk, S. P. D. Mangles, Z. Najmudin, C. A. J. Palmer, K. Ta Phuoc, W. Schumaker, L. O. Silva, J. Vieira, V. Yanovsky, and A. G. R. Thomas. Characterization of transverse beam emittance of electrons from a laser-plasma wakefield accelerator in the bubble regime using betatron x-ray radiation. *Physical Review Special Topics: Accelerators and Beams*, 15:021302, 2012.

[21] V. Ramanathan, S. Banerjee, N. D. Powers, N. Cunningham, N. A. Chandler-Smith, K. Zhao, K. Brown, D. P. Umstadter, S. Clarke, S. Pozzi, J. Beene, C. R. Vane, and D. Schultz. Submillimeter-resolution radiography of shielded structures with laser-accelerated electron beams. *Physical Review Special Topics: Accelerators and Beams*, 13:104701, 2010.

[22] S. Kneip, C. McGuffey, F. Dollar, M. S. Bloom, V. Chvykov, G. Kalintchenko, K. Krushelnick, A. Maksimchuk, S. P. D. Mangles, T. Matsuoka, et al. X-ray phase contrast imaging of biological specimens with femtosecond pulses of betatron radiation from a compact laser plasma wakefield accelerator. *Applied Physics Letters*, 99:093701, 2011.

[23] G. R. Gould. The laser, light amplification by stimulated emission of radiation. In *The Ann Arbor Conference on Optical Pumping, the University of Michigan, June 15 through June 18, 1959.*, page 128, Ann Arbor, Michigan, USA, 1959. University of Michigan.

[24] T. H. Maiman. Stimulated optical radiation in ruby. *Nature*, 187:493–494, 1960.

[25] J. Nuckolls and L. Wood. Laser compression of matter to super-high densities. *Nature*, 239:139, 1972.

[26] D. Strickland and G. Mourou. Compression of amplified chirped optical pulses. *Optics Communications*, 55:447–449, 1985.

[27] M. D. Perry and G. Mourou. Terawatt to petawatt subpicosecond lasers. *Science*, 264:917–924, 1994.

[28] R. M. G. M. Trines, F. Fiúza, R. Bingham, R. A. Fonseca, L. O. Silva, R. A. Cairns, and P. A. Norreys. Simulations of efficient raman amplification into the multipetawatt regime. *Nature Physics*, 7:87–92, 2011.

[29] R. M. G. M. Trines, F. Fiúza, R. Bingham, R. A. Fonseca, L. O. Silva, R. A. Cairns, and P. A. Norreys. Production of picosecond, kilojoule, and petawatt laser pulses via raman amplification of nanosecond pulses. *Physical Review Letters*, 107:105002, 2011.

[30] G. Mourou, B. Brocklesby, T. Tajima, and J. Limpert. The future is fibre accelerators. *Nature Photonics*, 7:258–261, 2013.

[31] V. Yanovsky, V. Chvykov, G. Kalinchenko, P. Rousseau, T. Planchon, T. Matsuoka, A. Maksimchuk, J. Nees, G. Cheriaux, G. Mourou, and K. Krushelnick. Ultra-high intensity 300-tw laser at 0.1 hz repetition rate. *Optics Express*, 16:2109–2114, 2008.

[32] C. J. Hooker, J. L. Collier, O. Chekhlov, R. Clarke, E. Divall, K. Ertel, B. Fell, P. Foster, S. Hancock, A. Langley, et al. The astra gemini project–a dual-beam petawatt ti: Sapphire laser system. In *Journal de Physique IV*, volume 133, pages 673–677, 2006.

[33] V. Chvykov, P. Rousseau, S. Reed, G. Kalinchenko, and V. Yanovsky. Generation of 10^{11} contrast 50 tw laser pulses. *Optics Letters*, 31:1456–1458, 2006.

[34] X. Liu, R. Wagner, A. Maksimchuk, E. Goodman, J. Workman, D. Umstadter, and A. Migus. Nonlinear temporal diffraction and frequency shifts resulting from pulse shaping in chirped-pulse amplification systems. *Optics Letters*, 20:1163–1165, 1995.

[35] P. A. Franken, A. E. Hill, C. W. Peters, and G. Weinreich. Generation of optical harmonics. *Physical Review Letters*, 7:118–119, 1961.

[36] S. Semushin and V. Malka. High density gas jet nozzle design for laser target production. *Review of Scientific Instruments*, 72:2961–2965, 2001.

[37] B. B. Pollock, C. E. Clayton, J. E. Ralph, F. Albert, A. Davidson, L. Divol, C. Filip, S. H. Glenzer, K. Herpoldt, W. Lu, K. A. Marsh, J. Meinecke, W. B. Mori, A. Pak, T. C. Rensink, J. S. Ross, J. Shaw, G. R. Tynan, C. Joshi, and D. H. Froula. Demonstration of a narrow energy spread, 0.5 gev electron beam from a two-stage laser wakefield accelerator. *Physical Review Letters*, 107:045001, 2011.

[38] S. W. Jolly, Z. H. He, C. McGuffey, W. Schumaker, K. Krushelnick, and A. G. R. Thomas. Stereolithography based method of creating custom gas density profile targets for high intensity laser-plasma experiments. *Review of Scientific Instruments*, 83:073503, 2012.

[39] M. Vargas, W. Schumaker, Z. He, V. Chyvkov, B. Hou, A. Maksimchuk, et al. Improvements to laser wakefield accelerated electron beam stability, divergence, and energy spread using two-stage gas cell targets. (submitted, in peer review).

[40] J. Osterhoff, A. Popp, Z. Major, B. Marx, T. P. Rowlands-Rees, M. Fuchs, M. Geissler, R. Hörlein, B. Hidding, S. Becker, et al. Generation of stable, low-divergence electron beams by laser-wakefield acceleration in a steady-state-flow gas cell. *Physical Review Letters*, 101:085002, 2008.

[41] C. E. Clayton, J. E. Ralph, F. Albert, R. A. Fonseca, S. H. Glenzer, C. Joshi, W. Lu, K. A. Marsh, S. F. Martins, W. B. Mori, A. Pak, F. S. Tsung, B. B. Pollock, J. S. Ross, L. O. Silva, and D. H. Froula. Self-guided laser wakefield

acceleration beyond 1 gev using ionization-induced injection. *Physical Review Letters*, 105:105003, 2010.

[42] A. J. Gonsalves, K. Nakamura, C. Lin, D. Panasenko, S. Shiraishi, T. Sokollik, C. Benedetti, C. B. Schroeder, C. G. R. Geddes, J. Van Tilborg, et al. Tunable laser plasma accelerator based on longitudinal density tailoring. *Nature Physics*, 7:862–866, 2011.

[43] I. J. Paterson, R. J. Clarke, N. C. Woolsey, and G. Gregori. Image plate response for conditions relevant to laserplasma interaction experiments. *Measurement Science and Technology*, 19:095301, 2008.

[44] K. A. Tanaka, T. Yabuuchi, T. Sato, R. Kodama, Y. Kitagawa, T. Takahashi, T. Ikeda, Y. Honda, and S. Okuda. Calibration of imaging plate for high energy electron spectrometer. *Review of Scientific Instruments*, 76:013507–013507, 2005.

[45] G. Fiksel, F. J. Marshall, C. Mileham, and C. Stoeckl. Note: Spatial resolution of fuji bas-tr and bas-sr imaging plates. *Review of Scientific Instruments*, 83, 2012.

[46] C. Zulick, F. Dollar, V. Chvykov, J. Davis, G. Kalinchenko, A. Maksimchuk, G. M. Petrov, A. Raymond, A. G. R. Thomas, L. Willingale, V. Yanovsky, and K. Krushelnick. Energetic neutron beams generated from femtosecond laser plasma interactions. *Applied Physics Letters*, 102, 2013.

[47] R. Fonseca, L. Silva, F. Tsung, V. Decyk, W. Lu, C. Ren, W. Mori, S. Deng, S. Lee, T. Katsouleas, and J. Adam. Osiris: A three-dimensional, fully relativistic particle in cell code for modeling plasma based accelerators. In Peter Sloot, Alfons Hoekstra, C. Tan, and Jack Dongarra, editors, *Computational Science ICCS 2002*, volume 2331 of *Lecture Notes in Computer Science*, pages 342–351. Springer Berlin / Heidelberg, 2002.

[48] G. Battistoni, F. Cerutti, A. Fasso, A. Ferrari, S. Muraro, J. Ranft, S. Roesler, and P. R. Sala. The fluka code: Description and benchmarking. In *AIP Conference Proceedings*, volume 896, page 31, 2007.

[49] J. T. Larsen and S. M. Lane. Hyadesa plasma hydrodynamics code for dense plasma studies. *Journal of Quantitative Spectroscopy and Radiative Transfer*, 51:179–186, 1994.

[50] F. J. Dollar. *High Intensity, High Contrast Laser Solid Interactions with Short Pulses.* PhD thesis, The University of Michigan., Ann Arbor, Michigan, USA, 2012.

[51] F. Dollar, P. Cummings, V. Chvykov, L. Willingale, M. Vargas, V. Yanovsky, C. Zulick, A. Maksimchuk, A. G. R. Thomas, and K. Krushelnick. Scaling high-order harmonic generation from laser-solid interactions to ultrahigh intensity. *Physical Review Letters*, 110:175002, 2013.

[52] COMSOL Inc. http://www.comsol.com.

[53] M. Tabak, J. Hammer, M. E. Glinsky, W. L. Kruer, S. C. Wilks, J. Woodworth, E. M. Campbell, M. D. Perry, and R. J. Mason. Ignition and high gain with ultrapowerful lasers. *Physics of Plasmas*, 1:1626–1634, 1994.

[54] L. Biermann. Uber den ursprung der magnetfelder auf sternen und im interstellaren raum,. *Z. Naturfors.*, 5:128, 1950.

[55] P. Kolodner and E. Yablonovitch. Two-dimensional distribution of self-generated magnetic fields near the laser-plasma resonant- interaction region. *Physical Review Letters*, 43:1402–1403, 1979.

[56] D. W. Forslund and J. U. Brackbill. Magnetic-field-induced surface transport on laser-irradiated foils. *Physical Review Letters*, 48:1614–1617, 1982.

[57] P. McKenna, D. C. Carroll, R. J. Clarke, R. G. Evans, K. W. D. Ledingham, F. Lindau, O. Lundh, T. McCanny, D. Neely, A. P. L. Robinson, L. Robin, P. T. Simpson, C.-G. Wahlstrom, and M. Zepf. Lateral electron transport in high-intensity laser-irradiated foils diagnosed by ion emission. *Physical Review Letters*, 98:145001, 2007.

[58] C. P. Ridgers, M. Sherlock, R. G. Evans, A. P. L. Robinson, and R. J. Kingham. Superluminal sheath-field expansion and fast-electron-beam divergence measurements in laser-solid interactions. *Physical Review E*, 83:036404, 2011.

[59] F. Califano, R. Prandi, F. Pegoraro, and S. V. Bulanov. Nonlinear filamentation instability driven by an inhomogeneous current in a collisionless plasma. *Physical Review E*, 58:7837, 1998.

[60] M. Borghesi, D. H. Campbell, A. Schiavi, O. Willi, M. Galimberti, L. A. Gizzi, A. J. MacKinnon, R. D. Snavely, P. Patel, S. Hatchett, M. Key, and W. Nararov. Propagation issues and energetic particle production in laser-plasma interactions at intensities exceeding 1019 w/cm2. *Laser and Particle Beams*, 20:31–38, 2002.

[61] C. K. Li, F. H. Séguin, J. A. Frenje, J. R. Rygg, R. D. Petrasso, R. P. J. Town, P. A. Amendt, S. P. Hatchett, O. L. Landen, A. J. Mackinnon, P. K. Patel, V. A. Smalyuk, T. C. Sangster, and J. P. Knauer. Measuring e and b fields in laser-produced plasmas with monoenergetic proton radiography. *Physical Review Letters*, 97:135003, 2006.

[62] P. M. Nilson, L. Willingale, M. C. Kaluza, C. Kamperidis, S. Minardi, M. S. Wei, P. Fernandes, M. Notley, S. Bandyopadhyay, M. Sherlock, R. J. Kingham, M. Tatarakis, Z. Najmudin, W. Rozmus, R. G. Evans, M. G. Haines, A. E. Dangor, and K. Krushelnick. Magnetic reconnection and plasma dynamics in two-beam laser-solid interactions. *Physical Review Letters*, 97:255001, 2006.

[63] S. L. Pape, D. Hey, P. Patel, A. Mackinnon, R. Klein, B. Remington, S. C. Wilks, D. Ryutov, S. Moon, and M. Foord. Proton radiography of megagauss electromagnetic fields generated by the irradiation of a solid target by an ultraintense laser pulse. *Astrophysics and Space Science*, 307:341–345, 2007.

[64] C. A. Cecchetti, M. Borghesi, J. Fuchs, G. Schurtz, S. Kar, A. Macchi, L. Romagnani, P. A. Wilson, P. Antici, R. Jung, et al. Magnetic field measurements in laser-produced plasmas via proton deflectometry. *Physics of Plasmas*, 16:043102, 2009.

[65] L. Willingale, P. M. Nilson, M. C. Kaluza, A. E. Dangor, R. G. Evans, P. Fernandes, M. G. Haines, C. Kamperidis, R. J. Kingham, C. P. Ridgers, et al. Proton deflectometry of a magnetic reconnection geometry. *Physics of Plasmas*, 17:043104, 2010.

[66] M. Borghesi, L. Romagnani, A. Schiavi, D. H. Campbell, M. G. Haines, O. Willi, A. J. Mackinnon, M. Galimberti, L. Gizzi, R. J. Clarke, and S. Hawkes. Measurement of highly transient electrical charging following high-intensity laser-solid interaction. *Applied Physics Letters*, 82:1529–1531, 2003.

[67] K. Quinn, P. A. Wilson, C. A. Cecchetti, B. Ramakrishna, L. Romagnani, G. Sarri, L. Lancia, J. Fuchs, A. Pipahl, T. Toncian, O. Willi, R. J. Clarke, D. Neely, M. Notley, P. Gallegos, D. C. Carroll, M. N. Quinn, X. H. Yuan, P. McKenna, T. V. Liseykina, A. Macchi, and M. Borghesi. Laser-driven ultrafast field propagation on solid surfaces. *Physical Review Letters*, 102:194801, 2009.

[68] L. Willingale, A. G. R. Thomas, P. M. Nilson, M. C. Kaluza, S. Bandyopadhyay, A. E. Dangor, R. G. Evans, P. Fernandes, M. G. Haines, C. Kamperidis, et al. Fast advection of magnetic fields by hot electrons. *Physical Review Letters*, 105:095001, 2010.

[69] E. L. Clark, K. Krushelnick, M. Zepf, F. N. Beg, M. Tatarakis, A. Machacek, M. I. K. Santala, I. Watts, P. A. Norreys, and A. E. Dangor. Energetic heavy-ion and proton generation from ultraintense laser-plasma interactions with solids. *Physical Review Letters*, 85:1654–1657, 2000.

[70] A. Maksimchuk, S. Gu, K. Flippo, D. Umstadter, and V. Yu. Bychenkov. Forward ion acceleration in thin films driven by a high-intensity laser. *Physical Review Letters*, 84:4108–4111, 2000.

[71] R. A. Snavely, M. H. Key, S. P. Hatchett, T. E. Cowan, M. Roth, T. W. Phillips, M. A. Stoyer, E. A. Henry, T. C. Sangster, M. S. Singh, S. C. Wilks, A. MacKinnon, A. Offenberger, D. M. Pennington, K. Yasuike, A. B. Langdon, B. F. Lasinski, J. Johnson, M. D. Perry, and E. M. Campbell. Intense high-energy proton beams from petawatt-laser irradiation of solids. *Physical Review Letters*, 85:2945–2948, 2000.

[72] S. C. Wilks, A. B. Langdon, T. E. Cowan, M. Roth, M. Singh, S. Hatchett, M. H. Key, D. Pennington, A. MacKinnon, and R. A. Snavely. Energetic proton generation in ultra-intense laser-solid interactions. *Physics of Plasmas*, 8:542–549, 2001.

[73] S. P. D. Mangles, A. G. R. Thomas, M. C. Kaluza, O. Lundh, F. Lindau, A. Persson, F. S. Tsung, Z. Najmudin, W. B. Mori, C.-G. Wahlström, et al. Laser-wakefield acceleration of monoenergetic electron beams in the first plasma-wave period. *Physical Review Letters*, 96:215001, 2006.

[74] J. P. Freidberg, R. W. Mitchell, R. L. Morse, and L. I. Rudsinski. Resonant absorption of laser light by plasma targets. *Physical Review Letters*, 28:795–799, 1972.

[75] F. Brunel. Not-so-resonant, resonant absorption. *Physical Review Letters*, 59:52–55, 1987.

[76] A. R. Bell, J. R. Davies, S. Guerin, and H. Ruhl. Fast-electron transport in high-intensity short-pulse laser - solid experiments. *Plasma Physics and Controlled Fusion*, 39:653, 1997.

[77] C. McGuffey, A. G. R. Thomas, W. Schumaker, T. Matsuoka, V. Chvykov, F. J. Dollar, G. Kalintchenko, V. Yanovsky, A. Maksimchuk, K. Krushelnick, et al. Ionization induced trapping in a laser wakefield accelerator. *Physical Review Letters*, 104:025004, 2010.

[78] A. Pak, K. A. Marsh, S. F. Martins, W. Lu, W. B. Mori, and C. Joshi. Injection and trapping of tunnel-ionized electrons into laser-produced wakes. *Physical Review Letters*, 104:025003, 2010.

[79] K. Nakamura and Particle Data Group. Review of particle physics. *Journal of Physics G: Nuclear and Particle Physics*, 37:075021, 2010.

[80] M. Zepf, M. Castro-Colin, D. Chambers, S. G. Preston, J. S. Wark, J. Zhang, C. N. Danson, D. Neely, P. A. Norreys, A. E. Dangor, A. Dyson, P. Lee, A. P. Fews, P. Gibbon, S. Moustaizis, and M. H. Key. Measurements of the hole boring velocity from doppler shifted harmonic emission from solid targets. *Physics of Plasmas*, 3:3242–3244, 1996.

[81] P. V. Konash and I. G. Lebo. Simulations of electron-beam scattering by spontaneous magnetic fields in a laser plasma. *Quantum Electronics*, 36:767, 2006.

[82] M. A. Yates, D. B. van Hulsteyn, H. Rutkowski, G. Kyrala, and J. U. Brackbill. Experimental evidence for self-generated magnetic fields and remote energy deposition in laser-irradiated targets. *Physical Review Letters*, 49:1702–1704, 1982.

[83] H. Bethe and W. Heitler. On the stopping of fast particles and on the creation of positive electrons. *Proceedings of the Royal Society of London, Series A*, 146:83–112, 1934.

[84] J. D. Jackson. *Classical Electrodynamics*. John Wiley and Sons Inc., New York, New York, USA, 1962.

[85] S.D. Clarke, S.A. Pozzi, N. Cunningham, S. Banerjee, and D. Umstadter. Monte-carlo characterization of a pulsed laser-wakefield driven monochromatic x-ray source. In *Nuclear Science Symposium Conference Record (NSS/MIC), 2009 IEEE*, pages 1998–2003, 2009.

[86] W. P. Leemans, D. Rodgers, P. E. Catravas, C. G. R. Geddes, G. Fubiani, E. Esarey, B. A. Shadwick, R. Donahue, and A. Smith. Gamma-neutron activation experiments using laser wakefield accelerators. *Physics of Plasmas*, 8:2510–2516, 2001.

[87] S. A. Reed, V. Chvykov, G. Kalintchenko, T. Matsuoka, P. Rousseau, V. Yanovsky, C. R. Vane, J. R. Beene, D. Stracener, D. R. Schultz, and A. Maksimchuk. Photonuclear fission with quasimonoenergetic electron beams from laser wakefields. *Applied Physics Letters*, 89, 2006.

[88] S. A. Reed, V. Chvykov, G. Kalintchenko, T. Matsuoka, V. Yanovsky, C. R. Vane, J. R. Beene, D. Stracener, D. R. Schultz, and A. Maksimchuk. Efficient initiation of photonuclear reactions using quasimonoenergetic electron beams from laser wakefield acceleration. *Journal of Applied Physics*, 102, 2007.

[89] G. C. Baldwin and G. S. Klaiber. Photo-fission in heavy elements. *Physical Review*, 71:3–10, 1947.

[90] C. Courtois, A. C. La Fontaine, O. Landoas, G. Lidove, V. Méot, P. Morel, R. Nuter, E. Lefebvre, A. Boscheron, J. Grenier, et al. Effect of plasma density scale length on the properties of bremsstrahlung x-ray sources created by picosecond laser pulses. *Physics of Plasmas*, 16:013105, 2009.

[91] K. W. D. Ledingham, I. Spencer, T. McCanny, R. P. Singhal, M. I. K. Santala, E. Clark, I. Watts, F. N. Beg, M. Zepf, K. Krushelnick, M. Tatarakis, A. E. Dangor, P. A. Norreys, R. Allott, D. Neely, R. J. Clark, A. C. Machacek, J. S. Wark, A. J. Cresswell, D. C. W. Sanderson, and J. Magill. Photonuclear physics when a multiterawatt laser pulse interacts with solid targets. *Physical Review Letters*, 84:899–902, 2000.

[92] C. Gahn, G. D. Tsakiris, G. Pretzler, K. J. Witte, C. Delfin, C.-G. Wahlstrm, and D. Habs. Generating positrons with femtosecond-laser pulses. *Applied Physics Letters*, 77:2662–2664, 2000.

[93] C. Gahn, G. D. Tsakiris, G. Pretzler, K. J. Witte, P. Thirolf, D. Habs, C. Delfin, and C.-G. Wahlstrm. Generation of mev electrons and positrons with femtosecond pulses from a table-top laser system. *Physics of Plasmas*, 9:987–999, 2002.

[94] Hui Chen, Scott C. Wilks, James D. Bonlie, Edison P. Liang, Jason Myatt, Dwight F. Price, David D. Meyerhofer, and Peter Beiersdorfer. Relativistic positron creation using ultraintense short pulse lasers. *Physical Review Letters*, 102:105001, 2009.

[95] Hui Chen, S. C. Wilks, D. D. Meyerhofer, J. Bonlie, C. D. Chen, S. N. Chen, C. Courtois, L. Elberson, G. Gregori, W. Kruer, O. Landoas, J. Mithen, J. Myatt, C. D. Murphy, P. Nilson, D. Price, M. Schneider, R. Shepherd, C. Stoeckl, M. Tabak, R. Tommasini, and P. Beiersdorfer. Relativistic quasimonoenergetic positron jets from intense laser-solid interactions. *Physical Review Letters*, 105:015003, 2010.

[96] D. Taylor, E. Liang, T. Clarke, A. Henderson, P. Chaguine, X. Wang, G. Dyer, K. Serratto, N. Riley, M. Donovan, and T. Ditmire. Hot electron and pair production from the texas petawatt laser irradiating thick gold targets. *arXiv preprint arXiv:1205.1874*, 2012.

[97] International Atomic Energy Agency. Experimental nuclear reaction data (exfor). https://www-nds.iaea.org/exfor/exfor.htm.

[98] C. M. Ankenbrandt and Muon Collider Collaboration. Status of muon collider research and development and future plans. *Physical Review Special Topics: Accelerators and Beams*, 2:081001, 1999.

[99] D. J. Gibson, F. Albert, S. G. Anderson, S. M. Betts, M. J. Messerly, H. H. Phan, V. A. Semenov, M. Y. Shverdin, A. M. Tremaine, F. V. Hartemann, C. W. Siders, D. P. McNabb, and C. P. J. Barty. Design and operation of a tunable mev-level compton-scattering-based gamma-ray source. *Physical Review Special Topics: Accelerators and Beams*, 13:070703, 2010.

[100] F. Albert, S. G. Anderson, D. J. Gibson, R. A. Marsh, S. S. Wu, C. W. Siders, C. P. J. Barty, and F. V. Hartemann. Design of narrow-band compton scattering sources for nuclear resonance fluorescence. *Physical Review Special Topics: Accelerators and Beams*, 14:050703, 2011.

[101] F. V. Hartemann, F. Albert, C. W. Siders, and C. P. J. Barty. Low-intensity nonlinear spectral effects in compton scattering. *Physical Review Letters*, 105:130801, 2010.

[102] C. Bamber, S. J. Boege, T. Koffas, T. Kotseroglou, A. C. Melissinos, D. D. Meyerhofer, D. A. Reis, W. Ragg, C. Bula, K. T. McDonald, E. J. Prebys, D. L. Burke, R. C. Field, G. Horton-Smith, J. E. Spencer, D. Walz, S. C. Berridge, W. M. Bugg, K. Shmakov, and A. W. Weidemann. Studies of nonlinear qed in collisions of 46.6 gev electrons with intense laser pulses. *Physical Review D*, 60:092004, 1999.

[103] D. L. Burke, R. C. Field, G. Horton-Smith, J. E. Spencer, D. Walz, S. C. Berridge, W. M. Bugg, K. Shmakov, A. W. Weidemann, C. Bula, K. T. McDonald, E. J. Prebys, C. Bamber, S. J. Boege, T. Koffas, T. Kotseroglou, A. C. Melissinos, D. D. Meyerhofer, D. A. Reis, and W. Ragg. Positron production in multiphoton light-by-light scattering. *Physical Review Letters*, 79:1626–1629, 1997.

[104] C. Bula, K. T. McDonald, E. J. Prebys, C. Bamber, S. Boege, T. Kotseroglou, A. C. Melissinos, D. D. Meyerhofer, W. Ragg, D. L. Burke, R. C. Field, G. Horton-Smith, A. C. Odian, J. E. Spencer, D. Walz, S. C. Berridge, W. M. Bugg, K. Shmakov, and A. W. Weidemann. Observation of nonlinear effects in compton scattering. *Physical Review Letters*, 76:3116–3119, 1996.

[105] Y. Y. Lau, F. He, D. P Umstadter, and R. Kowalczyk. Nonlinear thomson scattering: A tutorial. *Physics of Plasmas*, 10:2155, 2003.

[106] F. He, Y. Y. Lau, D. P. Umstadter, and R. Kowalczyk. Backscattering of an intense laser beam by an electron. *Physical Review Letters*, 90:055002, 2003.

[107] S. P. D. Mangles. Compact x-ray sources: X-rays from self-reflection. *Nature Photonics*, 6:280–281, 2012.

[108] K. Ta Phuoc, S. Corde, C. Thaury, V. Malka, A. Tafzi, J. P. Goddet, R. C. Shah, S. Sebban, and A. Rousse. All-optical compton gamma-ray source. *Nature Photonics*, 6:308–311, 2012.

[109] S. Chen, N. D. Powers, I. Ghebregziabher, C. M. Maharjan, C. Liu, G. Golovin, S. Banerjee, J. Zhang, N. Cunningham, A. Moorti, S. Clarke, S. Pozzi, and D. P. Umstadter. Mev-energy x rays from inverse compton scattering with laser-wakefield accelerated electrons. *Physical Review Letters*, 110:155003, 2013.

[110] N. D. Powers, I. Ghebregziabher, G. Golovin, C. Liu, S. Chen, S. Banerjee, J. Zhang, and D. P Umstadter. Quasi-monoenergetic and tunable x-rays from a laser-driven compton light source. *Nature Photonics*, 8:28–31, 2014.

[111] A. Di Piazza, C. Müller, K. Z. Hatsagortsyan, and C. H. Keitel. Extremely high-intensity laser interactions with fundamental quantum systems. *Review of Modern Physics*, 84:1177–1228, 2012.

[112] A. G. R. Thomas, C. P. Ridgers, S. S. Bulanov, B. J. Griffin, and S. P. D. Mangles. Strong radiation-damping effects in a gamma-ray source generated by the interaction of a high-intensity laser with a wakefield-accelerated electron beam. *Physical Review X*, 2:041004, 2012.

[113] T. G. Blackburn, C. P. Ridgers, J. G. Kirk, and A. R. Bell. Quantum radiation reaction in laserelectron-beam collisions. *Physical Review Letters*, 112:015001, 2014.

[114] W. Schumaker, N. Nakanii, C. McGuffey, C. Zulick, V. Chyvkov, F. Dollar, H. Habara, G. Kalintchenko, A. Maksimchuk, K.A. Tanaka, et al. Ultrafast electron radiography of magnetic fields in high-intensity laser-solid interactions. *Physical Review Letters*, 110:015003, 2013.

[115] W. Schumaker, G. Sarri, M. Vargas, Z. Zhao, K. Behm, V. Chvykov, B. Dromey, B. Hou, A. Maksimchuk, J. Nees, V. Yanovsky, A. G. R. Zepf, M. ands Thomas, and K. Krushelnick. Short-pulse, high-energy radiation generation from laser wakefield accelerated electron beams. (accepted, to be published).

[116] G. Sarri, W. Schumaker, A. Di Piazza, M. Vargas, B. Dromey, M. E. Dieckmann, V. Chvykov, A. Maksimchuk, V. Yanovsky, Z. H. He, et al. Table-top laser-based source of femtosecond, collimated, ultrarelativistic positron beams. *Physical Review Letters*, 110:255002, 2013.

[117] G. Sarri, W. Schumaker, A. Di Piazza, K. Poder, J. M. Cole, M. Vargas, D. Doria, S. Kushel, B. Dromey, G. Grittani, et al. Laser-driven generation of collimated ultra-relativistic positron beams. *Plasma Physics and Controlled Fusion*, 55:124017, 2013.

[118] G. Sarri, K. Poder, J. M. Cole, W. Schumaker, A. Di Piazza, B. Reville, D. Doria, B. Dromey, L. Gizzi, A. Green, et al. Generation of a neutral, high-density electron-positron plasma in the laboratory. *arXiv preprint arXiv:1312.0211*, 2013.

[119] J. Faure, C. Rechatin, A. Norlin, A. Lifschitz, Y. Glinec, and V. Malka. Controlled injection and acceleration of electrons in plasma wakefields by colliding laser pulses. *Nature*, 444:737–739, 2006.